https://ntrs.nasa.gov/search.jsp?R=20190002344 2020-03-10T16:41:24+00:00Z

The Astrophysical Journal, 864:150 (30pp), 2018 September 10 https://doi.org/10.3847/1538-4357/aad500
© 2018. The American Astronomical Society. All rights reserved.

Black Holes and Neutron Stars in Nearby Galaxies: Insights from *NuSTAR*

N. Vulic[1,2], A. E. Hornschemeier[1,3], D. R. Wik[1,4], M. Yukita[1,3], A. Zezas[5,6], A. F. Ptak[1,3], B. D. Lehmer[7], V. Antoniou[6], T. J. Maccarone[8], B. F. Williams[9], and F. M. Fornasini[6]

[1] Laboratory for X-ray Astrophysics, Code 662, NASA Goddard Space Flight Center, Greenbelt, MD 20771, USA; nvulic@uwo.ca
[2] Department of Astronomy and Center for Space Science and Technology (CRESST), University of Maryland, College Park, MD 20742-2421, USA
[3] Department of Physics & Astronomy, Johns Hopkins University, 3400 North Charles Street, Baltimore, MD 21218, USA
[4] Department of Physics & Astronomy, University of Utah, Salt Lake City, UT 84112-0830, USA
[5] Physics Department & Institute of Theoretical & Computational Physics, University of Crete, 71003 Heraklion, Crete, Greece
[6] Harvard-Smithsonian Center for Astrophysics, 60 Garden Street, Cambridge, MA 02138, USA
[7] Department of Physics, University of Arkansas, 825 West Dickson Street, Fayetteville, AR 72701, USA
[8] Department of Physics & Astronomy, Box 41051, Science Building, Texas Tech University, Lubbock, TX 79409-1051, USA
[9] Department of Astronomy, Box 351580, University of Washington, Seattle, WA 98195, USA
Received 2018 February 21; revised 2018 July 18; accepted 2018 July 18; published 2018 September 11

Abstract

Nearby galaxy surveys have long classified X-ray binaries (XRBs) by the mass category of their donor stars (high-mass and low-mass). The *NuSTAR* observatory, which provides imaging data at $E > 10$ keV, has enabled the classification of extragalactic XRBs by their compact object type: neutron star (NS) or black hole (BH). We analyzed *NuSTAR*/*Chandra*/*XMM-Newton* observations from a *NuSTAR*-selected sample of 12 galaxies within 5 Mpc having stellar masses ($M_\star$) $10^{7-11} M_\odot$ and star formation rates (SFRs) ≈ 0.01–$15\, M_\odot\, \mathrm{yr}^{-1}$. We detected 128 *NuSTAR* sources to a sensitivity of $\approx 10^{38}$ erg s^{-1}. Using *NuSTAR* color-intensity and color–color diagrams we classified 43 of these sources as candidate NSs and 47 as candidate BHs. We further subdivide BHs by accretion states (soft, intermediate, and hard) and NSs by weak (Z/Atoll) and strong (accreting pulsar) magnetic field. Using eight normal (Milky Way-type) galaxies in the sample, we confirm the relation between the SFR and galaxy X-ray point source luminosity in the 4–25 and 12–25 keV energy bands. We also constrained galaxy X-ray point source luminosity using the relation $L_X = \alpha M_\star + \beta \mathrm{SFR}$, finding agreement with previous work. The X-ray luminosity function (XLF) of all sources in the 4–25 and 12–25 keV energy bands matches the $\alpha = 1.6$ slope for high-mass XRBs. We find that NS XLFs suggest a decline beginning at the Eddington limit for a $1.4\, M_\odot$ NS, whereas the BH fraction shows an approximate monotonic increase in the 4–25 and 12–25 keV energy bands. We calculate the overall ratio of BH to NS to be ≈ 1 for 4–25 keV and ≈ 2 for 12–25 keV.

Key words: galaxies: luminosity function, mass function – pulsars: general – stars: black holes – stars: neutron – X-rays: binaries – X-rays: galaxies

1. Introduction

Until the launch of the first focusing telescope to operate at $E > 10$ keV, the *Nuclear Spectroscopic Telescope Array* (*NuSTAR*; Harrison et al. 2013), we knew very little about the behavior and nature of extragalactic black hole (BH) and neutron star (NS) populations at harder energies. In the absence of an X-ray bright supermassive BH, the total X-ray emission of a galaxy above 2 keV is dominated by X-ray binaries (XRBs), classified as low-mass (LMXB) or high-mass (HMXB) based on their donor star. Previous studies of nearby galaxies in the soft X-ray band (0.5–10 keV) by, e.g., *Chandra* and *XMM-Newton* (e.g., Stiele et al. 2011; Mineo et al. 2012, 2014; Long et al. 2014; Haberl & Sturm 2016; Peacock & Zepf 2016), have revealed important new information on compact object populations, such as strong correlations between the properties of XRBs and the galaxy star formation rate (SFR), stellar mass, and metallicity (e.g., Basu-Zych et al. 2016). Extrapolation of these local-universe measurements as well as supporting measurements at high redshift (Lehmer et al. 2016) have indicated a possible significant role of XRBs in heating the intergalactic medium of the early universe (e.g., Fragos et al. 2013; Mesinger et al. 2014; Pacucci et al. 2014; Das et al. 2017; Madau & Fragos 2017; Sazonov & Khabibullin 2017).

However, there are questions about the extragalactic XRB population that are difficult to answer at $E < 10$ keV, including whether compact objects are BHs or NSs. The rich suite of thousands of *Rossi X-ray Timing Explorer* (*RXTE*) Proportional Counter Array (PCA) spectra of BH/NS XRBs in the Milky Way galaxy provide critical diagnostics in the 4–25 keV band of both compact object type (BH versus NS) and accretion state (e.g., Maccarone & Coppi 2003; McClintock & Remillard 2006; Done et al. 2007). With *NuSTAR*, for the first time, we are able to leverage the knowledge gained from compact objects in our own galaxy by applying these harder X-ray diagnostics to extragalactic populations.

The hard X-ray coverage with *NuSTAR* is crucial for distinguishing different types of accreting binaries, such as BH/NS XRBs and accreting pulsars. Compact object diagnostics have already been successfully applied to characterize XRBs in several nearby galaxies observed by *NuSTAR*. These studies include simultaneous *NuSTAR*/*Chandra*/*XMM-Newton*/*Swift* studies of the nearby star-forming galaxies NGC 253 (Lehmer et al. 2013; Wik et al. 2014b) and M83 (Yukita et al. 2016), as well as Local Group galaxy M31 (Maccarone et al. 2016; Yukita et al. 2017; Lazzarini et al. 2018); for a description of the *NuSTAR* galaxy program please see Hornschemeier et al. (2016). Using 4–25 keV color–color and color-intensity diagnostics, these studies have shown that the starburst galaxies are dominated by luminous BH-XRB systems, mostly in intermediate accretion states. Specifically, ultraluminous X-ray sources (ULXs) with 3–30 keV spectra

Table 1
Galaxy Properties

Galaxy	R.A. (J2000.0)	Decl. (J2000.0)	Type	D_{25}	d_{25}	Inclination	Linear Scale	Distance	Uncertainty	N_H	Stellar Mass	SFR
				(′)	(′)	(degrees)	(pc/″)	(Mpc)	(Mpc)	(10^{20} cm^{-2})	(10^9 $M_\odot$)	($M_\odot$ yr^{-1})
(1)	(2)	(3)	(4)	(5)	(6)	(7)	(8)	(9)	(10)	(11)	(12)	(13)
M31[a]	10.685	41.269	Sb	177.8	69.2	72	3.73	0.77	0.04	6.7	93.88	0.32
Holmberg II	124.768	70.722	I	7.9	5.6	51	15.85	3.27	0.18	3.4	0.11	0.06
IC 342	56.705	68.101	SABc	20.0	19.1	18	16.44	3.39	0.22	28.7	22.64	3.90
M82	148.968	69.680	Scd	11.0	5.1	76	17.11	3.53	0.26	4.0	32.45	12.52
NGC 253	11.888	−25.288	SABc	26.9	4.6	90	17.26	3.56	0.26	1.4	71.63	5.82
M81	148.888	69.065	Sab	21.4	11.2	62	17.50	3.61	0.20	4.2	88.22	0.47
NGC 4945	196.364	−49.468	SBc	23.4	4.1	90	18.04	3.72	0.27	14.9	38.15	4.35
Holmberg IX	149.383	69.046	I	2.5	2.1	34	18.28	3.77	0.28	4.3	0.02	0.01
Circinus	213.291	−65.339	Sb	8.7	4.3	64	20.36	4.20	0.78	59.9	53.70	3.23
NGC 1313	49.565	−66.498	SBcd	11.0	9.1	34	20.60	4.25	0.31	4.0	1.17	0.58
M83	204.254	−29.866	Sc	13.5	13.2	14	22.59	4.66	0.30	3.7	44.06	3.41
NGC 5204	202.402	58.419	Sm	4.5	2.8	58	23.66	4.88	0.38	1.4	0.21	0.08

Note. Galaxy properties. Unless indicated, values have been taken from the HyperLeda database (Makarov et al. 2014, http://leda.univ-lyon1.fr/). Columns 5 and 6: major and minor isophotal diameters D_{25} and d_{25}, respectively, for $\mu_B = 25$ mag arcsec^{-2}. Column 7: inclination in degrees. Column 8: linear scale in pc representing 1″ at the adopted distance. Distances are from Tully et al. (2013) except for Circinus, which is from Tully et al. (2009). Column 10: 1σ distance uncertainty. Column 11: Galactic column density from Kalberla et al. (2005). Columns 12 and 13: stellar mass and SFR as determined using the methods from Section 2.1.
[a] Results for M31 can be found in D. Wik et al. (2018, in preparation).

indicative of super-Eddington accretion (e.g., Gladstone et al. 2009) appear to dominate the hard X-ray emission of starburst galaxies (Walton et al. 2013; Bachetti et al. 2014b; Lehmer et al. 2015; Rana et al. 2015). Meanwhile, M31 has a significant contribution from NS accretors (pulsars and low-magnetic field Z-type sources; Maccarone et al. 2016; Yukita et al. 2017). As expected, the pulsars trace the young stellar population in the spiral arms and the Z-type sources are concentrated in globular clusters and the bulge/field of the galaxy. *NuSTAR* data were crucial to the reclassification of previously identified BH candidates in M31 globular clusters as NSs, based on their hard X-ray spectra (Maccarone et al. 2016).

NuSTAR has previously resolved the XRB population in three galaxies. Thus, it is now time for a broader investigation of the relationship between the properties of a galaxy and the X-ray source types and accretion states as determined from hard X-ray observations. Specifically, what is the relationship between galaxy properties, such as the stellar mass and recent SFR/history and compact object type/accretion state, as determined from hard X-ray diagnostics? To estimate the number of BHs and NSs that will be formed in a galaxy requires binary population synthesis, and a detailed understanding of concepts, such as supernova explosions, which are not well understood (e.g., Pejcha & Thompson 2015). Alternatively, we can use observational data and methods to determine the BH fraction and its dependence on X-ray luminosity and the specific star formation rate (sSFR).

With *NuSTAR* we can measure local-galaxy spectral energy distributions (SEDs) over 0.5–30 keV that are applicable to high-z galaxies detected by *Chandra*. One of our goals is to determine what sources are contributing to the 0.5–30 keV emission. Furthermore, we would like to be able to predict, based on galaxy properties such as SFR/history and stellar mass, what the distribution of binaries and their emitting properties are. Achieving this goal is rather complicated, as there are parameters, such as the duty cycle, that result in a broad range of population properties for different stellar ages, etc. One approach to this complicated problem is to make direct measurements over a variety of galaxy properties. Each snapshot view of an individual galaxy measures the state of the overall population, giving us a constraint on duty cycles (Binder et al. 2017). Hard X-ray diagnostics allow us to determine the distribution of BH spectral states, similar to Galactic BH studies (e.g., Tetarenko et al. 2016). Using this approach, we can obtain baseline estimates of the XRB formation rate, duty cycles, spectral states, and galaxy SEDs. Understanding these properties at $E > 10$ keV is critical to compare to the results of XRB evolution in the 0.5–10 keV bandpass. *NuSTAR* is well matched to the rest-frame energies of high-z galaxies at $z = 3$–4 probed by *Chandra* and is thus a new window into XRB evolution.

The X-ray luminosity function (XLF) represents the distribution of sources in a galaxy based on their luminosity. Seminal studies of LMXBs in elliptical galaxies (e.g., Gilfanov 2004a; Zhang et al. 2012) and HMXBs in spiral galaxies (e.g., Grimm et al. 2003; Mineo et al. 2012) found that their XLFs were (approximately) universal when normalizing by the stellar mass and the SFR of a galaxy, respectively (see Gilfanov 2004b for a summary). Small variations in the power-law slope and cutoff are dependent on factors such as metallicity (Basu-Zych et al. 2016) and star formation history (Lehmer et al. 2017). We will investigate how scaling *NuSTAR* XLFs by the SFR compares with results from *Chandra*/*XMM-Newton* studies.

To date, studies of the XLFs of nearby galaxies have mostly focused on LMXB or HMXB populations. However, certain XLF characteristics can be attributed to compact object types (Lutovinov et al. 2013), such as the break at $\sim$few$\times 10^{38}$ erg s^{-1} corresponding to the Eddington limit for NS. This break is often argued to reflect the transition from a population of NS to BH XRBs (Sarazin et al. 2000; Kim & Fabbiano 2004; Wang et al. 2016). *NuSTAR* is well suited to distinguish between BH and NS accretors, therefore allowing a first look at BH-only and NS-only XLFs. In addition, this can elucidate how the 0.5–30 keV SED of galaxies depends

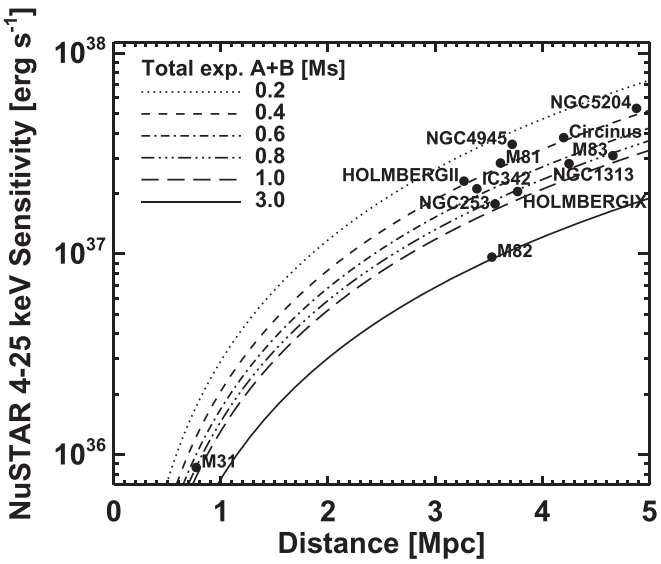

Figure 1. Shown is the X-ray point source sensitivity of each *NuSTAR*-observed galaxy, which is affected most directly by the exposure time and the distance to the galaxy. *NuSTAR* point source (absorbed) sensitivity limits were calculated for each galaxy based on a 3σ detection (30″ extraction region for telescopes A and B) using the distance and $N_{\rm H}$ values from Table 1 and a spectral index of $\Gamma = 1.7$. Exposure times were taken from Table 2 (telescopes A and B) and we assumed a constant background based on the value from the 30″ *NuSTAR* background spectrum file. Lines of constant exposure time for telescopes A and B in Ms are shown based on the same assumptions with a constant $N_{\rm H}$ value of 10^{20} cm^{-2}.

on the compact object type and accretion states of BHs and NSs.

Our goals are to study the hard X-ray properties of the XRB population of 12 nearby galaxies (<5 Mpc), using joint *NuSTAR* and *Chandra*/*XMM-Newton* data. We will use knowledge of galaxy parameters, such as the SFR and stellar mass, to investigate the connection between XRB populations and host galaxy properties. In Section 2, we describe the sample selection and the calculation of the SFR and stellar mass for galaxies in the sample. In Section 3, we summarize the *NuSTAR*, *Chandra*, and *XMM-Newton* observations. In Section 4, we outline our analysis methods, which focus on the point-spread function (PSF) fitting procedure for *NuSTAR* data. In Section 5, we present *NuSTAR* diagnostic diagrams, XLFs, and scaling relations, and discuss their implications. We summarize our conclusions in Section 6.

2. Sample Selection

Using the HyperLeda database[10] (Makarov et al. 2014) and the Updated Nearby Galaxy catalog (Karachentsev et al. 2013) we searched for all galaxies within 10 Mpc that have been observed by *NuSTAR* as of 1 July 2017. We created the sample based on reaching an X-ray point source sensitivity limit of $\approx 10^{38}$ erg s^{-1} (4–25 keV), corresponding to the expected approximate luminosity of luminous non-magnetized NS XRBs,[11] for each observed galaxy. We excluded M51, NGC 4258, and NGC 4395 because they did not reach this limit. We also excluded Centaurus A due to the presence of a luminous active galactic nucleus (AGN), whose emission contaminated the field of view (FOV) and prevented the detection of faint point sources. The nearby dwarf galaxy IC 10 was excluded due to contamination from stray light.

In Table 1 we list the 12 galaxies in the sample and include their coordinates, morphological type, dimensions, inclination, distance, Galactic column density, stellar masses, and SFR (see Section 2.1). Several of these galaxies are either part of the *NuSTAR* nearby galaxies program (Hornschemeier et al. 2016) or were targeted because they contained individual ULX sources that are likely high-accretion rate XRBs (Bachetti et al. 2014a; Kaaret et al. 2017).

There is sufficient *NuSTAR* exposure for the entire galaxy sample for detection of all point sources with $L_{\rm X}$ above $\sim 10^{38}$ erg s^{-1} (4–25 keV). However, there is spatial variation of sensitivity within the galaxies due to source confusion in regions with higher relative source density. In Figure 1 we plot the 4–25 keV point source sensitivity limit against the distance of each galaxy and show sensitivity curves for total exposure times ranging from 200 ks to 3 Ms.

To date, while there have been studies of individual sources or galaxies, there has not been a systematic analysis of the hard X-ray point source populations for an ensemble of these galaxies. The X-ray point source populations of these galaxies have been well studied in the 0.5–10 keV bandpass in the past by various X-ray observatories, such as *Chandra*, *XMM-Newton*, and *ROSAT*, with the exception of NGC 1313 and NGC 5204, where the focus has been on ULX sources as opposed to the point source population. In the Appendix, we summarize individual galaxy properties and previous X-ray studies for each galaxy in the sample. A detailed study of M31 will be presented by D. Wik et al. (2018, in preparation), thus we exclude M31 from our analysis (except for total galaxy X-ray luminosity fitting in Section 5.2).

2.1. Stellar Masses and SFRs

The LMXB and HMXB populations in a galaxy trace the host galaxy stellar mass and SFR, respectively. Therefore, to investigate this relationship, we need to determine accurate values of the galaxy stellar mass and SFR. To calculate stellar masses we used the results from Into & Portinari (2013) that were corrected for self-consistency by McGaugh & Schombert (2014). This relation was derived assuming a Kroupa (1998) initial mass function (IMF). We chose the parameterization reproduced in Equation (1) because $(B - V)$ colors were readily available from the HyperLeda database (Makarov et al. 2014) and the $K_{\rm s}$-band luminosity is a robust indicator of stellar mass. Extinction-corrected 2MASS $K_{\rm s}$-band magnitudes were taken from Tully et al. (2016) and converted to luminosities using the distances from Table 1 and $K_{{\rm s},\odot} = 3.302$ (Casagrande et al. 2012; Pecaut & Mamajek 2013). The revised relation from McGaugh & Schombert (2014) was based on *Spitzer* 3.6 μm data and required conversion of K-band magnitudes using their prescription $K_{\rm s} - [3.6] = 0.31$. The resulting stellar masses were each multiplied by 1.29 to convert from 3.6 μm to K-band. Typical M/L uncertainties were estimated to be $\sim$0.1 dex in the near-IR as a result of dust and complex star formation histories.

$$\log(M_\star/M_\odot) = \log(L_{K_{\rm s},{\rm gal}}/L_{K_{\rm s},\odot}) + 0.849(B - V) - 0.861. \quad (1)$$

The $K_{\rm s}$-band magnitude and $(B-V)$ color for M31 were adjusted using the values from Table 3 of Kormendy & Ho (2013), corrected for angular extent. The stellar mass agrees

[10] http://leda.univ-lyon1.fr/

[11] e.g., Sco X-1; $L_{\rm X}$ (2 − 20 keV) $\approx 2 \times 10^{38}$ erg s^{-1}, Bradshaw et al. (1999).

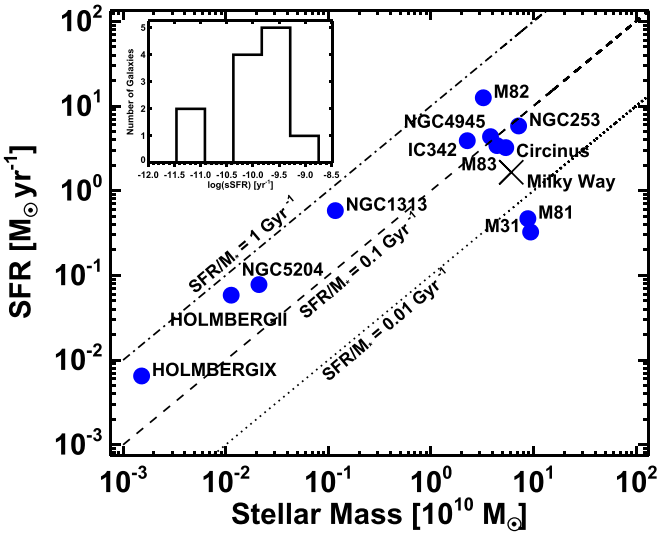

Figure 2. Shown are the SFRs and stellar masses $M_\star$ for all 12 galaxies in the sample (see Table 1 and Section 2.1 for the SFR and stellar mass calculations). Lines of constant sSFR (SFR/$M_\star$) are indicated to gauge the contribution from HMXBs. The Milky Way has been included as a comparison to the sample. The inset shows a histogram of the sSFR for all galaxies in the sample. The calculation of the stellar mass and SFR assumed a Kroupa (1998) and Kroupa (2001) IMF, respectively.

with the recently determined value from Sick et al. (2015). NGC 4945 suffers from large internal extinction that affects the stellar mass estimate, so we used the $(B - V)$ value from McCall (2014) that was corrected for internal extinction.

We determined the SFRs from the relations presented in Calzetti (2013) by adding the contribution from the UV and IR luminosity (Calzetti 2013 Equation (1.11)). These relations all assumed a Kroupa (2001) IMF. Equation (2) (Calzetti 2013 Equation (1.2)) was used to estimate the UV (dust-obscured) component of the SFR:

$$\mathrm{SFR(UV)}\ [M_\odot/\mathrm{yr}^{-1}] = 3 \times 10^{-47}\lambda[\text{Å}]L(\lambda)[\mathrm{erg\ s}^{-1}]. \quad (2)$$

We used *GALEX* far-UV (1539 Å, FWHM of 269 Å) asymptotic (total) magnitudes from Lee et al. (2011) and Gil de Paz et al. (2007, only for M31) to calculate the SFR (UV). We calculated the IR (dust-unobscured) component of the SFR with Equation (3) (Calzetti 2013 Equations (1.5–1.7)) using 24 μm fluxes from Dale et al. (2009).

$$\mathrm{SFR(IR)}\ [M_\odot/\mathrm{yr}^{-1}] = 2.04 \times 10^{-43}L(\lambda)[\mathrm{erg\ s}^{-1}]. \quad (3)$$

M31 and IC 342 did not have 24 μm fluxes in Dale et al. (2009) and were instead taken from Tempel et al. (2010) and Jarrett et al. (2013), respectively. For Circinus, we used the 25 μm *IRAS* flux from the NASA/IPAC Extragalactic Database (NED) and adjusted the coefficient in Equation (3) to 1.789×10^{-43}. NGC 4945 did not have a UV flux estimate and so we used the SFR from Atacama Large Millimeter Array results (Bendo et al. 2016), which were not affected by dust attenuation in the nuclear starburst. Circinus also had no UV flux estimate and thus we only used the SFR (25 μm) value as it agrees well with other studies (Grimm et al. 2003; For et al. 2012).

In Figure 2 we plot the SFR versus the stellar mass for each galaxy in the sample. We also included the Milky Way for reference. The stellar mass and SFR for the Milky Way, $6.08 \pm 1.14 \times 10^{10}\,M_\odot$ and $1.65 \pm 0.19\ M_\odot\,\mathrm{yr}^{-1}$, respectively, were taken from Licquia & Newman (2015). Lines of a constant specific SFR (sSFR) are indicated to help compare the relative amount of star formation per galaxy across a variety of stellar masses. One expects fractionally more HMXBs in galaxies with higher values of sSFR. Most of the galaxies in the sample (8 of 12) have stellar masses comparable to the Milky Way galaxy. There is a range of sSFR values with a peak around the value for the Milky Way. The *NuSTAR* archive represents a biased nearby galaxy sample that tends toward an intermediate sSFR as seen in Figure 2. This results from the relative lack of nearby massive elliptical galaxies that have a low sSFR (e.g., Cen A, Maffei 1) and few nearby starbursts with a large sSFR (e.g., NGC 253, M82).

3. Observations

Table 2 summarizes the simultaneous/archival *NuSTAR* and *Chandra*/*XMM-Newton* observations for galaxies in the sample that were analyzed in this work (Table 1). We have excluded all *NuSTAR* observations of galaxies that are shorter than ~10 ks (before data reduction) because it is not possible to robustly constrain the background. Each observatory's FOV covers the D_{25} ellipse of all galaxies except the *NuSTAR* observations of M83 (~90% of D_{25}, see Yukita et al. 2016), IC 342 (~75% of D_{25}), and M31 (~40% of D_{25}). There was non-contemporaneous archival X-ray data available for these galaxies, however, simultaneous data are particularly important for the study of the highly variable XRB population. Thus, we prioritized simultaneous *Chandra*/*XMM-Newton* data for our analyses. Such data were available for 11 of the 12 galaxies; for M81 we relied solely upon archival data. Due to the high frequency of observations for M31, M82, and Holmberg IX, only some observations were simultaneous with *Chandra*/*XMM-Newton*. If simultaneous observations were not present, we used observations as close in time as possible. We used *Chandra* ACIS observations and *XMM-Newton* PN for 11 of the 12 galaxies because of the higher signal-to-noise ratio compared to *XMM-Newton* MOS. The *XMM-Newton* PN observation of M81 was taken in small window mode and so we used the MOS detector data in order to cover the entire FOV. This combination of *Chandra*/*XMM-Newton* observations ensures that we have high spatial resolution X-ray data to create point source lists used in *NuSTAR* data processing (see Section 4.3).

4. Data Analysis

4.1. NuSTAR

NuSTAR data were reduced using HEASOFT v6.19/NUSTARDAS v1.6.0 along with CALDB version 20161021. We reprocessed all level 1 event files using NUPIPELINE to obtain cleaned level 2 event files. This script measured the alignment of the mast connecting the focal plane detectors and optics, applied gain and dead time correction, flagged bad/hot pixels, filtered good time intervals and screened events based on grade and status, and converted raw detector positions into sky coordinates. The script also filtered out observational data during passages through the South Atlantic Anomaly that caused periods of high background, accomplished by setting the parameters `SAAMODE` to *strict* and `TENTACLE` to *yes*. While reducing exposure times by ~10%, these parameters decreased the uncertainty associated with our background

Table 2
NuSTAR, *Chandra*, and *XMM-Newton* Observations of the *NuSTAR* Galaxy Sample

Galaxy	*NuSTAR* ObsID	Date	R.A. (J2000.0)	Decl. (J2000.0)	Livetime ks	Observatory	ObsID	Date	R.A. (J2000.0)	Decl. (J2000.0)	Livetime ks
Circinus	60002039002	2013 Jan 25	213.3888	−65.3207	53.7	*XMM-Newton*	0701981001	2013 Feb 03	213.1538	−65.3638	21.1
	30002038002	2013 Feb 02	213.2684	−65.3867	18.3	*XMM-Newton*	0792382701	2016 Aug 23	213.1643	−65.4209	12.3
	30002038004	2013 Feb 03	213.2347	−65.3826	40.3	…	…	…	…	…	…
	30002038006	2013 Feb 05	213.2318	−65.3847	35.9	…	…	…	…	…	…
	90201034002	2016 Aug 23	213.1020	−65.3954	39.0	…	…	…	…	…	…
Holmberg II	30001031002	2013 Sep 09	124.8517	70.6840	25.1	*XMM-Newton*	0200470101	2004 Apr 15	124.9008	70.6784	28.5
	30001031003	2013 Sep 09	124.9776	70.6930	67.0	*XMM-Newton*	0724810101	2013 Sep 09	124.8877	70.7336	4.0
	30001031005	2013 Sep 17	124.9655	70.7048	93.1	*XMM-Newton*	0724810301	2013 Sep 17	124.8792	70.7334	5.5
Holmberg IX	30002033002	2012 Oct 26	149.4906	69.0590	27.1	*XMM-Newton*	0693850801	2012 Oct 23	149.4712	69.0920	5.7
	30002033003	2012 Oct 26	149.5251	69.0561	76.4	*XMM-Newton*	0693850901	2012 Oct 25	149.4716	69.0921	4.9
	30002033005	2012 Nov 11	149.5509	69.0710	33.2	*XMM-Newton*	0693851001	2012 Oct 27	149.4682	69.0923	3.9
	30002033006	2012 Nov 11	149.4688	69.0646	30.0	*XMM-Newton*	0693851701	2012 Nov 12	149.4493	69.0916	6.2
	30002033008	2012 Nov 14	149.5119	69.0671	10.7	*XMM-Newton*	0693851801	2012 Nov 14	149.4477	69.0912	6.6
	30002033010	2012 Nov 15	149.5060	69.0666	38.5	*XMM-Newton*	0693851101	2012 Nov 16	149.4466	69.0908	2.6
	30002034002	2014 May 02	149.3835	69.0447	49.7	…	…	…	…	…	…
	30002034004	2014 Nov 15	149.4594	69.0778	54.5	…	…	…	…	…	…
	30002034006	2015 Apr 06	149.4038	69.0677	44.3	…	…	…	…	…	…
	30002034008	2015 May 16	149.3901	69.0381	50.3	…	…	…	…	…	…
IC 342	30002032002	2012 Aug 10	56.5500	68.0815	17.5	*XMM-Newton*	0693850601	2012 Aug 11	56.4305	68.1026	24.3
	30002032003	2012 Aug 10	56.5393	68.1033	80.6	*XMM-Newton*	0693851301	2012 Aug 17	56.4315	68.1038	27.8
	30002032005	2012 Aug 16	56.5439	68.1020	112.8	…	…	…	…	…	…
	90201039002	2016 Oct 16	56.4568	68.1026	44.4	…	…	…	…	…	…
M31	50026001002	2015 Feb 06	10.8508	41.3004	106.4	*Chandra*	17008	2015 Oct 06	11.0654	41.3876	49.1
	50026002001	2015 Feb 08	11.0826	41.3762	109.2	*Chandra*	17011	2015 Oct 08	11.3757	41.7235	49.4
	50026003002	2015 Feb 11	11.3306	41.5763	107.0	*Chandra*	17010	2015 Oct 19	11.2461	41.5343	49.4
	50026001004	2015 Mar 01	10.8535	41.2919	104.3	*Chandra*	17009	2015 Oct 26	11.0174	41.5775	49.4
	50026002003	2015 Mar 06	11.0821	41.3688	104.0	…	…	…	…	…	…
	50026003003	2015 Mar 08	11.3277	41.5753	15.3	…	…	…	…	…	…
	50111001002	2015 Jun 26	10.8878	41.3078	104.1	…	…	…	…	…	…
	50110001002	2015 Jul 25	10.8817	41.3043	52.2	…	…	…	…	…	…
	50110002002	2015 Jul 27	11.1122	41.3753	34.0	…	…	…	…	…	…
	50110002004	2015 Jul 29	11.1126	41.3749	30.6	…	…	…	…	…	…
	50110001004	2015 Aug 01	10.8822	41.2990	71.4	…	…	…	…	…	…
	50110002006	2015 Aug 05	11.1047	41.3758	38.0	…	…	…	…	…	…
	50110003002	2015 Aug 17	11.3425	41.5610	96.4	…	…	…	…	…	…
	50101001002	2015 Sep 13	10.6413	41.2401	98.6	…	…	…	…	…	…
	50111002002	2015 Oct 10	11.1285	41.3694	94.8	…	…	…	…	…	…
	50111003002	2015 Oct 23	11.3704	41.5913	105.4	…	…	…	…	…	…
M81	60101049002	2015 May 18	148.8056	69.0481	181.5	*XMM-Newton*	0111800101	2001 Apr 22	148.8992	69.0380	76.8
M82	80002092002	2014 Jan 23	148.8576	69.6987	59.7	*XMM-Newton*	0206080101	2004 Apr 21	148.9516	69.6523	41.4
	80002092004	2014 Jan 25	148.8647	69.7010	77.4	*XMM-Newton*	0560590301	2009 Apr 29	148.9692	69.6508	11.9
	80002092006	2014 Jan 28	148.8511	69.7064	271.4	*XMM-Newton*	0657802301	2011 Nov 21	148.9263	69.7053	8.1
	80002092007	2014 Feb 04	148.8804	69.6876	260.0	*Chandra*	16580	2014 Feb 03	148.9116	69.6716	46.8

Table 2
(Continued)

Galaxy	*NuSTAR* ObsID	Date	R.A. (J2000.0)	Decl. (J2000.0)	Livetime ks	Observatory	ObsID	Date	R.A. (J2000.0)	Decl. (J2000.0)	Livetime ks
	80002092008	2014 Feb 10	148.8779	69.6835	26.5	*Chandra*	17578	2015 Jan 16	148.8175	69.7153	9.1
	80002092009	2014 Feb 11	148.8538	69.6884	98.2	*Chandra*	16023	2015 Jan 20	148.9160	69.6913	10.0
	80002092011	2014 Mar 03	148.8121	69.6800	98.2	*Chandra*	17678	2015 Jun 21	149.1251	69.6900	9.3
	50002019002	2015 Jan 15	148.9231	69.7165	23.6	*Chandra*	18062	2016 Jan 26	149.0273	69.7373	23.2
	50002019004	2015 Jan 19	148.9173	69.7115	134.0	*Chandra*	18063	2016 Feb 24	148.9199	69.7380	23.2
	90101005002	2015 Jun 20	148.9232	69.6533	30.9	*Chandra*	18064	2016 Apr 05	148.8330	69.7179	23.2
	80202020002	2016 Jan 26	148.9121	69.6979	30.2	*Chandra*	18068	2016 Apr 24	149.0902	69.6418	23.2
	80202020004	2016 Feb 23	148.8794	69.6918	23.7	*Chandra*	18069	2016 Jun 03	149.1305	69.6724	23.2
	80202020006	2016 Apr 05	148.8780	69.6804	26.5	*Chandra*	18067	2016 Jul 01	149.1182	69.7019	24.1
	30101045002	2016 Apr 15	148.8957	69.6743	163.3	…	…	…	…	…	…
	80202020008	2016 Apr 24	148.8943	69.6729	35.7	…	…	…	…	…	…
	90202038002	2016 Oct 07	149.0146	69.6776	38.7	…	…	…	…	…	…
	90202038004	2016 Nov 30	148.9574	69.6900	36.3	…	…	…	…	…	…
M83	50002043002	2013 Aug 07	204.2200	−29.8677	42.3	*XMM-Newton*	0723450101	2013 Aug 07	204.2760	−29.8969	41.6
	50002043004	2013 Aug 09	204.2270	−29.8744	79.7	*XMM-Newton*	0723450201	2014 Jan 11	204.2626	−29.8407	25.1
	50002043006	2013 Aug 21	204.2160	−29.8675	42.5	*Chandra*	16024	2014 Jun 07	204.2509	−29.8767	29.6
	50002043008	2014 Jan 19	204.3021	−29.8458	81.0	…	…	…	…	…	…
	50002043010	2014 Jun 04	204.2388	−29.8793	70.4	…	…	…	…	…	…
	50002043012	2014 Jun 07	204.2380	−29.8791	109.4	…	…	…	…	…	…
NGC 1313	30002035002	2012 Dec 16	49.6268	−66.5225	100.2	*XMM-Newton*	0693850501	2012 Dec 16	49.6311	−66.4993	60.9
	30002035004	2012 Dec 21	49.6351	−66.5268	126.4	*Chandra*	14676	2012 Dec 17	49.5101	−66.5812	9.8
	80001032002	2014 Jul 05	49.5764	−66.4456	63.0	*XMM-Newton*	0693851201	2012 Dec 22	49.6330	−66.5027	61.3
	90201050002	2017 Mar 29	49.5047	−66.4958	64.1	*Chandra*	15594	2012 Dec 23	49.5102	−66.5812	9.8
	…	…	…	…	…	*XMM-Newton*	0742590301	2014 Jul 05	49.5016	−66.4904	50.6
NGC 253	50002031002	2012 Sep 01	11.9200	−25.2719	156.5	*Chandra*	13830	2012 Sep 02	11.8901	−25.2803	19.7
	50002031004	2012 Sep 15	11.9143	−25.2805	157.6	*Chandra*	13831	2012 Sep 18	11.8941	−25.2818	19.7
	50002031006	2012 Nov 16	11.8900	−25.3178	124.5	*Chandra*	13832	2012 Nov 16	11.8967	−25.2921	19.7
NGC 4945	60002051002	2013 Feb 10	196.4060	−49.4605	45.0	*XMM-Newton*	0204870101	2004 Jan 10	196.3473	−49.4435	18.3
	60002051004	2013 Jun 15	196.3271	−49.4610	54.4	*Chandra*	14985	2013 Apr 20	196.3682	−49.4664	68.7
	60002051006	2013 Jul 05	196.3334	−49.4907	34.2	*Chandra*	14984	2013 Apr 25	196.3686	−49.4668	128.8
NGC 5204	30002037002	2013 Apr 19	202.3756	58.4400	95.7	*XMM-Newton*	0693851401	2013 Apr 21	202.3691	58.3993	12.3
	30002037004	2013 Apr 29	202.3658	58.4413	77.3	*Chandra*	14675	2013 Apr 21	202.3968	58.4149	9.8
	…	…	…	…	…	*XMM-Newton*	0693850701	2013 Apr 29	202.3733	58.3966	6.1
	…	…	…	…	…	*Chandra*	15603	2013 May 01	202.4004	58.4124	9.8

Note. Simultaneous/archival *NuSTAR* and *Chandra*/*XMM-Newton* observations for galaxies in the sample (Table 1). Livetime represents the exposure time of the cleaned event file (Section 4).

calculations. We also inspected light curves to ensure no flares were present. We only used observing mode 01 event data for both focal plane modules A and B throughout our analysis. The resulting total exposure times for each observation after applying all these corrections/filters are listed in Table 2.

We computed the background for each telescope (FPMA/B) in each observation for each galaxy using the publicly available tool NUSKYBGD (Wik et al. 2014a). The *NuSTAR* background is comprised of stray light (from the cosmic X-ray background or bright sources outside the FOV), reflected solar X-rays, the focused cosmic X-ray background, and the instrumental background. Due to the spectral and spatial variation of the background across even individual detectors, accurate modeling is required to produce background images at source locations. For each observation, we created four source-free[12] box regions for each of the detectors (0−3) of each telescope (A and B) for fitting a background model (see Wik et al. 2014a for an example). Stray light from bright sources within approximately 1°–5° of the optical axis can cause significant contamination in addition to the aperture background component. Stray light was only an issue for M83 (see Yukita et al. 2016). We were able to overcome this issue by excluding data from telescope B in the 2014 Jan observation and excluding telescope A data for the remaining observations.

4.2. Chandra *and* XMM-Newton

Reduction of *Chandra* ACIS observations was performed using the CHANDRA INTERACTIVE ANALYSIS OF OBSERVATIONS (CIAO) tools package version 4.7.2 (Fruscione et al. 2006) and the CHANDRA CALIBRATION DATABASE (CALDB) version 4.8 (Graessle et al. 2006). *Chandra* data were reduced using the CHANDRA_REPRO script. Events files were filtered using the standard (ASCA) grades (0, 2–4, 6), status bits (0), good time intervals, and CCD chips (I0-I3 for ACIS-I and S3 for ACIS-S). We then created exposure maps and exposure-corrected images using FLUXIMAGE with a bin size of 1 in the 4–8 keV energy band. Source lists were created with WAVDETECT using the $\sqrt{2}$ series from 1–8 for the *scales* parameter and corresponding exposure maps to reduce false positives. Default settings were used for all other parameters.

XMM-Newton data were reduced using SAS v.16.0.0. Level 1 event data were processed using the EPCHAIN and EMCHAIN scripts. High-background intervals were filtered using the PN-FILTER and MOS-FILTER scripts. We created 4–10 keV images using single- and double-pixel events (PATTERN 0−4) for the PN detector and single- to quadruple-pixel events (PATTERN 0−12) from the MOS detector. Source lists were created using EDETECT_CHAIN with 16 spline nodes and a likelihood threshold of 6 to include faint sources.

4.3. NuSTAR *Point Source Detection via PSF Fitting*

Point source detection in *NuSTAR* images can be complicated in regions with a high spatial density of comparably bright point sources such as those present in many galaxies. The moderate-quality 18″ PSF core FWHM can lead to source confusion and/or PSF contamination by sources within 58″ (corresponding to the *NuSTAR* PSF half-power diameter). Therefore, we used simultaneous or archival *Chandra* and *XMM-Newton* observations to create point source lists to localize and determine source characteristics in the *NuSTAR* observations. For each galaxy we merged the *NuSTAR* imaging data from telescopes A and B to increase the signal-to-noise ratio. Exposure times for *Chandra* and/or *XMM-Newton* observations were sufficient to reach below the sensitivity limits of the combined *NuSTAR* observations for each galaxy. The methodology outlined here follows that in Wik et al. (2014b).

4.3.1. PSF and Response File Generation

Due to *NuSTAR*'s 58″ PSF half-power diameter and 18″ PSF core FWHM, source confusion is an issue in crowded fields. To accurately determine a source's count rate, we modeled the PSF of each source to deconvolve the contribution from nearby sources. The PSF shape changes more dramatically once sources are >3′ off-axis, such that pointing variations over the course of an observation can induce errors in the PSF shape. We created composite PSFs for each source using PSF model images from the CALDB that were weighted by the time spent at each off-axis angle. The same procedure was applied to determine the vignetting function, which represents the effective area and is dependent on both off-axis angle and energy. The average vignetting of an image with a given energy band is found by weighting the vignetting function over that energy range by a power-law spectrum typical of XRBs with $\Gamma = 1.7$, to ensure the calculated vignetting function is appropriately weighted for the sources we are studying. The weighting was used to prevent the higher-energy vignetting from influencing our results, due to *NuSTAR* having a strongly energy-dependent vignetting function (e.g., Harrison et al. 2013; Madsen et al. 2015). ARFs were created by multiplying the on-axis ARF from the CALDB by the weighted vignetting function. RMFs were created using the appropriate response file from the CALDB. ARFs and RMFs were created for each source and were used to obtain corrected count rates. The overall result was count rates that were the same as those expected for an on-axis source.

4.3.2. PSF Fitting and Astrometric Alignment

Using the previously described techniques for generating data products, we determined the astrometric shifts for every observation and count rates via PSF fitting. We used the *Chandra*/*XMM-Newton* source positions as the reference coordinate system and used the brightest few sources to determine the (x/y) image shifts of the *NuSTAR* data. This was completed for every ObsID in the galaxy sample using the 4–25 keV images. These shifts were then applied to the images and the PSF fitting routine was executed again to determine count rates without fitting for image shifts. To reach the lowest sensitivity limits for each galaxy, we merged data from both *NuSTAR* telescopes A and B and combined all observations.

The *Chandra*/*XMM-Newton* source positions for the brightest sources were used as inputs for the fitting procedure. The composite PSFs and response files were created for each source in a rectangular region that included all sources with overlapping PSFs in the region. A background image was created at each source location using the background model computed for each focal plane module in an observation. A model image was created by combining the PSF and background images, which was then fit to the actual data using the Cash statistic (Cash 1979). The Cash statistic was

[12] Created by masking out visually identifiable sources in an image.

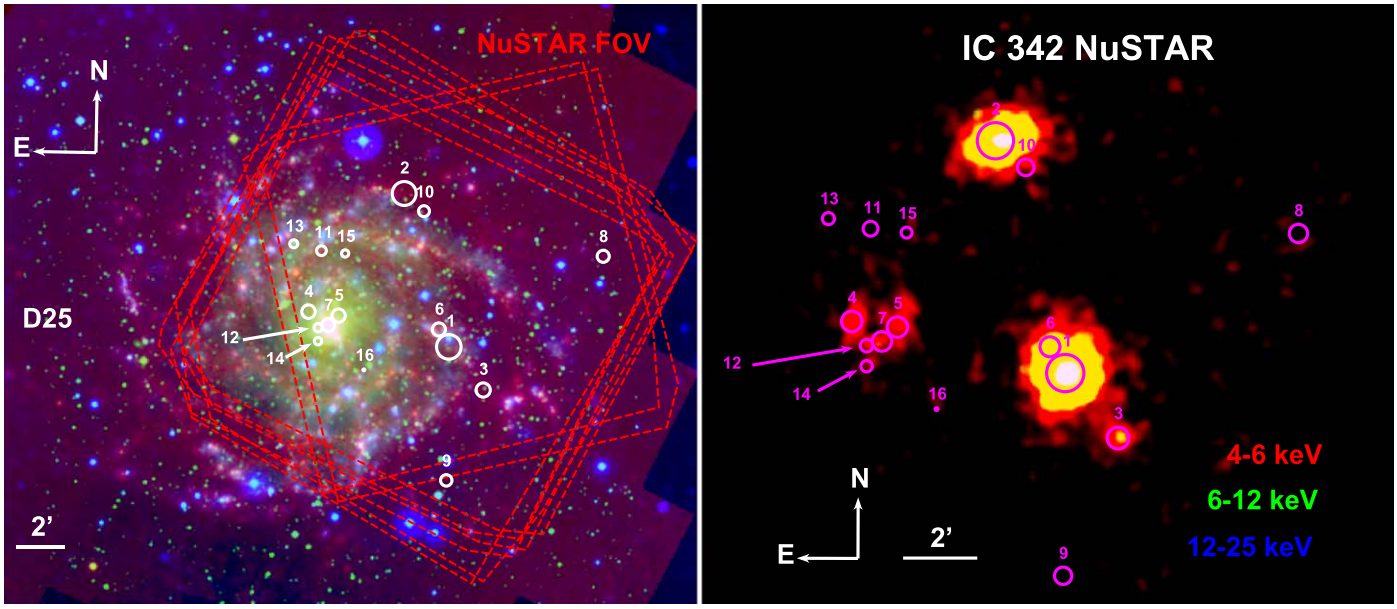

Figure 3. Example images for the *NuSTAR* observations of IC 342. Left: three-color image of IC 342 from *GALEX* NUV (blue), Hα (green), and *Spitzer* 24 μm (red). The *NuSTAR* observations of IC 342 are outlined in red (Table 2, telescopes A and B), whereas the D_{25} ellipse (white) is larger than the FOV (Table 1) and cuts through the top right corner. The numbers represent the detected *NuSTAR* X-ray point sources from Table 3, where circle sizes are proportional to a 4–25 keV count rate. Right: false-color *NuSTAR* image smoothed by a Gaussian of 7 pixels. Magenta numbers are identical to those in the left panel.

minimized using the Amoeba algorithm (Press et al. 2002), which is ideal for models without derivatives. Count-rate errors were estimated by completing 1000 Monte Carlo simulations of the best-fitting model. During the process if a better fit was found, then the original model parameters were reset and fitting was repeated. The 90% uncertainty range was calculated from the inner 900 sorted values for each simulated parameter. We determined count rates in the soft (S, 4−6 keV), medium (M, 6−12 keV), hard, (H, 12–25 keV), and full (F, 4–25 keV) *NuSTAR* energy bands because they provided the most robust separation between sources (see Section 5.1). The same source positions were used when fitting each energy band. We omitted all sources with count rates $<10^{-4}$ counts s^{-1} in each energy band and required that a source was detected (count rate above the 90% confidence threshold) in at least one energy band. In Figure 3 we show an example of the *NuSTAR* data and detected *NuSTAR* point sources for IC 342.

4.3.3. Simultaneous PSF Fitting

Our goals of identifying the accretion states and compact object types of *NuSTAR* point sources rely on using hardness-intensity and color–color diagrams. However, the hardness ratio uncertainties can be prohibitively large due to error propagation from count rates. To improve our methodology we used the technique developed by D. Wik et al. (2018, in preparation). Briefly, the soft, medium, and hard energy band images were fit simultaneously—with the PSF models described in Section 4.3.2—using hardness ratios and the full (4–25 keV) count rate as free parameters instead of the S, M, and H rates themselves. The hardness ratios $HR1 = (M - S)/(M + S)$ and $HR2 = (H - M)/(H + M)$, as well as the full energy band $F = S + M + H$ were free parameters in the fit instead of fitting individual energy bands to determine count rates. In order to use F, $HR1$, and $HR2$ as free parameters we defined the variables $C = (1-HR1)/(1+HR1)$ and $D = (1+HR2)/(1-HR2)$ to convert to count rates in each energy band:

$$S = \frac{FC}{1 + C + D}, M = \frac{F}{1 + C + D}, H = \frac{FD}{1 + C + D}. \quad (4)$$

By changing the free parameters, we were able to directly calculate uncertainty ranges on the hardness ratios from the data itself, which avoids error propagation (and any assumptions behind that method) from introducing new systematic uncertainties. This method allowed uncertainties for fainter sources to be calculated more accurately, which allowed better limits to be derived when a source was not detected in one of the energy bands. We used the same source positions that were used for fitting each energy band in Section 4.3.2 such that there was no variation in source positions between methods. In Table 3 we list the count rates in each energy band (S, M, H, and F) and their 90% upper and lower confidence intervals that were derived from individual PSF fitting of each energy band (Section 4.3.2). The S, M, and H count rates were not derived from simultaneous PSF fitting using Equation (4) because their propagated uncertainties are poorly constrained compared to individual PSF fitting of each energy band. Sources were grouped by galaxy and numbered in order of decreasing 4–25 keV count rate. We also show the hardness ratios $HR1$ and $HR2$ and their uncertainties from the simultaneous PSF fitting of the soft, medium, and hard energy bands summarized in this section. The 4–25 keV luminosity was estimated by converting the 4–25 keV count rate (derived from simultaneous PSF fitting summarized in this section) assuming a spectral model typical of XRBs, with $\Gamma = 1.7$ and $N_{\rm H}$ values from Table 1. We estimated the influence of using $\Gamma = 1$ for sources classified as pulsars (see Section 5.1) and found a <10% difference in count rates, corresponding to <0.05 shift in color space for pulsars. This

Table 3
NuSTAR Point Source Properties

Galaxy	ID	R.A. (J2000.0)	Decl. (J2000.0)	*NuSTAR* Count Rates (10^{-4} counts s^{-1}) (4 − 6 keV)	σ_{up}	σ_{down}	(6 − 12 keV)	σ_{up}	σ_{down}	(12–25 keV)	σ_{up}	σ_{down}	(4–25 keV)	σ_{up}	σ_{down}	*NuSTAR* colors HR1	σ_{up}	σ_{down}	HR2	σ_{up}	σ_{down}	*NuSTAR* L_X (10^{38} erg s^{-1}) (4–25 keV)	σ_{up}	σ_{down}	Type	State
Circinus	1	213.162556	−65.392239	445.43	4.68	4.57	401.37	4.58	4.45	39.48	1.92	1.85	1078.08	8.11	8.11	−0.04	0.01	0.01	−0.80	0.01	0.01	113.98	0.86	0.86	BH	ULX
Circinus	2	213.291263	−65.345541	114.42	9.28	9.14	324.15	14.37	14.14	116.70	13.62	13.51	589.66	24.31	24.22	0.53	0.04	0.04	−0.49	0.05	0.05	62.34	2.57	2.56	NS	AP
Circinus	3	213.079532	−65.433248	4.78	1.58	1.36	9.38	1.93	1.73	4.78	1.82	1.56	16.18	2.58	2.41	0.35	0.17	0.16	−0.42	0.18	0.21	1.71	0.27	0.25	NS	AP
Circinus	4	213.253387	−65.429618	4.89	1.49	1.30	4.15	1.69	1.47	1.91	0.00	0.00	11.92	2.39	1.97	−0.14	0.17	0.18	−0.56	0.00	0.00	1.26	0.25	0.21	BH	···
IC 342	1	56.479998	68.081921	365.84	3.63	3.62	458.99	4.05	4.03	87.25	1.97	1.94	1065.63	6.82	6.85	0.11	0.01	0.01	−0.68	0.01	0.01	73.40	0.47	0.47	BH	ULX
IC 342	2	56.564447	68.186753	258.74	3.54	3.51	401.89	4.43	4.32	100.29	2.70	2.66	883.17	7.23	7.13	0.21	0.01	0.01	−0.59	0.01	0.01	60.83	0.50	0.49	BH	ULX
IC 342	3	56.416343	68.052534	23.07	1.23	1.21	21.81	1.32	1.25	3.50	0.89	0.79	56.64	2.28	2.19	−0.03	0.04	0.04	−0.71	0.06	0.06	3.90	0.16	0.15	BH	I
IC 342	4	56.738231	68.105118	23.86	1.65	1.52	14.15	1.50	1.42	0.84	0.00	0.00	46.01	2.66	2.53	−0.27	0.05	0.05	−0.89	0.00	0.00	3.17	0.18	0.17	BH	···
IC 342	5	56.683009	68.102598	18.58	1.51	1.42	16.73	1.53	1.43	1.00	0.00	0.00	44.89	2.74	2.62	−0.08	0.06	0.06	−0.78	0.00	0.00	3.09	0.19	0.18	···	···
IC 342	6	56.498453	68.093783	17.59	1.92	1.84	16.24	1.95	1.90	3.24	1.04	0.99	41.58	3.46	3.40	−0.03	0.09	0.08	−0.69	0.10	0.10	2.86	0.24	0.23	BH	I
IC 342	7	56.701628	68.096126	12.15	1.76	1.65	16.29	1.86	1.76	4.11	1.22	1.10	38.21	3.29	3.12	0.15	0.09	0.09	−0.60	0.10	0.10	2.63	0.23	0.21	NS	ZA
IC 342	8	56.197127	68.144554	8.20	1.56	1.42	8.34	1.79	1.65	1.74	0.00	0.00	30.79	2.82	2.67	0.03	0.09	0.09	−0.51	0.14	0.16	2.12	0.19	0.18	BH	I
IC 342	9	56.482757	67.990453	5.09	1.83	1.57	10.70	2.45	2.20	2.40	0.00	0.00	25.66	3.52	3.30	0.29	0.13	0.13	−0.33	0.00	0.00	1.77	0.24	0.23	···	···
IC 342	10	56.527707	68.174742	8.36	1.34	1.28	10.79	1.54	1.45	4.75	1.19	1.09	22.48	2.53	2.39	0.39	0.14	0.13	−0.30	0.12	0.11	1.55	0.17	0.16	NS	AP
IC 342	11	56.715792	68.146976	2.97	1.00	0.89	6.97	1.24	1.14	3.69	1.36	1.22	16.06	2.27	2.15	0.49	0.17	0.15	−0.29	0.15	0.17	1.11	0.16	0.15	NS	AP
IC 342	12	56.720147	68.094210	4.56	1.71	1.57	1.67	0.00	0.00	1.11	0.00	0.00	10.48	2.96	2.70	−0.18	0.29	0.30	−0.47	0.00	0.00	0.72	0.20	0.19	···	···
IC 342	13	56.766922	68.151472	4.62	1.21	1.06	1.21	0.00	0.00	1.40	0.00	0.00	9.64	2.48	2.09	−0.31	0.00	0.00	0.09	0.00	0.00	0.66	0.17	0.14	···	···
IC 342	14	56.720092	68.084930	2.90	1.23	1.08	1.27	0.00	0.00	1.11	0.00	0.00	8.25	2.36	2.21	−0.10	0.31	0.30	−0.02	0.00	0.00	0.57	0.16	0.15	···	···
IC 342	15	56.672095	68.145262	2.91	0.88	0.79	0.93	0.00	0.00	0.99	0.00	0.00	7.75	1.81	1.67	−0.14	0.22	0.24	0.03	0.00	0.00	0.53	0.12	0.12	···	···
IC 342	16	56.635542	68.065637	2.42	0.76	0.66	2.66	0.84	0.74	0.84	0.00	0.00	6.60	1.40	1.40	0.04	0.20	0.20	0.41	0.00	0.00	0.12	0.00	0.00	···	···
NGC 4945	1	196.408793	−49.429173	31.83	7.65	7.77	29.81	6.98	6.58	3.63	0.00	0.00	73.98	13.09	12.34	−0.02	0.19	0.16	−0.81	0.00	0.00	6.14	1.09	1.02	NS	ZA
NGC 4945	2	196.355946	−49.473268	9.07	0.00	0.00	27.48	7.39	7.34	7.68	0.00	0.00	67.05	13.24	12.02	0.01	0.19	0.18	−0.61	0.00	0.00	5.56	1.10	1.00	···	···
NGC 4945	3	196.296232	−49.524091	12.99	1.60	1.49	21.33	2.05	1.95	1.78	0.00	0.00	46.40	3.45	3.29	0.24	0.07	0.07	−0.73	0.00	0.00	3.85	0.29	0.27	NS	ZA
NGC 4945	4	196.387047	−49.459326	41.37	2.98	2.84	29.17	3.60	3.45	5.18	0.00	0.00	39.96	4.58	4.49	−0.44	0.00	0.00	−0.83	0.00	0.00	3.31	0.38	0.37	BH	S
NGC 4945	5	196.338298	−49.461319	5.27	0.00	0.00	5.40	0.00	0.00	1.66	0.00	0.00	31.45	4.18	4.01	−0.06	0.13	0.15	−0.92	0.00	0.00	2.61	0.35	0.33	NS	ZA
NGC 4945	6	196.327271	−49.473171	12.04	2.23	2.10	16.31	2.61	2.53	1.62	0.00	0.00	30.30	3.79	3.64	0.04	0.12	0.13	−0.93	0.00	0.00	2.51	0.31	0.30	NS	ZA
NGC 4945	7	196.404702	−49.426126	5.81	0.00	0.00	5.33	0.00	0.00	8.77	2.46	2.53	29.79	9.82	8.93	0.31	0.93	0.42	0.01	0.00	0.00	2.47	0.81	0.74	···	···
NGC 4945	8	196.412435	−49.424898	3.83	0.00	0.00	12.22	3.81	3.64	2.85	0.00	0.00	23.61	7.03	6.67	0.34	0.49	0.29	−0.42	0.00	0.00	1.96	0.58	0.55	NS	AP
NGC 4945	9	196.397906	−49.486358	12.65	1.65	1.53	9.77	1.96	1.84	2.68	0.00	0.00	15.00	2.73	2.55	−0.22	0.00	0.00	−0.66	0.00	0.00	1.24	0.23	0.21	BH	S
NGC 4945	10	196.343820	−49.493043	2.25	0.00	0.00	6.50	2.53	2.43	1.83	0.00	0.00	13.70	3.44	3.31	0.08	0.27	0.29	−0.85	0.00	0.00	1.14	0.29	0.27	NS	ZA
NGC 4945	11	196.438717	−49.489241	1.10	0.00	0.00	4.56	1.46	1.35	1.68	0.00	0.00	8.24	2.64	2.11	0.24	0.00	0.00	−0.45	0.00	0.00	0.68	0.22	0.18	···	···
NGC 4945	12	196.375811	−49.413063	1.25	0.00	0.00	4.07	1.52	1.39	1.74	0.00	0.00	7.82	2.88	2.35	0.17	0.40	0.36	−0.42	0.00	0.00	0.65	0.24	0.19	···	···
Holmberg II	1	124.869805	70.705453	288.82	3.49	3.51	305.27	3.66	3.59	42.73	1.68	1.64	752.54	6.51	6.37	0.02	0.01	0.01	−0.75	0.01	0.01	48.23	0.42	0.41	BH	ULX
Holmberg II	2	124.788852	70.657370	6.99	0.95	0.87	11.90	1.30	1.19	2.61	1.07	0.95	29.96	2.20	2.12	0.25	0.07	0.07	−0.57	0.10	0.10	1.92	0.14	0.14	···	···
Holmberg II	3	124.790615	70.777998	5.59	0.00	0.00	6.95	1.37	1.25	4.30	1.51	1.37	24.31	2.59	2.47	0.13	0.11	0.11	−0.25	0.14	0.16	1.56	0.17	0.16	BH	H
Holmberg II	4	124.666558	70.767633	1.69	0.00	0.00	5.88	2.02	1.79	2.23	0.00	0.00	21.81	3.98	3.69	0.20	0.21	0.20	−0.17	0.21	0.26	1.40	0.26	0.24	BH	H
Holmberg II	5	124.616683	70.714178	3.05	1.43	1.23	1.71	0.00	0.00	0.90	0.00	0.00	11.56	2.96	2.57	−0.05	0.24	0.27	−0.56	0.00	0.00	0.74	0.19	0.16	···	···
Holmberg II	6	124.967121	70.711546	2.87	0.97	0.86	4.22	1.11	1.03	2.10	0.93	0.79	11.00	1.94	1.84	0.33	0.22	0.20	−0.31	0.19	0.20	0.70	0.12	0.12	···	···
M81	1	148.886846	69.009754	95.39	2.71	2.59	107.25	2.81	2.69	22.62	1.50	1.43	262.46	4.87	4.75	0.07	0.02	0.02	−0.64	0.02	0.02	20.50	0.38	0.37	BH	ULX
M81	2	148.908881	69.067523	27.00	7.21	7.03	34.60	8.35	8.30	4.79	0.00	0.00	84.01	14.08	14.06	0.10	0.19	0.18	−0.37	0.00	0.00	6.56	1.10	1.10	···	···
M81	3	148.956128	69.092627	22.42	2.41	2.31	26.49	2.00	1.92	1.19	0.00	0.00	52.47	3.86	3.72	0.21	0.08	0.07	−0.76	0.00	0.00	4.10	0.30	0.29	NS	ZA
M81	4	148.792621	69.084213	20.26	1.74	1.61	18.20	1.79	1.71	1.12	0.00	0.00	43.59	3.05	2.96	0.05	0.07	0.07	−0.69	0.00	0.00	3.40	0.24	0.23	NS	ZA
M81	5	148.753974	69.124464	7.61	1.85	1.69	12.02	2.27	2.13	5.74	1.94	1.74	40.23	4.25	4.09	0.19	0.11	0.11	−0.40	0.13	0.13	3.14	0.33	0.32	BH	H
M81	6	148.749554	69.129380	9.11	2.04	1.85	11.39	2.41	2.19	1.96	0.00	0.00	29.85	4.36	4.11	0.09	0.14	0.14	−0.45	0.00	0.00	2.33	0.34	0.32	···	···
M81	7	149.010120	68.993406	2.31	0.99	0.91	3.50	1.23	1.12	2.80	1.31	1.17	17.83	2.36	2.23	0.20	0.14	0.14	−0.21	0.16	0.18	1.39	0.18	0.17	BH	H
M81	8	148.955677	69.136729	3.34	1.16	1.04	3.91	1.34	1.18	0.80	0.00	0.00	17.68	2.65	2.19	0.06	0.13	0.13	−0.74	0.00	0.00	1.38	0.21	0.17	NS	ZA
M81	9	148.956347	68.977013	2.07	0.97	0.86	1.12	0.00	0.00	1.18	0.00	0.00	11.12	2.20	2.05	0.07	0.20	0.20	−0.13	0.00	0.00	0.87	0.17	0.16	···	···
M81	10	148.740078	69.045188	3.19	0.95	0.86	1.03	0.00	0.00	0.45	0.00	0.00	6.83	1.68	1.54	−0.01	0.25	0.26	−0.66	0.00	0.00	0.53	0.13	0.12	···	···
Holmberg IX	1	149.471230	69.063248	881.68	3.90	3.90	1104.69	4.28	4.38	209.73	2.04	2.06	2572.42	7.58	7.53	0.11	0.00	0.00	−0.68	0.00	0.00	219.14	0.65	0.64	BH	ULX
Holmberg IX	2	149.700595	69.092578	7.08	0.84	0.77	12.64	1.02	1.00	2.55	0.91	0.86	35.32	1.92	1.86	0.20	0.05	0.05	−0.60	0.07	0.08	3.01	0.16	0.16	NS	ZA
Holmberg IX	3	149.246174	69.072843	5.47	0.85	0.82	7.15	0.98	0.91	2.44	0.00	0.00	28.45	1.81	1.77	0.09	0.06	0.06	−0.43	0.09	0.09	2.42	0.15	0.15	BH	H

Table 3
(Continued)

Galaxy	ID	R.A. (J2000.0)	Decl. (J2000.0)	*NuSTAR* Count Rates (4 − 6 keV)	σ_{up}	σ_{down}	(6 − 12 keV)	σ_{up}	σ_{down}	(12–25 keV)	σ_{up}	σ_{down}	(4–25 keV)	σ_{up}	σ_{down}	*NuSTAR* colors HR1	σ_{up}	σ_{down}	HR2	σ_{up}	σ_{down}	*NuSTAR* L_X (4–25 keV)	σ_{up}	σ_{down}	Type	State
				(10^{-4} counts s^{-1})																		(10^{38} erg s^{-1})				
Holmberg IX	4	149.401430	69.001676	2.89	0.63	0.59	4.37	0.76	0.72	2.64	0.00	0.00	13.10	1.29	1.25	0.17	0.10	0.10	−0.43	0.13	0.14	1.12	0.11	0.11	BH	H
Holmberg IX	5	149.701622	69.013395	0.67	0.00	0.00	0.83	0.00	0.00	0.99	0.00	0.00	11.18	1.77	1.66	−0.01	0.17	0.18	−0.09	0.22	0.25	0.95	0.15	0.14	BH	H
Holmberg IX	6	149.264037	69.056331	1.65	0.65	0.60	1.97	0.79	0.70	0.70	0.00	0.00	9.58	1.40	1.34	0.14	0.15	0.15	−0.23	0.00	0.00	0.82	0.12	0.11	⋯	⋯
Holmberg IX	7	149.403636	69.124751	0.62	0.00	0.00	2.81	0.73	0.68	0.69	0.00	0.00	9.54	1.31	1.24	0.30	0.15	0.14	−0.36	0.16	0.18	0.81	0.11	0.11	BH	H
Holmberg IX	8	149.527654	69.076959	5.57	1.10	1.00	2.89	1.07	1.02	0.65	0.00	0.00	5.74	1.74	1.31	0.69	0.00	0.00	−0.22	0.00	0.00	0.49	0.15	0.11	NS	AP
NGC 5204	1	202.410891	58.418104	90.90	2.81	2.58	97.78	2.47	2.40	14.38	1.31	1.25	246.82	4.05	3.92	0.03	0.02	0.02	−0.73	0.02	0.02	35.23	0.58	0.56	BH	ULX
NGC 5204	2	202.365137	58.426330	5.67	1.45	1.37	0.95	0.00	0.00	0.86	0.00	0.00	10.78	2.64	2.30	−0.25	0.23	0.25	−0.51	0.00	0.00	1.54	0.38	0.33	BH	S
NGC 5204	3	202.357118	58.424131	2.46	0.00	0.00	5.01	1.10	0.99	2.27	0.00	0.00	9.85	2.56	2.40	0.20	0.43	0.33	0.06	0.00	0.00	1.41	0.37	0.34	⋯	⋯
NGC 1313	1	49.583262	−66.486433	251.07	2.56	2.52	309.54	2.83	2.81	59.09	1.45	1.41	728.94	4.97	4.88	0.10	0.01	0.01	−0.68	0.01	0.01	78.92	0.54	0.53	BH	ULX
NGC 1313	2	49.592608	−66.600926	98.98	2.27	2.16	69.05	2.07	2.00	9.66	1.39	1.29	215.88	3.98	3.89	−0.17	0.02	0.02	−0.73	0.03	0.03	23.37	0.43	0.42	BH	ULX
NGC 1313	3	49.576007	−66.500731	23.27	1.69	1.62	28.30	1.77	1.71	3.47	0.89	0.87	64.43	3.09	3.03	0.11	0.05	0.05	−0.76	0.05	0.05	6.98	0.33	0.33	NS	ZA
NGC 1313	4	49.410931	−66.551014	17.97	1.22	1.16	14.25	1.26	1.19	1.09	0.00	0.00	44.62	2.40	2.30	−0.12	0.05	0.05	−0.65	0.00	0.00	4.83	0.26	0.25	BH	I
NGC 1313	5	49.453570	−66.512900	4.43	0.73	0.68	5.58	0.85	0.79	2.46	0.85	0.79	17.91	1.59	1.55	0.06	0.09	0.09	−0.31	0.12	0.13	1.94	0.17	0.17	BH	H
NGC 1313	6	49.849423	−66.584843	3.20	0.97	0.87	5.53	1.29	1.18	1.42	0.00	0.00	16.70	2.45	2.31	0.17	0.13	0.14	−0.28	0.00	0.00	1.81	0.27	0.25	⋯	⋯
NGC 1313	7	49.887555	−66.532604	2.97	0.99	0.88	4.77	1.19	1.16	1.26	0.00	0.00	14.77	2.31	2.19	0.11	0.15	0.15	−0.30	0.00	0.00	1.60	0.25	0.24	⋯	⋯
NGC 1313	8	49.857416	−66.496388	0.96	0.00	0.00	5.38	1.26	1.16	1.22	0.00	0.00	13.16	2.38	2.24	0.29	0.19	0.17	−0.41	0.00	0.00	1.42	0.26	0.24	NS	AP
NGC 1313	9	49.588208	−66.509542	5.67	1.05	1.01	2.70	1.05	1.00	0.72	0.00	0.00	11.26	1.91	1.84	−0.29	0.16	0.18	−0.40	0.00	0.00	1.22	0.21	0.20	BH	S
NGC 1313	10	49.684068	−66.428079	2.09	0.61	0.57	1.81	0.75	0.70	0.85	0.00	0.00	10.32	1.48	1.41	−0.06	0.15	0.17	−0.05	0.20	0.23	1.12	0.16	0.15	BH	H
NGC 1313	11	49.591024	−66.434908	2.02	0.58	0.53	2.40	0.71	0.66	0.57	0.00	0.00	7.98	1.32	1.21	0.07	0.15	0.15	−0.47	0.00	0.00	0.86	0.14	0.13	⋯	⋯
M83	1	204.271280	−29.868466	58.71	2.12	2.05	41.51	1.92	1.84	3.01	0.96	0.87	129.29	3.56	3.45	−0.15	0.03	0.03	−0.85	0.04	0.04	16.83	0.46	0.45	BH	ULX
M83	2	204.121141	−29.856414	27.35	2.40	2.22	32.63	2.70	2.52	11.72	2.39	2.16	91.78	4.09	3.94	0.08	0.04	0.04	−0.51	0.06	0.06	11.95	0.53	0.51	BH	I
M83	3	204.332434	−29.896720	12.73	1.93	1.80	7.44	1.79	1.63	3.24	0.00	0.00	54.55	3.39	3.24	−0.16	0.06	0.06	−0.35	0.10	0.10	7.10	0.44	0.42	⋯	⋯
M83	4	204.247658	−29.832904	14.74	1.28	1.20	13.02	1.32	1.25	0.95	0.00	0.00	42.86	2.41	2.32	−0.04	0.05	0.05	−0.70	0.08	0.09	5.58	0.31	0.30	BH	I
M83	5	204.302098	−29.864971	8.58	1.23	1.17	14.35	1.42	1.38	5.99	1.26	1.18	41.31	2.54	2.46	0.24	0.07	0.06	−0.41	0.07	0.07	5.38	0.33	0.32	BH	H
M83	6	204.253488	−29.865445	4.77	0.00	0.00	6.58	0.00	0.00	1.06	0.00	0.00	39.10	7.63	8.20	0.37	0.31	0.22	−0.73	0.00	0.00	5.09	0.99	1.07	NS	⋯
M83	7	204.318179	−29.827451	7.16	1.18	1.10	8.80	1.41	1.32	3.28	1.36	1.24	36.44	2.67	2.55	0.07	0.07	0.07	−0.42	0.10	0.11	4.74	0.35	0.33	BH	H
M83	8	204.279501	−29.850263	14.51	1.34	1.27	8.30	1.22	1.13	0.85	0.00	0.00	33.35	2.37	2.27	−0.21	0.07	0.06	−0.67	0.00	0.00	4.34	0.31	0.30	BH	I
M83	9	204.258357	−29.921444	6.90	0.96	0.88	10.93	1.15	1.11	2.18	0.94	0.85	29.78	2.02	1.94	0.19	0.07	0.07	−0.64	0.09	0.09	3.88	0.26	0.25	NS	ZA
M83	10	204.311241	−29.908424	6.87	1.23	1.15	6.27	1.35	1.26	5.33	1.37	1.25	28.39	2.61	2.48	0.01	0.10	0.10	−0.15	0.12	0.13	3.70	0.34	0.32	BH	H
M83	11	204.181380	−29.851747	10.82	1.45	1.34	9.75	1.53	1.40	0.80	0.00	0.00	27.12	2.26	2.07	0.03	0.08	0.08	−0.88	0.00	0.00	3.53	0.29	0.27	NS	ZA
M83	12	204.320495	−29.893943	7.29	1.33	1.23	8.41	1.50	1.38	5.73	1.42	1.30	23.81	2.85	2.72	0.17	0.14	0.13	−0.24	0.14	0.15	3.10	0.37	0.35	BH	H
M83	13	204.249872	−29.863881	3.02	0.00	0.00	9.69	3.58	3.42	1.55	0.00	0.00	20.65	5.77	5.58	−0.13	0.31	0.30	−0.41	0.00	0.00	2.69	0.75	0.73	⋯	⋯
M83	14	204.236728	−29.820689	3.68	1.00	0.92	4.50	1.10	1.02	0.97	0.00	0.00	17.07	2.14	2.02	0.09	0.12	0.11	−0.55	0.00	0.00	2.22	0.28	0.26	⋯	⋯
M83	15	204.238592	−29.894139	4.69	0.96	0.88	4.88	1.06	0.96	0.59	0.00	0.00	15.60	1.96	1.72	0.03	0.11	0.11	−0.78	0.00	0.00	2.03	0.26	0.22	NS	ZA
M83	16	204.256672	−29.795013	0.93	0.00	0.00	3.93	1.24	1.15	1.18	0.00	0.00	14.09	2.30	2.16	0.25	0.15	0.15	−0.43	0.00	0.00	1.83	0.30	0.28	⋯	⋯
M83	17	204.243149	−29.851161	0.96	0.00	0.00	4.42	1.13	1.04	0.85	0.00	0.00	12.20	1.96	1.88	0.41	0.20	0.17	−0.42	0.00	0.00	1.59	0.26	0.24	NS	AP
M83	18	204.266172	−29.825121	0.85	0.00	0.00	3.42	1.04	0.95	0.57	0.00	0.00	11.90	1.88	1.70	0.28	0.15	0.14	−0.65	0.00	0.00	1.55	0.24	0.22	NS	ZA
M83	19	204.267739	−29.900895	2.86	0.97	0.87	0.94	0.00	0.00	2.16	0.95	0.86	11.11	1.90	1.78	−0.23	0.19	0.20	−0.01	0.27	0.27	1.45	0.25	0.23	⋯	⋯
M83	20	204.231018	−29.919042	0.69	0.00	0.00	2.00	0.87	0.79	0.89	0.00	0.00	9.11	1.67	1.56	0.29	0.19	0.18	−0.22	0.00	0.00	1.19	0.22	0.20	⋯	⋯
M83	21	204.260241	−29.888722	1.86	0.00	0.00	1.60	0.00	0.00	2.66	0.92	0.82	7.28	3.19	2.36	0.32	0.00	0.00	0.04	0.00	0.00	0.95	0.42	0.31	NS	AP
NGC 253	1	11.887405	−25.296824	183.31	3.90	3.77	134.68	5.76	5.73	9.33	1.70	2.16	397.00	8.50	8.64	−0.15	0.02	0.02	−0.87	0.02	0.03	30.16	0.65	0.66	BH	ULX
NGC 253	2	11.887485	−25.288801	87.88	36.78	37.24	161.89	19.58	34.17	14.76	0.00	0.00	285.48	51.43	60.23	0.32	0.38	0.20	−0.75	0.00	0.00	21.69	3.91	4.58	BH	ULX
NGC 253	3	11.889146	−25.289359	12.51	0.00	0.00	82.16	12.76	12.24	5.62	0.00	0.00	134.19	22.51	24.49	0.53	0.44	0.19	−0.65	0.00	0.00	10.19	1.71	1.86	NS	AP
NGC 253	4	11.928089	−25.250713	28.88	1.74	1.64	19.95	1.55	1.47	0.76	0.00	0.00	64.61	2.91	2.85	−0.18	0.04	0.04	−0.82	0.06	0.06	4.91	0.22	0.22	BH	I
NGC 253	5	11.896703	−25.253366	29.58	1.10	1.07	14.26	0.93	0.89	1.62	0.60	0.56	55.68	1.83	1.77	−0.33	0.03	0.03	−0.76	0.06	0.06	4.23	0.14	0.13	BH	S
NGC 253	6	11.844211	−25.347459	20.71	0.97	0.94	20.87	1.08	1.03	2.52	0.82	0.75	55.46	1.91	1.83	0.00	0.03	0.03	−0.75	0.05	0.06	4.21	0.15	0.14	NS	ZA
NGC 253	7	11.878991	−25.307364	8.88	1.96	1.88	13.60	2.06	1.97	0.91	0.00	0.00	30.98	3.55	3.45	0.18	0.13	0.12	−0.68	0.10	0.11	2.35	0.27	0.26	NS	ZA
NGC 253	8	11.827027	−25.320633	10.14	0.80	0.75	9.59	0.87	0.83	0.72	0.00	0.00	25.86	1.55	1.48	−0.04	0.05	0.05	−0.79	0.00	0.00	1.96	0.12	0.11	NS	ZA
NGC 253	9	11.883434	−25.289374	7.95	0.00	0.00	5.38	0.00	0.00	6.88	2.15	2.36	13.26	0.00	0.00	0.65	0.00	0.00	−0.33	0.75	0.22	1.01	0.00	0.00	⋯	⋯
NGC 253	10	11.892656	−25.284370	7.57	2.87	2.87	8.24	2.88	2.82	3.35	1.33	1.26	22.32	5.12	5.17	0.03	0.33	0.28	−0.40	0.29	0.22	1.70	0.39	0.39	BH	H
NGC 253	11	11.864731	−25.283095	3.81	0.92	0.87	9.81	1.11	1.07	6.87	0.83	0.79	18.74	1.77	1.71	0.70	0.00	0.00	−0.12	0.08	0.08	1.42	0.13	0.13	NS	AP

Table 3
(Continued)

Galaxy	ID	R.A.	Decl.	*NuSTAR* Count Rates												*NuSTAR* colors						*NuSTAR* L_X			Type	State
		(J2000.0)		(4 − 6 keV)	σ_{up}	σ_{down}	(6 − 12 keV)	σ_{up}	σ_{down}	(12–25 keV)	σ_{up}	σ_{down}	(4–25 keV)	σ_{up}	σ_{down}	HR1	σ_{up}	σ_{down}	HR2	σ_{up}	σ_{down}	(4–25 keV)	σ_{up}	σ_{down}		
				(10^{-4} counts s^{-1})																		(10^{38} erg s^{-1})				
NGC 253	12	11.878787	−25.295633	2.44	0.00	0.00	9.89	2.78	2.75	1.19	0.00	0.00	18.09	4.58	4.43	0.39	0.42	0.27	−0.49	0.00	0.00	1.37	0.35	0.34	NS	AP
NGC 253	13	11.919357	−25.236955	5.68	0.78	0.72	6.21	0.83	0.80	0.65	0.00	0.00	17.00	1.49	1.44	0.03	0.09	0.08	−0.54	0.00	0.00	1.29	0.11	0.11	⋯	⋯
NGC 253	14	11.854943	−25.329247	6.34	0.75	0.72	6.58	0.82	0.77	0.66	0.00	0.00	16.94	1.48	1.43	0.03	0.08	0.08	−0.59	0.00	0.00	1.29	0.11	0.11	⋯	⋯
NGC 253	15	11.866615	−25.305688	5.61	0.98	0.92	7.11	1.04	1.00	0.69	0.00	0.00	15.82	1.78	1.73	0.21	0.12	0.11	−0.54	0.00	0.00	1.20	0.14	0.13	⋯	⋯
NGC 253	16	11.878149	−25.312474	4.43	1.47	1.44	4.73	1.53	1.52	0.90	0.00	0.00	12.86	2.65	2.60	−0.07	0.21	0.22	−0.51	0.00	0.00	0.98	0.20	0.20	⋯	⋯
NGC 253	17	11.901412	−25.277326	5.29	1.13	1.07	5.72	1.15	1.10	0.62	0.00	0.00	12.82	2.01	1.91	0.07	0.16	0.15	−0.74	0.00	0.00	0.97	0.15	0.15	NS	ZA
NGC 253	18	11.929490	−25.256850	4.57	1.22	1.18	6.19	1.19	1.15	0.51	0.00	0.00	12.23	2.04	1.95	0.17	0.19	0.16	−0.84	0.00	0.00	0.93	0.15	0.15	NS	ZA
NGC 253	19	11.936255	−25.249076	3.19	1.10	1.07	4.64	1.10	1.06	0.80	0.00	0.00	10.88	2.02	1.95	0.13	0.24	0.20	−0.39	0.21	0.22	0.83	0.15	0.15	BH	H
NGC 253	20	11.878623	−25.247475	0.94	0.00	0.00	3.46	0.99	0.94	1.68	0.65	0.59	8.11	1.74	1.68	0.35	0.38	0.27	−0.26	0.22	0.23	0.62	0.13	0.13	⋯	⋯
NGC 253	21	11.881610	−25.251775	3.14	1.09	1.02	4.26	1.06	1.01	0.63	0.00	0.00	8.11	1.85	1.69	0.21	0.27	0.21	−0.73	0.00	0.00	0.62	0.14	0.13	NS	ZA
NGC 253	22	11.868956	−25.323236	3.59	0.78	0.74	2.80	0.81	0.76	0.59	0.00	0.00	7.87	1.49	1.35	−0.08	0.17	0.18	−0.52	0.00	0.00	0.60	0.11	0.10	⋯	⋯
NGC 253	23	11.904814	−25.333960	0.39	0.00	0.00	2.08	0.62	0.57	1.78	0.66	0.60	4.96	1.06	1.08	0.71	0.00	0.00	−0.02	0.20	0.21	0.38	0.08	0.08	NS	AP
NGC 253	24	11.855788	−25.278774	0.71	0.00	0.00	0.79	0.00	0.00	0.65	0.00	0.00	4.57	1.42	1.32	0.07	0.36	0.33	−0.14	0.00	0.00	0.35	0.11	0.10	⋯	⋯
NGC 253	25	11.837290	−25.296446	1.87	0.58	0.54	1.81	0.66	0.60	0.40	0.00	0.00	4.29	1.15	0.95	0.03	0.24	0.26	−0.54	0.00	0.00	0.33	0.09	0.07	⋯	⋯
M82	1	148.959041	69.679695	1558.52	8.00	7.95	2201.69	11.12	10.79	475.27	3.98	4.30	4894.26	15.82	17.09	0.17	0.00	0.00	−0.65	0.00	0.00	365.54	1.18	1.28	BH	ULX
M82	2	148.947688	69.683262	298.98	7.28	7.26	394.00	8.55	8.42	74.54	3.26	3.37	888.56	13.42	13.15	0.15	0.02	0.02	−0.68	0.01	0.01	66.36	1.00	0.98	BH	ULX
M82	3	148.972467	69.683930	160.41	5.58	8.85	192.71	8.58	12.24	37.29	2.34	2.73	473.13	9.05	9.12	0.10	0.02	0.02	−0.68	0.02	0.02	35.34	0.68	0.68	BH	ULX
M82	4	148.943809	69.678010	45.53	5.05	5.02	7.86	0.00	0.00	1.95	0.00	0.00	65.37	11.10	10.06	−0.45	0.00	0.00	−0.48	0.00	0.00	4.88	0.83	0.75	BH	S
M82	5	148.948396	69.688254	4.00	0.00	0.00	24.39	4.38	4.44	11.65	2.03	1.95	46.33	7.28	6.76	0.54	0.36	0.20	−0.35	0.13	0.10	3.46	0.54	0.50	NS	AP
M82	6	148.936554	69.679625	6.40	0.00	0.00	23.20	6.21	6.32	1.87	0.00	0.00	21.36	6.98	6.80	0.68	0.00	0.00	−0.84	0.00	0.00	1.60	0.52	0.51	NS	AP
M82	7	148.908934	69.674927	4.49	1.34	1.30	9.87	1.68	1.75	0.73	0.00	0.00	11.62	1.79	1.74	0.92	0.00	0.00	−0.65	0.00	0.00	0.87	0.13	0.13	NS	AP
M82	8	148.863555	69.656646	4.77	0.54	0.52	5.00	0.57	0.55	0.39	0.00	0.00	5.90	0.91	0.89	0.65	0.24	0.16	−0.66	0.00	0.00	0.44	0.07	0.07	NS	AP
M82	9	149.128916	69.705975	1.38	0.45	0.42	3.08	0.55	0.52	1.62	0.56	0.52	5.18	0.95	0.93	0.43	0.00	0.00	−0.38	0.18	0.23	0.39	0.07	0.07	NS	AP
M82	10	149.082374	69.696161	2.08	0.47	0.45	2.79	0.53	0.51	0.44	0.00	0.00	2.54	0.66	0.54	0.88	0.00	0.00	−0.75	0.00	0.00	0.19	0.05	0.04	NS	AP
M82	11	149.103354	69.715913	0.43	0.00	0.00	1.74	0.50	0.48	0.51	0.00	0.00	2.15	0.83	0.68	0.66	0.00	0.00	−0.14	0.00	0.00	0.16	0.06	0.05	NS	AP
M82	12	148.920935	69.657896	0.74	0.00	0.00	4.48	0.85	0.83	0.47	0.00	0.00	2.11	0.95	0.98	0.95	0.00	0.00	0.03	0.00	0.00	0.16	0.07	0.07	NS	AP

Note. Point source properties for galaxies from Table 1. Sources are grouped by galaxy and sorted/numbered by decreasing 4–25 keV count rate. Count rates shown are the soft (S, 4–6 keV), medium (M, 6–12 keV), hard (H, 12–25 keV), and full (F, 4–25 keV) energy bands. These count rates were derived from individual PSF fittings of each energy band (Section 4.3.2). Where the σ_{up} and σ_{down} values are 0.00 the *NuSTAR* count rate represents the upper limit on the 90% confidence interval. Section 4.3.3 defines the derivation of hardness ratios $HR1 = (M - S)/(M + S)$ and $HR2 = (H - M)/(H + M)$. Luminosities were calculated using the N_H values and distances from Table 1, assuming an absorbed power law with spectral index $\Gamma = 1.7$. The hardness ratios and luminosities were determined using the results of simultaneous PSF fitting described in Section 4.3.3, and thus can vary from values derived using count rates from individual PSF fittings in each energy band. State abbreviations are as follows: AP (accreting pulsar), S (BH soft state), I (BH intermediate state), H (BH hard state), ZA (Z/Atoll NS), and ULX (ultraluminous source). Compact object type and accretion state classifications are described in Section 5.1.

does not change source classifications and is smaller than the uncertainties on the hardness ratios. In Table 3 we presented the count rates from individual PSF fitting in each energy band (*S*, *M*, *H*, and *F*) but we used *HR*1, *HR*2, and *F* from simultaneous PSF fitting for our X-ray source diagnostics (Section 5.1) due to the improved constraints on uncertainties.

5. Results and Discussion

In this section we classify BHs and NSs using *NuSTAR* hardness-intensity and color–color diagrams. With this information we study the characteristics of compact object types/accretion states and trends with the sSFR. We investigate the correlation of XRB luminosity with the SFR and stellar mass. Lastly, we study the XLF of the *NuSTAR* sample and determine the ratio of BH to NS using BH-only and NS-only XLFs.

5.1. NuSTAR *XRB Diagnostic Diagrams*

It has long been understood that there are significant observable changes in the X-ray spectra of accreting BH and NS systems, which give an indication of changes in the underlying accretion state (e.g., the extent of the accretion disk that dominates in the softer X-rays versus non-thermal/coronal components that are more X-ray hard; see review by Done et al. 2007). These changes may, in large part, be directly linked to accretion physics phenomena and have advanced our understanding of the overall geometry of accreting compact objects. These states form the basis of the diagnostic diagrams we use in our work with *NuSTAR*, so we begin with a short review of current understanding of such spectral state changes.

Uhuru observations of Cygnus X-1 by Tananbaum et al. (1972) revealed a state change where the 2–6 keV X-ray intensity decreased by a factor of 4 and the 10–20 keV X-ray intensity doubled. Along with the simultaneous brightening of the radio counterpart, this result indicated that spectral changes signified important changes in the accretion physics of BH XRBs. Following 14 years of extensive monitoring with *RXTE*, there are now thousands of high signal-to-noise spectra and fairly well-understood phenomena for outbursts and state transitions for BH/NS as a population (e.g Maccarone & Coppi 2003; McClintock & Remillard 2006; Done et al. 2007; Church et al. 2014; Tetarenko et al. 2016). BHs in the hard state produce hard thermal Comptonized spectra that can be described by a power law with a photon index $\Gamma \sim 1.7$, with a cutoff at $\sim$100 keV. The BH soft state has a spectrum that is dominated by a disk blackbody component that peaks at $\sim$1 keV and a weak power-law tail extending to 500 keV with a photon index $\Gamma \sim 2$. The BH intermediate state is a transitional stage between the hard and soft states (e.g., McClintock & Remillard 2006), exhibiting a soft spectrum as the thermal disk component appears with an increased mass accretion rate. In addition, the hard power-law component steepens to $\Gamma \sim 2$–2.5. Almost all Galactic BH XRBs were found to follow the same hysteresis pattern in a hardness-intensity diagram (Maccarone & Coppi 2003; Done et al. 2007, see below for a more detailed discussion). The only sources that do not fit this pattern are Cygnus X-1 and X-3 (Smith et al. 2002), where Cygnus X-1 happens to be the only bright BH HMXB in the Galaxy (Cygnus X-3 is a BH candidate HMXB). Given that our sample is comprised of late-type galaxies, many with ongoing star formation, the majority of sources we detect will be bright HMXBs. Therefore, we must exercise caution when interpreting BH accretion states in our sample. The drastic spectral changes that occur in BHs allow them to be uniquely identified by their accretion state using hardness-intensity and color–color diagnostics (e.g., Remillard & McClintock 2006; Done et al. 2007).

NSs occupy a much narrower band in hardness-intensity and color–color diagrams when compared with BHs. Due to the small dynamic range of NS colors and the uncertainties associated with extragalactic sources, we are unable to robustly separate NS accretion states. Instead, we group all Z/Atoll sources (non-magnetized NSs) together, which are distinct from the harder spectra of young, magnetized accreting pulsars. The spectra of accreting pulsars are usually best described by a hard power law with photon index $\Gamma \sim 1$ and a cutoff at $\sim$20 keV (e.g., White et al. 1983). Z-track sources are named based on the Z pattern they trace out in a hardness-intensity diagram, through the horizontal, normal and flaring branches (Hasinger & van der Klis 1989; Schulz et al. 1989). Atoll sources are less luminous ($<10^{38}$ erg s^{-1}) and display island and banana (lower and upper) states. The spectra of Z/Atoll NSs vary, with a non-thermal Comptonized component dominating their emission. The high-energy cutoff of the Comptonized emission is $\approx$6 keV for sources $>10^{37}$ erg s^{-1}. There is also a thermal disk component that peaks between 1–2 keV, which for Atoll sources is weak in the island state and can be very strong in the banana state, but for bright Z sources it can rise to 50% of the total luminosity (Church et al. 2014). This rich phenomenology enables us to classify X-ray point sources as BHs or NSs based on luminosities and colors.

A. Zezas (2018, private communication) has completed detailed spectral fitting of $\sim$2500 Galactic *RXTE* PCA observations of 6 extensively studied BHs and 9 pulsars, where the compact object and orbital properties are extremely well constrained. The spectral libraries for BHs (Sobolewska et al. 2009) and pulsars (e.g., Reig 2011) were used to characterize each source class/state. The best-fitting results were converted from the *RXTE* to the *NuSTAR* energy bands. We selected the soft (*S*, 4−6 keV), medium (*M*, 6−12 keV), hard, (*H*, 12–25 keV), and full (*F*, 4–25 keV) *NuSTAR* energy bands because they provided the most robust separation between sources. Following work from Wik et al. (2014b) and Yukita et al. (2016), we created *NuSTAR* diagnostic diagrams to determine global properties of the point source population, specifically the distribution of compact object types and accretion states.

In Figure 4(a) we show the hardness-intensity (left) and color–color (right) diagrams. Due to the overlap between different accretion states and source types in both diagnostic diagrams, there remain some ambiguities in these diagnostics for some sources, even when the statistics are excellent. For the 4–25 keV count rates, sources near the detection limit naturally have larger uncertainties compared to the brightest sources.

In Figures 4(b)–(i) we show the hardness-intensity and color–color plots for each galaxy in our sample. We grouped galaxies in Figures 4(g) and (h) with a similar sSFR. Uncertainties shown represent the 90% confidence interval and delineated regions on the color–color diagram are approximations to isolate different accretion states and source types. Numbers label point sources by decreasing 4–25 keV count rate.

Due to the many observations with varying cadence that have been co-added for each galaxy, the count rates and

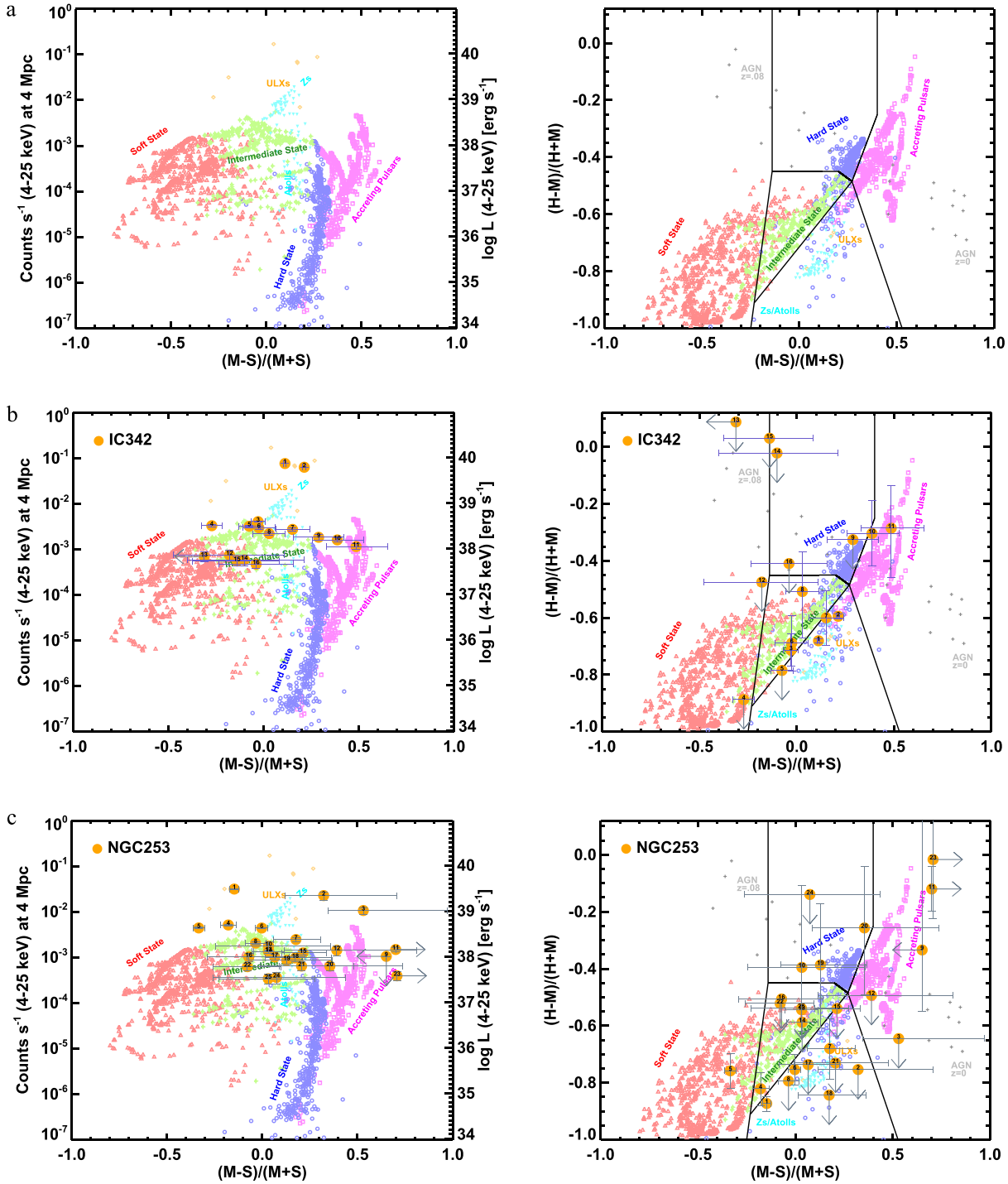

Figure 4. (a) *NuSTAR* hardness-intensity (left) and color–color (right) diagrams for Galactic XRBs. The data points indicate different accretion states and compact object types: accreting pulsars (magenta squares), hard state BH XRBs (blue circles), intermediate state BH XRBs (green stars), and soft state BH XRBs (red triangles). These data points were based on spectral fits to thousands of *RXTE* PCA observations of Galactic XRBs in well-defined accretion states and with known compact object types. Z/Atoll NSs are shown as inverted cyan triangles and are based on spectral fits to *RXTE* and *BeppoSAX* observations of Galactic LMXBs (Church et al. 2014). ULXs (orange diamonds) were derived from spectral fits from various studies: Bachetti et al. (2013, NGC 1313 X-1 and X-2), Walton et al. (2013, Circinus ULX5), Walton et al. (2014, Holmberg IX X-1), Rana et al. (2015, IC 342 X-1 and X-2). Soft (S), medium (M), and hard (H) correspond to the 4–6 keV, 6–12 keV, and 12–25 keV energy bands. Delineated regions on the color–color diagram are approximations to isolate different accretion states. We also included implied colors of AGNs (gray filled plusses) from the *NuSTAR* extragalactic survey (see Section 5.1.1). The count rate axis was converted to a luminosity axis assuming $\Gamma = 1.7$ and $N_{\rm H} = 10^{20}$ cm^{-2} and normalizing to a distance of 4 Mpc. (b) Hardness-intensity (left) and color–color (right) diagrams for IC 342. Uncertainties shown represent the 90% confidence interval. Numbers label point sources by decreasing count rate (see Table 3). (c) As in Figure 4(b) for NGC 253. (d) As in Figure 4(b) for M83. (e) As in Figure 4(b) for NGC 1313. (f) As in Figure 4(b) for M81. (g) As in Figure 4(b) for dwarf galaxies Holmberg II, Holmberg IX, and NGC 5204, all with a similar sSFR. (h) As in Figure 4(b) for Circinus and NGC 4945. (i) As in Figure 4(b) for M82. (j) As in Figure 4(b) for all sources from all galaxies. The left panel shows that most point sources overlap with the BH-XRB intermediate state, which is also degenerate with hard state BHs and Z/Atoll NSs. The characteristics of the soft state are such that our sensitivity limits prevent us from detecting many sources in this region (see Section 5.1.2). The right panel shows more distinct separation between accretion states and compact object types, specifically the sources constrained in the Z/Atoll NS region. In particular, there are fewer sources located in the intermediate state due to the constraints from 12–25 keV. The color–color diagnostic was used for source classification because it was more robust at breaking degeneracies between source types. Sources in the right panel with large hard colors above the hard state are possibly background AGNs that can be identified with optical followup.

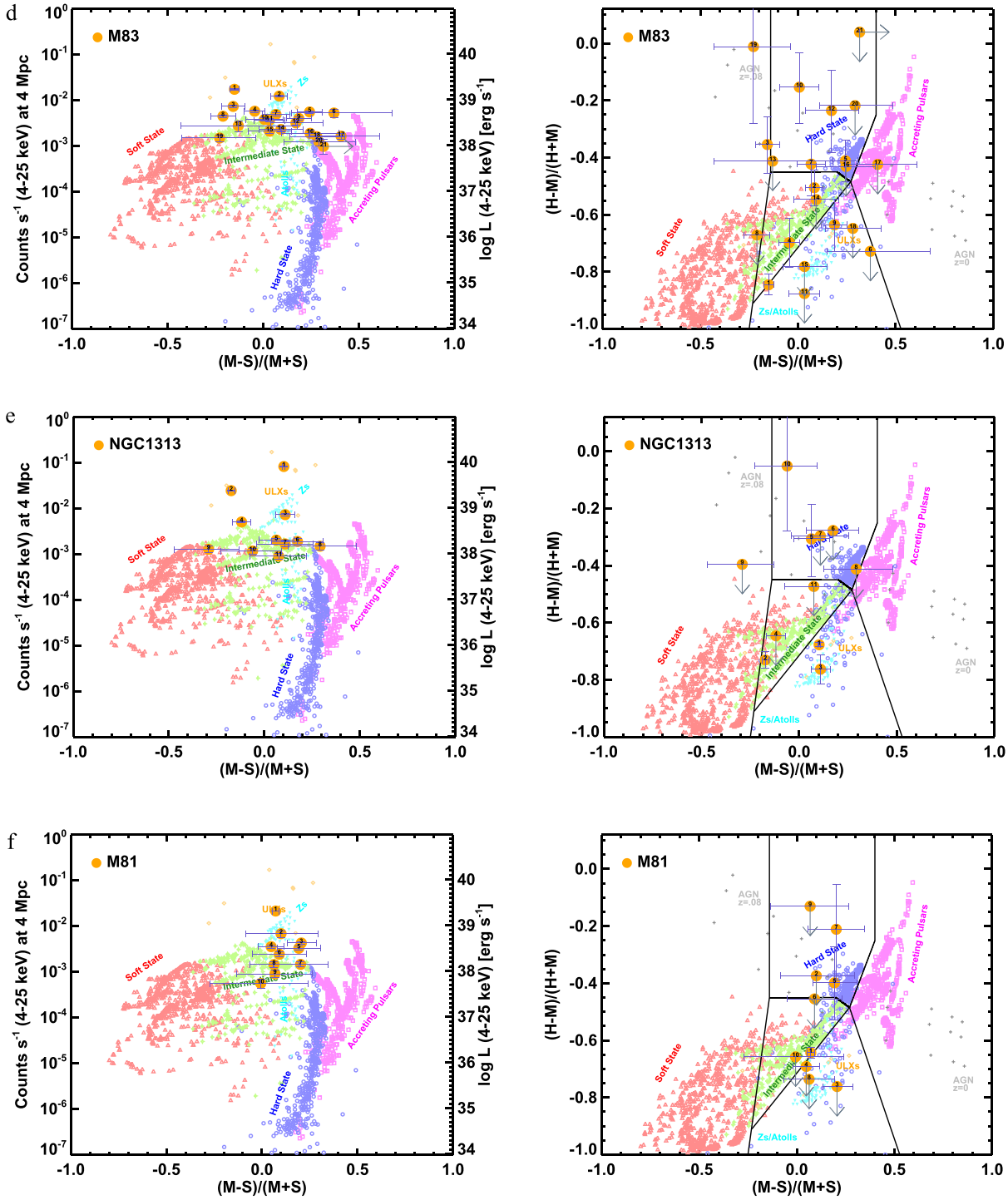

Figure 4. (Continued.)

hardness ratios represent averages, potentially hiding any variability. Wik et al. (2014b) was able to study the multi-epoch properties of the brightest eight sources in NGC 253 and found only one underwent a state transition, while two sources varied slightly in flux. Yukita et al. (2016) found no statistically significant variability among M83 sources over three epochs. However, while most extragalactic sources studied may be persistent, galaxies such as M82 with longer exposure times and high cadence require more detailed investigation. In Figure 4(j) we show all point sources from all galaxies in the sample. The left panel shows that most point sources overlap with the BH-XRB intermediate state, which is degenerate with the Z/Atoll source loci. However, the color–color plot allows for clearer separations between source types and shows that some of these sources are likely NS accretors.

Combining X-ray luminosity with *HR*1 and *HR*2 allows us to constrain X-ray source characteristics via identification of the accretor and accretion state. The color–color plots show more robust separation, particularly the Z/Atoll NS sources that are localized below the BH points with softer *HR*1 colors.

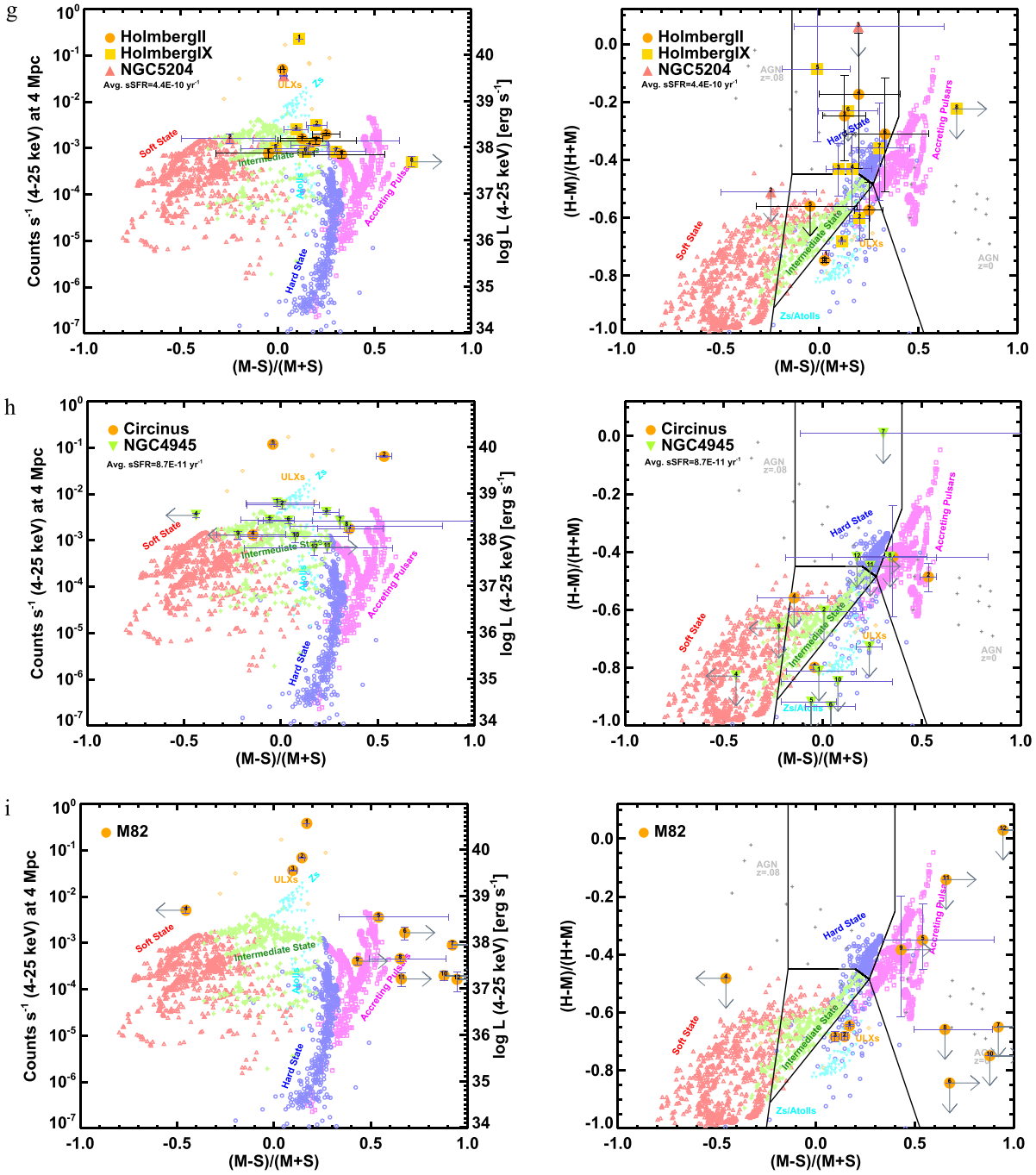

Figure 4. (Continued.)

This is due to the spectra of non-magnetized NSs (and also ULXs), which turn over more quickly than BHs (e.g., Maccarone et al. 2016). There are ∼10 *NuSTAR* sources that overlap the isolated Z/Atoll sources (not identified as ULXs based on L_X) and are undetected in *HR*2; however, the upper limits constrain them to the NS region. The scatter about the intermediate state is evident, especially for sources near and above the hard state, which are possibly background galaxies. Given the loci and uncertainties in the diagnostic diagrams, we were able to classify 90 compact objects and 87 accretion states from our sample of 128 sources. These are candidate classifications that require further detailed study (e.g., multi-wavelength spectra) to confirm their nature. When source classification between the diagnostic diagrams disagreed, we utilized the color–color result due to its improved source separation. The identifications for each source are shown in Table 3, while the total number of sources in each category is shown in Table 4.

5.1.1. AGN Contamination

To estimate AGN colors we used the results from the *NuSTAR* extragalactic survey of Del Moro et al. (2017), who calculated the average broadband (3–24 keV observed frame) X-ray spectral properties of 182 AGNs. They found an average power-law photon index of $\Gamma = 1.65$, flatter than the typical $\Gamma \approx 1.8$ for AGNs (e.g., Tozzi et al. 2006). The spectral slope

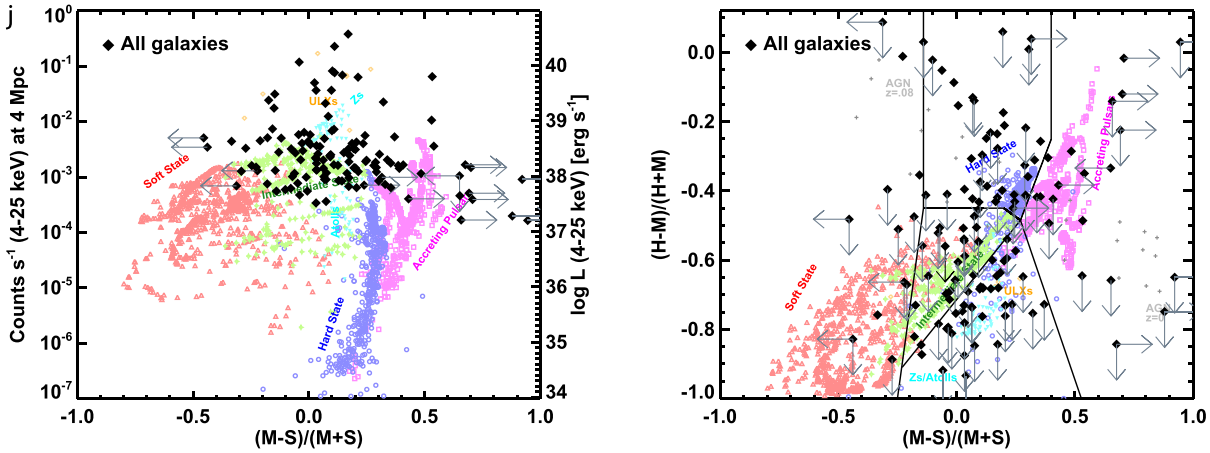

Figure 4. (Continued.)

Table 4
Compact Object Classification and Accretion States

	Total	Hard State	Intermediate State	Soft State	ULX	Z/Atoll	Accreting Pulsar
BHs	47	16	8	6	15	…	…
NSs	43	…	…	…	…	21	21

Note. 90 of the 128 sources in our sample were separated into the BH/NS classification. From these 90 classifications, 2 BHs and 1 NS could not be classified to a particular accretion state. We assumed that all ULXs were BHs (see Section 5.2).

Table 5
Background AGN Contamination

Galaxy	Holmberg II	IC 342	M82	NGC 253	M81	NGC 4945	Holmberg IX	Circinus	NGC 1313	M83	NGC 5204
Background AGNs	1	2.8	1.6	1.5	2	1	1.3	1.2	1.9	2.3	0.7

Note. The number of background AGNs expected in each observed field is based on the *NuSTAR* AGN number counts from Harrison et al. (2016). These estimates closely match the number of unclassified sources that overlap the AGN region in the color–color diagrams for each galaxy.

of broad-line and X-ray unabsorbed AGNs was consistent with typical values ($\Gamma = 1.79$), but narrow-line and heavily absorbed sources had values as low as $\Gamma = 1.38$. We used the best-fitting spectral parameters for composite spectra that were grouped into all AGNs, narrow-line AGNs, and broad-line AGNs, varying the redshift from $z = 0.00$–0.08. We show the implied colors of the AGNs in the right panels of Figure 4. AGNs are found in a variety of locations, but most are concentrated in regions with large *HR*1 or *HR*2 colors. In particular, M82 has four sources located in the bottom right corner of its color–color diagram, which may be absorbed NS sources as opposed to AGNs, due to the large values of extinction in M82.

We also used the *NuSTAR* AGN number counts from Harrison et al. (2016) to determine the number of background galaxies expected for each galaxy in the sample, based on the *NuSTAR* FOV and the sensitivity limits for detected sources. In Table 5 we show the expected number of background AGNs for each galaxy. These estimates closely match the number of unclassified sources that overlap the AGN region in the color–color diagrams for each galaxy. Optical followup is required for all *NuSTAR*-detected sources to determine which are background AGNs.

5.1.2. Connections with the sSFR

In Figure 5 we plot the distribution of identified candidate BHs and NSs as a function of the sSFR of each galaxy. We also plot the BH fraction, defined as $N_{\rm BH}/(N_{\rm BH}+N_{\rm NS})$. As shown in Figure 2, the galaxy sample is not uniform across the sSFR and therefore features of the histogram may be biased based on the sSFR distribution. At a large sSFR a higher fraction of BHs is evident, which likely represent BH HMXBs that have formed from recent star formation episodes. Conversely, NSs begin to dominate galaxies toward a lower sSFR, as BH HMXBs become less numerous and older (LMXB) populations are more prevalent. M31, which is not shown here, is dominated by NSs at $\log({\rm sSFR/yr^{-1}}) = -11.5$. A Spearman's rank test on the fraction of BH versus the sSFR gave a p-value of 0.072 and coefficient $r_s = 0.56$. While the coefficient indicates weak monotonicity, the p-value is too large to claim a correlation. However, when including M31, which is dominated by NSs and extends the sSFR to lower values, we obtain a p-value of 0.028 and a coefficient $r_s = 0.63$. However, there are a number of caveats we must consider. First, most galaxies in the sample have 4–25 keV sensitivities of $\sim 10^{38}$ erg s^{-1}, which is not a sufficient limit from which to draw conclusions between the BH fraction and the sSFR. In addition, M31 *NuSTAR*

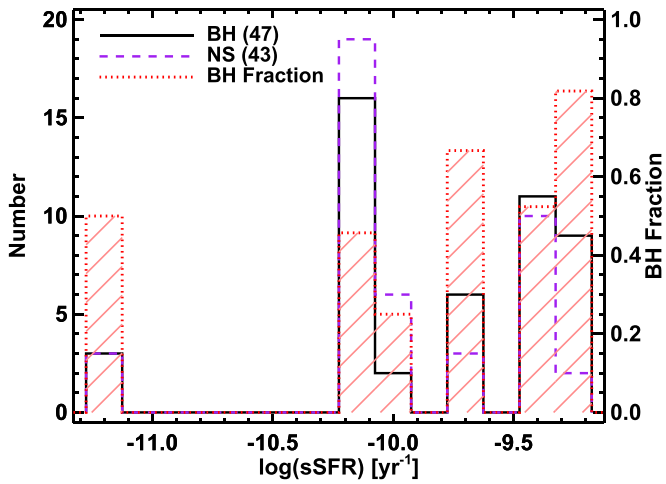

Figure 5. Histograms showing the distribution of BHs and NSs for a given sSFR based on the *NuSTAR* galaxy sample. The red dotted line (red line filled histogram) shows the BH fraction. As shown in Figure 2, the sample is not uniform across the sSFR and therefore features of the histogram are biased based on the sSFR distribution. There is no statistically significant relation between the BH fraction and the sSFR (see Section 5.1.2).

observations extend down to 10^{36} erg s^{-1}, 1−2 orders of magnitude fainter than the rest of the sample. Even among the remaining galaxies, completeness is not uniform (see Figure 1). These issues are exacerbated due to *NuSTAR's* PSF, which can mask sources under the broad wings of, e.g., ULXs, thus biasing sensitivity. Therefore, an expanded sample with improved statistics and completeness for X-ray point sources in each galaxy is necessary to draw conclusions between the sSFR and the ratio of BH/NS.

Do we expect to find a different ratio of BH/NS based on galaxy type? The preliminary indication that BH fraction may be larger for a high sSFR and decline toward a low sSFR, while not statistically significant, has interesting implications. First, these results are strictly limited to the XRBs we can detect, and therefore the population of BHs and NSs that are preferentially faint will be missed. Therefore, it is difficult to address the issue of compact object formation rates. This type of study is more applicable to the issue of mass accretion rate and conversion of accretion into luminosity. BH HMXBs generally accrete mass via the wind of the donor star at a rate proportional to $M_{\rm acc}^2$, where $M_{\rm acc}$ is the mass of the accreting compact object (Hoyle & Lyttleton 1939; Bondi & Hoyle 1944). For BH LMXBs, we can use the analytical approximations of mass transfer rate from King et al. (1996), which gives three cases that describe the physical processes driving the mass accretion rate:

1. evolution based on the nuclear evolution of the donor star, which is independent of accretor mass $M_{\rm acc}$
2. magnetic braking, which scales with $M_{\rm acc}^{-2/3}$
3. gravitational radiation, which scales with $M_{\rm acc}^{2/3}$

We expect high luminosities in the third case only for very short period sources, and in the second case for transient outbursts or a donor of mass $\approx 1 M_\odot$. Most BHs are transient sources (e.g., Wiktorowicz et al. 2014; Belloni & Motta 2016; Corral-Santana et al. 2016), and there is only one strong candidate persistent BH LMXB in the Milky Way, 4U 1957 + 115 (e.g., Ricci et al. 1995; Nowak et al. 2008; Gomez et al. 2015). Some sources could be long duration outburst transients, such as GRS 1915 + 105, which may be difficult to distinguish from persistent sources without extremely long light curves. Thus, the most luminous (persistent) LMXBs are more likely to be NSs. We would then expect to detect a lower BH fraction in galaxies with a low sSFR dominated by LMXBs. However, this effect would not necessarily extend down the luminosity function, where numerous transient BH LMXBs reside.

In Figure 6 we show the distribution of BH accretion states (left) and accreting NS sources (right) as a function of the sSFR of each galaxy. Two BHs and one NS source could not be separated by accretion state. All sources with $L_{\rm X}$ (4–25 keV) $\gtrsim 1.3 \times 10^{39}$ erg s^{-1}, the Eddington limit for a 10 $M_\odot$ BH, are classified as ULXs. Eight of 15 ULXs are found at a high sSFR as expected due to elevated star formation. Hard state BHs compose a large proportion of sources at all sSFRs, indicating a common XRB accretion state independent of the sSFR. With optical followup it may become apparent that a fraction of hard state sources are background AGNs, which would explain their prevalence at all values of sSFRs. Intermediate state sources are found at intermediate sSFRs. The accreting pulsar population is prevalent in the starburst galaxy M82 at log (sSFR/yr^{-1}) = −9.4, whereas the fraction of Z/Atoll NSs increases toward a lower sSFR as expected. M31, which is not shown here, is dominated by Z/Atoll sources.

Hard state BHs appear as a large fraction of all identified accretion states at all sSFRs in the left panel of Figure 6. However, we do not expect there to be a relation between BH accretion states and the sSFR. Instead, the accretion state depends on parameters such as orbital separation and disk instabilities. Tetarenko et al. (2016) recently produced an updated catalog of Galactic BH XRBs that provides a convenient comparison for our extragalactic sample. The study found that $38^{+6.0}_{-5.6}$% of 132 transient outbursts detected in the Galaxy in the last 19 years do not complete the hysteresis pattern, skipping the transition from the hard to soft state. Either long periods were spent in the hard state or the source would reach the intermediate state then transition back to the hard state. They found that this hard state-only behavior was not limited to recurrent transients but also seen in long-term transient and persistent accreting BH (Tetarenko et al. 2016, and references therein). The duration of Galactic BH outbursts vary depending on whether they were successful (i.e., state transition occurred) or hard state-only, having mean values of ≈247 and ≈391 days, respectively (Tetarenko et al. 2016). These hard state outburst sources generally have peak luminosities $\lesssim 0.11\ L_{\rm Edd}$, near the transition region to soft state luminosities. The hard state-only phenomenon is thought to occur in sources with low-level mass accretion rates. These factors may also explain the lack of identified soft state sources. While we need increased sensitivity to detect soft state sources, *NuSTAR* observations of M31 reaching $\sim 10^{36}$ erg s^{-1} have shown that most sources are NSs compared with only 2–3 potential BH hard state candidates. Of these BH candidates, none were soft state sources.[13] For the Galactic BH hard state sources in the *NuSTAR* hardness-intensity diagrams (blue circles), most are found at $L_{\rm X} < 3 \times 10^{37}$ erg s^{-1}, although they do extend just above 10^{38} erg s^{-1}. However, the *NuSTAR*

[13] Maccarone et al. (2016) demonstrated the likely NS nature of 5 M31 GCs, contrary to the previous BH candidate classification for 2 of these sources. They argued that BH candidates that are persistent and luminous are more likely NS (e.g., 50 M31 BH candidates in Barnard et al. 2014b).

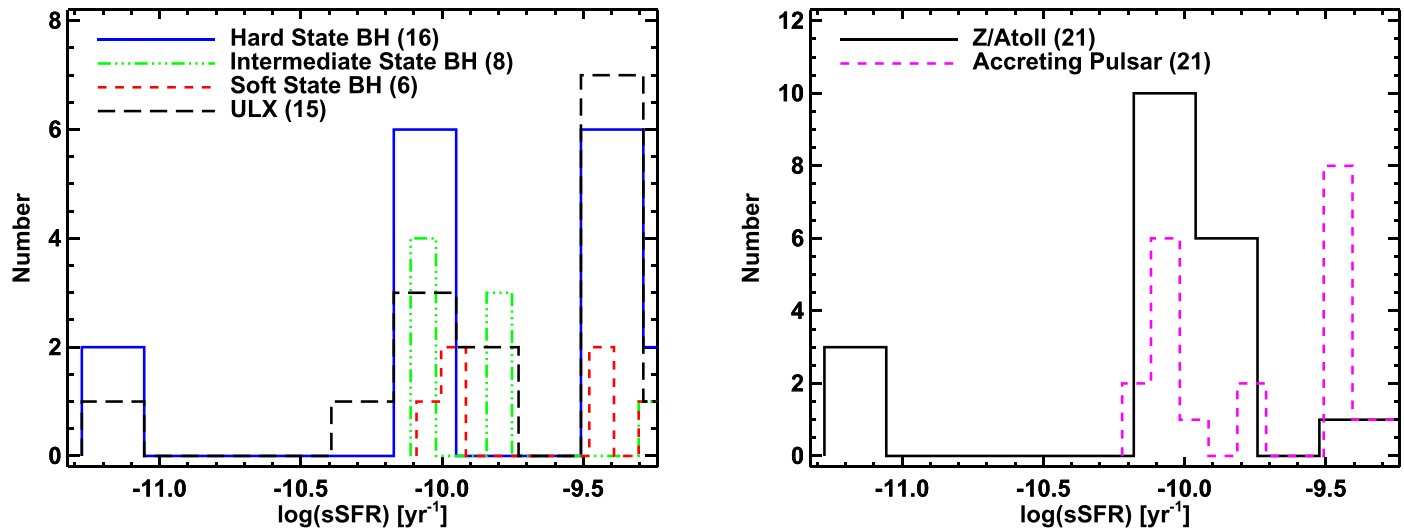

Figure 6. Histograms showing the distribution of various BH accretion states (left) and accreting NS sources (right) for a given sSFR based on the *NuSTAR* galaxy sample. Bin sizes vary based on the number of sources at each sSFR. Two BHs and one NS source could not be separated by their accretion state. As shown in Figure 2, the sample is not uniform across sSFRs and therefore features of the histogram are biased based on the sSFR distribution. ULXs are prevalent at high sSFR as expected due to elevated star formation, and accreting pulsars are prevalent in the starburst galaxy M82 at $\log(\mathrm{sSFR/yr^{-1}}) = -9.4$.

sample sources classified as hard state BH have $L_X \gtrsim 10^{38}\,\mathrm{erg\,s^{-1}}$, similar to the persistent Galactic BH HMXB Cygnus X-1,[14] which spends most of its time in the hard state (Grinberg et al. 2013).

The accreting pulsars used to create the diagnostic diagrams in Figure 4 are Galactic NSs with strong magnetic fields, accreting from high-mass companions. We detected accreting pulsar candidates in M82 (8), NGC 253 (5), Circinus (2), IC 342 (2), and one in each of M83, NGC 1313, NGC 4945, and Holmberg IX. These types of sources are produced by recent bursts of star formation, thus it is no surprise that M82 and NGC 253, galaxies with the largest SFR in our sample, contain a large number of pulsars. X-ray pulsars have also been found in the Large (e.g., Antoniou & Zezas 2016) and Small (e.g., Antoniou et al. 2010; Haberl & Sturm 2016) Magellanic Clouds. Both the SMC (Harris & Zaritsky 2004) and LMC (Harris & Zaritsky 2009) have an SFR of $\approx 0.3\,M_\odot\,\mathrm{yr^{-1}}$ and an sSFR similar to that of M82. To date, various studies have identified 64 pulsars in the SMC (Haberl & Sturm 2016; Vasilopoulos et al. 2017) and 19 in the LMC (Clark et al. 2015; Antoniou & Zezas 2016; Haberl et al. 2017; Vasilopoulos et al. 2018), with sensitivity limits $\sim 10^{33}\,\mathrm{erg\,s^{-1}}$ in the 0.5–10 keV energy band. All but two of the 21 pulsars identified in this work have L_X (4–25 keV) $\leqslant 3 \times 10^{38}\,\mathrm{erg\,s^{-1}}$, with a peak at the Eddington limit for NSs. Conversely, the populations in the Magellanic Clouds have L_X (0.2–12 keV) $\leqslant 10^{38}\,\mathrm{erg\,s^{-1}}$, with the majority of sources at least an order of magnitude fainter (Yang et al. 2017). This hampers comparison to the Magellanic Clouds because the detection limit of our survey mainly probes accreting pulsars undergoing very luminous type II outbursts, which are very rare (Reig 2011).

Due to the dependence of the pulsar rate (number formed per SFR) on the time since the star formation episode, and varying sensitivity limits, it is difficult to directly compare results. Pulsars in the SMC were found in regions having a peak in star formation history at $\approx$42 Myr and duration of 33 Myr (Antoniou et al. 2010). However, using spatially resolved maps of star formation history in the LMC, Antoniou & Zezas (2016) found the region around pulsars peaked earlier at $\approx$13 Myr with duration 32 Myr. There is an indication that the dominant stellar population in M82's nucleus is $\sim$10 Myr old, and reaches 100 Myr at 500 pc (Rodríguez-Merino et al. 2011). The star-forming complex in the central region of NGC 253 is thought to be <8 Myr old and have been formed in the last $\sim$30 Myr (Engelbracht et al. 1998; Davidge 2016). These estimates are broadly in agreement with timescales from the Magellanic Clouds.

Many galaxies in our sample have rich muti-wavelength data sets that allow these sources to be investigated using UV/optical/IR catalogs, which, in combination with the *NuSTAR*-*Chandra*/*XMM-Newton* data we analyzed, can help confirm the nature of these sources (e.g., to determine if they are located in globular clusters). These cross-correlations will help to confirm the accuracy of *NuSTAR* diagnostics. We do not perform this analysis here as it is beyond the scope of this paper (see Lazzarini et al. 2018 for detailed optical counterpart identification).

5.2. Correlation of X-Ray Luminosity with SFR and Stellar Mass

The connection between X-ray luminosity and the SFR and stellar mass of a galaxy has been well studied. *Chandra*, in combination with multiwavelength data, has constrained the correlation between HMXBs and SFR as well as LMXBs and stellar mass (e.g., Grimm et al. 2003; Ranalli et al. 2003; Colbert et al. 2004; Gilfanov 2004a; Gilfanov et al. 2004a; Persic & Rephaeli 2007; Lehmer et al. 2010; Mineo et al. 2012; Lehmer et al. 2016). Despite variations in other galaxy properties such as stellar age, metallicity, dynamics, etc., these global relations are remarkably consistent. The well-known relation between galaxy X-ray luminosity and the SFR can be parametrized as follows:

$$\log L_X = \log A + B \log \mathrm{SFR}, \tag{5}$$

where L_X is in units of $\mathrm{erg\,s^{-1}}$ and the SFR is in units of $M_\odot\,\mathrm{yr^{-1}}$. The X-ray luminosity of galaxies at energies $\gtrsim$2 keV

[14] Not part of the *RXTE* sample Galactic BH sources used to create the *NuSTAR* diagnostic diagrams.

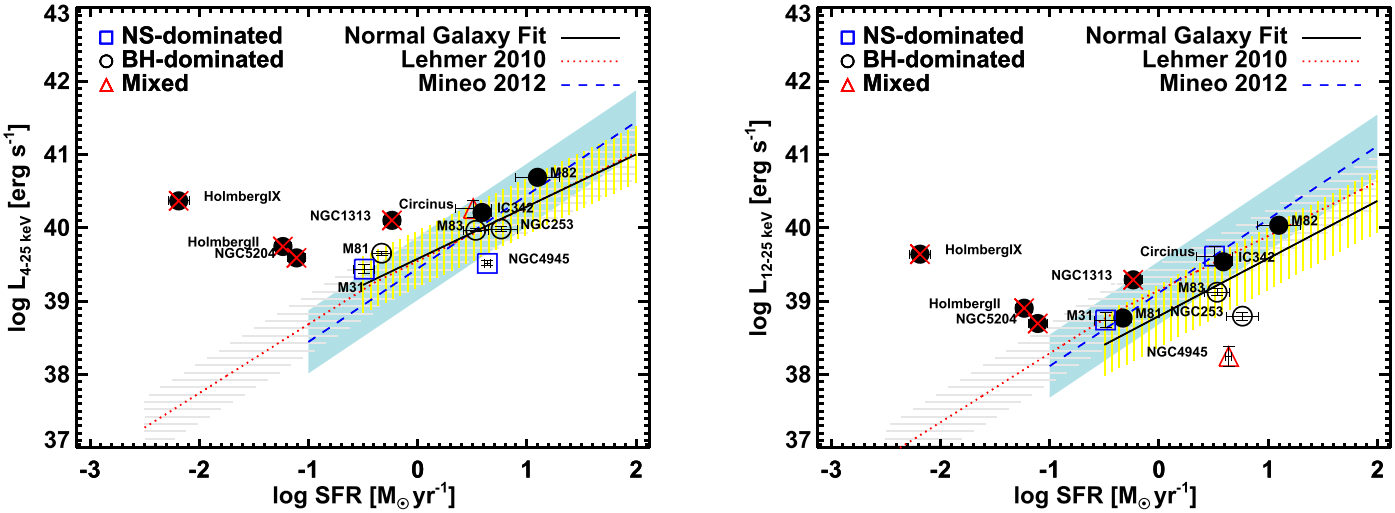

Figure 7. The integrated 4–25 keV (left) and 12–25 keV (right) point source emission (based on the sources in Table 3) as a function of the SFR of that galaxy is shown for the *NuSTAR* sample. The same spectral model for conversion from count rate to L_X was assumed as shown in Figures 4(a)–(j). Galaxies were classified as NS- (blue squares), BH- (black circles), and ULX-dominated (filled) if >70% of their 4–25 keV (left) or 12–25 keV (right) point source emission came from one of these groups (see Table 6). Galaxies that were not BH- or NS-dominated were classified as mixed (red triangles). The dashed blue line shows the L_X–SFR relation for 29 nearby star-forming galaxies from Mineo et al. (2012), with the dispersion shaded light blue. The dotted red line represents the L_X–SFR relation for 66 normal galaxies from Lehmer et al. (2010), with horizontal gray lines showing the dispersion. We converted these relations to the 4–25 and 12–25 keV bandpasses using the same spectral model as in Figures 4(a)–(j). The solid black line shows the best fit for the eight normal (Milky Way-type) galaxies in the sample (see Section 5.2 and Table 8, red crosses indicate dwarfs excluded from the fit), with yellow vertical lines showing the dispersion. The 4–25 keV fit matches the result from Lehmer et al. (2010), whereas the 12–25 keV fit is offset based on the assumed spectral model.

is dominated by XRBs. While nonlinear scalings exist for the individual L_X (LMXB) and L_X (HMXB) relations based on low stellar mass and low-SFR regimes, respectively (e.g., Gilfanov et al. 2004b), we also adopt the combined form to constrain the total XRB emission from a galaxy:

$$L_X(\mathrm{XRB}) = L_X(\mathrm{LMXB}) + L_X(\mathrm{HMXB}) = \alpha M_\star + \beta \mathrm{SFR}, \tag{6}$$

$$L_X(\mathrm{XRB})/\mathrm{SFR} = \alpha(\mathrm{SFR}/M_\star)^{-1} + \beta. \tag{7}$$

Previous surveys have investigated X-ray emission in the 0.5–2, 2−10, and 0.5–8 keV energy bands. X-ray emission from normal galaxies in the 2–10 keV band is dominated by XRBs and therefore is a cleaner correlation. We utilized the broad 4–25 keV and the hard 12–25 keV energy bands to study the L_X relation with the SFR and stellar mass. The broad band is an ideal comparison to previous 2–10 keV studies because of the similar flux in each band for XRB spectra with $\Gamma \sim 1.7$ and average values of extinction. The hard band provides a clean sample of XRB-only emission and insight into how hard X-ray luminosity from XRBs varies with the SFR and stellar mass.

The *NuSTAR* sample includes 12 galaxies, with three of these being dwarf galaxies (Holmberg II, Holmberg IX, NGC 5204). A fourth, NGC 1313, is intermediate between dwarf and $L^\star$ galaxies.[15] The sample is slightly biased toward an intermediate sSFR (Figure 2) as a result of the relative lack of nearby starbursts and massive elliptical galaxies. The absence of elliptical galaxies from our sample means that the correlations will be dominated by the star-forming component that produces bright HMXBs. The exceptions to this rule are M31 and M81, where a low SFR and thus lack of bright HMXBs results in LMXBs (globular cluster sources in the case of M31) dominating the integrated emission.

[15] An $L^\star$ galaxy has a luminosity similar to the Milky Way.

While we expect L_X to scale with both the stellar mass and the SFR, the sample galaxies are mostly intermediate sSFRs (not LMXB-dominated), so we also investigated the L_X–SFR correlation (e.g., Lehmer et al. 2010; Mineo et al. 2012). In Figure 7 we show the integrated 4–25 keV (left) and 12–25 keV (right) point source emission (based on sources in Table 3) as a function of the SFR for each galaxy in the *NuSTAR* sample.

We grouped galaxies in the sample using results from the *NuSTAR* diagnostic diagrams (Figures 4(a)–(j)). Specifically, for all the sources in a galaxy that were classified as BHs or NSs, we determined what percentage of the 4–25 and 12–25 keV luminosity came from each population. Galaxies with $\gtrsim$70% of their L_X from BHs (NSs) were classified as BH-dominated (NS-dominated) and shown as black circles (blue squares). Galaxies that did not meet either of these criteria were classified as mixed and are shown as red triangles. Galaxies that had $\gtrsim$70% of their L_X from ULXs (defined as sources with L_X (4–25 keV) $\gtrsim 1.3 \times 10^{39}$ erg s^{-1}, the Eddington limit for a 10 $M_\odot$ BH) were classified as ULX-dominated (filled symbols).

In Table 6 we show the proportion of 4–25 and 12–25 keV luminosity from each of these populations. While most ULXs have historically been presumed to be BHs, recent work using *NuSTAR*/*XMM-Newton* has shown that some sources exhibit pulsations and are in fact NSs (Bachetti et al. 2014b; Fürst et al. 2016; Israel et al. 2017a, 2017b). Only the confirmed ULX pulsar M82 X-2 is in the *NuSTAR* galaxy sample we analyzed,[16] but we cannot rule out the possibility that other ULX sources may be proven to be NSs as opposed to BHs. A binary population synthesis study by Fragos et al. (2015) found that only 13% of galaxies that have a similar star formation history to M82 are likely to have ULXs with an NS accretor. Therefore, we assumed that galaxies dominated by ULXs have BH accretors.

[16] We were not able to separate emissions from ULXs M82 X-1 and M82 X-2, which are 5″ apart.

Table 6
Galaxy Classifications Based on Source Type

Galaxy	NS Percent	BH Percent	ULX Percent	BH+NS	NS Percent	BH Percent	ULX Percent	BH+NS
	(4–25 keV)				(12–25 keV)			
Circinus	36 (2)	64 (2)	64 (1)	4	75 (2)	25 (1)	25 (1)	3
IC 342	3 (3)	97 (6)	89 (2)	9	4 (3)	96 (4)	94 (2)	7
NGC 4945	80 (6)	20 (2)	0 (0)	8	0 (0)	0 (0)	0 (0)	0
Holmberg II	0 (0)	100 (3)	94 (1)	3	0 (0)	100 (2)	91 (1)	2
M81	26 (3)	74 (3)	60 (1)	6	0 (0)	100 (3)	79 (1)	3
Holmberg IX	2 (2)	98 (5)	96 (1)	7	1 (1)	99 (1)	99 (1)	2
NGC 5204	0 (0)	100 (2)	96 (1)	2	0 (0)	100 (1)	100 (1)	1
NGC 1313	7 (2)	93 (6)	85 (2)	8	5 (1)	95 (3)	94 (2)	4
M83	25 (7)	75 (8)	23 (1)	15	26 (2)	74 (6)	10 (1)	8
NGC 253	28 (10)	72 (6)	59 (2)	16	26 (3)	74 (3)	27 (1)	6
M82	2 (8)	98 (4)	97 (3)	12	2 (2)	98 (3)	98 (3)	5
Total	43	47	15	90	14	27	15	41

Note. Percentage of 4–25 and 12–25 keV luminosity from BHs, NSs, and ULXs based on the total luminosity for all classified sources. The number of sources in a category is shown in parentheses, and the total number of sources in each category is shown in the last row. The total number of BHs and NSs in each galaxy is shown in the BH+NS column. These values were used to categorize galaxies in Figures 7 and 8, where galaxies were classified as NS-, BH-, and ULX-dominated if >70% of their point source emission came from one of these groups.

Table 7
Best-fitting L_X–SFR Parameters

Energy Band (keV)	A	B
4–25	39.49 ± 0.15	0.83 ± 0.24
12–25	38.80 ± 0.21	0.79 ± 0.32

Note. Best-fitting parameters and 1σ uncertainties for $\log L_X = \log A + B\log\mathrm{SFR}$ (Equation (5)) for the eight normal (Milky Way-type) galaxies in the *NuSTAR* sample from Figure 7.

We fit the log-linear model from Equation (5) to the data in Figure 7. We performed fitting using the generalized linear model (*glm*) in ***R*** (R Development Core Team 2008). The solid black line shows the best fit for the eight normal[17] (Milky Way-type) galaxies in the sample. We only used the eight normal ($L^\star$) galaxies in the sample, excluding Holmberg II, Holmberg IX, NGC 5204, and NGC 1313. Fitting the relation using different morphological types biases the underlying physical assumption of late-type galaxies having X-ray point source emission dominated by HMXBs. The best-fitting parameters are shown in Table 7. For comparison we show the L_X–SFR relation for 29 nearby star-forming galaxies from Mineo et al. (2012) (dashed blue line), converted from 0.5–8.0 keV. We also show the relation for 66 normal galaxies from Lehmer et al. (2010) (dotted red line), converted from 2–10 keV. We used the same spectral model as in Figures 4(a)–(j) to convert to the 4–25 and 12–25 keV ranges. The fit from Lehmer et al. (2010) is separated into distinct curves above and below an SFR of 0.4 $M_\odot\,\mathrm{yr}^{-1}$. Our 4–25 keV best fit matches the result from Lehmer et al. (2010), whereas the 12–25 keV fit, while still consistent, is offset based on the assumed spectral model used to convert the Lehmer et al. (2010) relation to 12–25 keV. Contrary to these nonlinear L_X–SFR fits, Mineo et al. (2012) found a linear correlation that agrees within uncertainties due to the large scatter in the relations. They argued the dispersion was not a result of measurement uncertainties or the CXB/LMXB sources but instead of physical origin.

In order to constrain the total XRB emission from each galaxy we fit the data using Equation (7). In Figure 8 we show the integrated 4–25 keV (left) and 12–25 keV (right) point source emission (based on sources in Table 3) normalized by the SFR as a function of the sSFR for each galaxy in the *NuSTAR* sample. Classifications are the same as in Figure 7. To properly analyze XRB emission and its relation with the sSFR required us to make corrections to the stellar masses of certain galaxies. We adjusted the stellar masses of M31 and M81 based on the FOV and AGN-dominated emission region, respectively. For M31, we used the updated stellar mass maps from Williams et al. (2017), which were derived from fits to data from the Panchromatic Hubble Andromeda Treasury Survey, scaled to the FOV of the *NuSTAR* observations. We did not include the M81 AGN in our source list/analysis and as such excluded the stellar mass in a circular region of radius 1′.5 centered on the AGN where no other sources could be detected. Using Table 3 of Tenjes et al. (1998) we calculated the mass within this region to be $2.4 \times 10^{10} M_\odot$ (25% of the total) and excluded that value from the total stellar mass of M81. Both NGC 4945 and Circinus have Seyfert nuclei that were also excluded from our source list. However, their low luminosity did not prevent us from detecting sources in their bulges within 0′.5 of their nuclei, therefore, we do not exclude any stellar mass from the total as it is negligible.

As in Figure 7, we used the eight normal ($L^\star$) galaxies in the sample to determine the best fit to Equation (7). The dashed blue line in Figure 8 shows the (*glm*) best fit, while the parameters are presented in Table 8. The 4–25 keV L_X/SFR for the NS model does not differ appreciably from the Lehmer et al. (2010) local-galaxy relation. The ULX model of NGC 1313 X-1 does show elevated L_X/SFR relative to Lehmer et al. (2010) as expected. For the 12–25 keV panel the NS model has a relatively lower L_X/SFR than the NGC 1313 X-1 ULX model, indicating that NS spectra turn over faster than ULXs. The increased scatter in the 12–25 keV panel compared to the 4–25 keV is evident as in Figure 7, particularly for NGC 4945

[17] Galaxies with stellar masses $M_\star > 10^{10} M_\odot$.

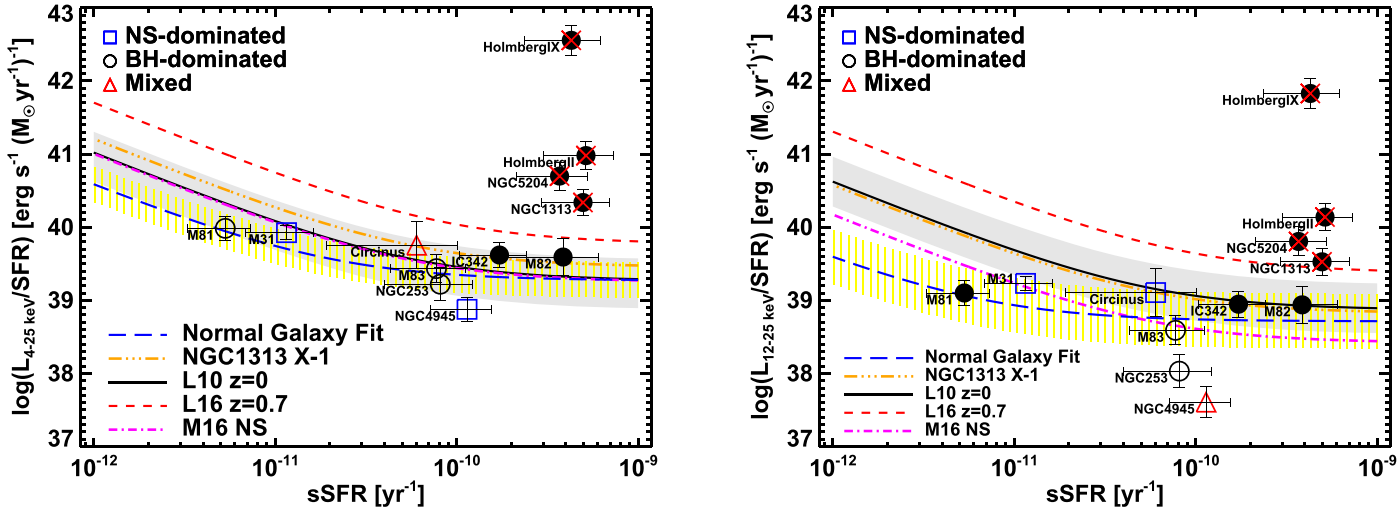

Figure 8. The integrated 4–25 keV (left) and 12–25 keV (right) point source emission (based on the sources in Table 3) normalized by the SFR as a function of the sSFR of that galaxy is shown for the *NuSTAR* sample. The same spectral model for conversion from count rate to L_X was assumed as in Figures 4(a)–(j). Galaxies were classified as NS- (blue squares), BH- (black circles), and ULX-dominated (filled) if >70% of their 4–25 keV (left) or 12–25 keV (right) point source emission was from one of these groups (see Table 6). Galaxies that were not BH- or NS-dominated were classified as mixed (red triangles). The solid black line represents the relation from the local ($z = 0$) galaxy sample of Lehmer et al. (2010), with the dispersion shaded light gray. The dashed red line shows the relation from the *Chandra* Deep Field South stacked galaxy sample of Lehmer et al. (2016), with a median redshift of 0.7. We converted the original 2–10 keV luminosities to our bandpasses using the spectral model assumed by Lehmer et al. (2016). We also converted the Lehmer et al. (2010) local galaxy result based on various spectral models: using the NGC 1313 X-1 ULX spectrum from Bachetti et al. (2013) (dashed–dotted orange line) and the COMPTT model for the NS in Bo 185 from Maccarone et al. (2016) (dashed–dotted magenta line). The dashed blue line shows the best fit for the eight normal (Milky Way-type) galaxies in the sample (see Section 5.2 and Table 8, red crosses indicate dwarfs excluded from the fit), with yellow vertical lines showing the dispersion. We have adjusted the stellar mass of M31 and M81 based on the FOV and AGN-dominated emission region, respectively.

Table 8
Best-fitting L_X/SFR-sSFR Parameters

Energy Band (keV)	α (10^{28} erg s^{-1} $M_\odot^{-1}$)	β (10^{39} erg s^{-1} ($M_\odot$ yr^{-1})$^{-1}$)
4–25	3.560 ± 1.163	1.902 ± 0.837
12–25	0.343 ± 0.221	0.515 ± 0.188

Note. Best-fitting parameters and 1σ uncertainties for the relation L_X (XRB) = $\alpha\, M_\star + \beta$ SFR (Equations (6) and (7)) for the eight normal (Milky Way-type) galaxies in the *NuSTAR* sample from Figure 8.

and NGC 253 in the 12–25 keV band. Both panels indicate that L_X per unit of SFR is larger for a lower sSFR.

Previous studies (e.g., Lehmer et al. 2010) found that extinction in the star-forming regions of starburst galaxies could account for the decreased L_X/SFR in the 2–10 keV band. With *NuSTAR*, the 4–25 keV and especially the 12–25 keV energy bands are not subject to the same degree of extinction. Even with extreme extinction of $N_H = 10^{24}$ cm^{-2}, the 4–25 and 12–25 keV energy bands are attenuated[18] by factors of 2 and 1.2, respectively, from standard galactic values of 10^{20} cm^{-2}, assuming a power law with $\Gamma = 1.7$. Thus, we find that L_X/SFR is indeed lower at low sSFR compared to previous studies. A larger sample of galaxies with a uniform sSFR is required in order to determine whether these correlations hold for a larger range in the sSFR.

The galaxies in the *NuSTAR* sample are spirals/dwarfs with recent star formation and are not LMXB-dominated elliptical galaxies. As such, their point source emission should be dominated by HMXBs. The four dwarf galaxies that are BH- and ULX-dominated all have elevated L_X/SFR for a given sSFR compared to the normal $L^\star$ galaxies. This effect may be a result of the star formation history of a galaxy that leads to a peak in L_X/SFR, similar to the peak in the B*e*-HMXB distribution ~50 Myr after a star formation episode found in nearby galaxies (e.g., Antoniou et al. 2010; Williams et al. 2013; Antoniou & Zezas 2016). However, M82 X-1 has also been detected at a 4–25 keV luminosity[19] of 5×10^{40} erg s^{-1}, which would shift it above the best-fitting relation into the dwarf galaxy locus. None of the galaxies in Lehmer et al. (2010) at similar sSFRs, which have even higher SFRs, have a total L_X above 10^{40} erg s^{-1}. The transient nature of XRBs, specifically the duration and recurrence times of their outbursts, can introduce complications in studying the relationship of L_X with the SFR and stellar mass.

5.3. Hard XLFs

XLFs of nearby galaxy point source populations are a powerful tool because they are not subject to the uncertainties associated with galactic sources (distance, extinction, low number statistics, etc.). Gilfanov (2004a) investigated a sample of 11 nearby galaxies with old stellar populations and determined that the total X-ray luminosity and the XLF of LMXBs each scaled with stellar mass. Similarly, Grimm et al. (2003) studied the X-ray populations of nearby spiral/starburst galaxies and found that the total X-ray luminosity and XLF of HMXBs scaled with the SFR (see Fabbiano 2006 for a review of XRB XLFs). The latter discovery is particularly appropriate for our work as our sample is dominated by late-type galaxies with HMXBs. Recent work by Mineo et al. (2012) using *Chandra*, *Spitzer*, *GALEX*, and 2MASS data of 29 nearby star-forming

[18] For photoelectric absorption; scattering further reduces the flux by ~50% in each energy band.

[19] Converted from 0.3–10 keV (Bachetti et al. 2014b).

galaxies confirmed and updated the 0.5–8 keV HMXB-SFR relation. They found an XLF power-law slope of 1.6 in the range $L_X = 10^{35\text{-}40}$ erg s^{-1} with evidence for a break above this limit. They did not find any features near the Eddington limit for a NS or BH. However, a larger study of 343 nearby galaxies (213 late-type) with *Chandra* by Wang et al. (2016) did detect a break dividing NS and BH XRBs in the composite XLF of early and late-type galaxies. For the 213 late-type galaxies the break was located at $(6.3 \pm 0.3) \times 10^{38}$ erg s^{-1} with a power-law slope of 1.6 ± 0.03 and 2 ± 0.05 below and above the break, respectively. The flat slope of the HMXB XLF up to 10^{40} erg s^{-1} suggests that ULXs are prevalent among high-SFR galaxies. The smooth transition past the Eddington limit for NSs may be due to a population of ULX pulsars (see Section 5.2). Recent analysis of *XMM-Newton* and *NuSTAR* data favors super-critically accreting NSs as the engines of a large fraction of ULXs; although degeneracy between spectral models warrants deeper broadband observations to support this interpretation (Koliopanos et al. 2017). If there is a break in the HMXB XLF of late-type galaxies, separating NS and BH XRBs to create independent XLFs would determine how sources are distributed and help interpret the origin of the break.

Do we expect the XLFs of XRBs to differ at harder energies? XLFs of the Milky Way and nearby galaxies are generally presented in the 0.5–10 keV energy range. The XLFs in the soft X-ray band (∼1–10 keV) do not accurately represent the total luminosity of spectrally hard and absorbed HMXBs. For LMXBs, the brightest systems emit most of their energy in the standard ∼1–10 keV band, whereas faint systems emit a similar amount of energy in the standard and 10–100 keV energy range (Revnivtsev et al. 2008). Only a few studies have investigated the hard ($E > 10$ keV) XLF, where most have focused on AGNs (e.g Sazonov et al. 2007; Paltani et al. 2008; Ajello et al. 2012; Bottacini et al. 2012; Mereminskiy et al. 2016).

The first hard XLF was presented by Krivonos et al. (2007) using 17–60 keV data from the *INTEGRAL*/IBIS all-sky survey, detecting 219 Galactic sources, including 90 LMXBs and 76 HMXBs. Revnivtsev et al. (2008) used this *INTEGRAL* catalog (Krivonos et al. 2007) to study the XLF of Galactic center/bulge LMXBs, separating persistent (22) and transient (16) sources. The LMXB XLF was probed to a limit of 7×10^{34} erg s^{-1} and exhibited a flattening at the faint end with a differential slope of 0.96 ± 0.2 and 1.13 ± 0.13 for persistent and persistent+transient sources, respectively. The authors argued that the drop-off in the hard XLF for $L_{17\text{–}60\,\mathrm{keV}} \gtrsim 10^{37}$ erg s^{-1} is a result of the spectral change near this luminosity in the 2–10 keV band, where sources have very soft spectra and therefore lower luminosities for energies $E > 10$ keV.

More recently, a detailed XLF for Galactic sources above 10 keV was compiled by Voss & Ajello (2010) using 15–55 keV data taken with *Swift*-BAT from 2005–2007. Specifically, they classified 211/228 (93%) of their sources, including 61 LMXBs and 43 HMXBs, for which they derived XLFs down to 7×10^{34} erg s^{-1}. They found a differential faint slope of 1 for LMXBs, consistent with results from the 2–10 keV band and Revnivtsev et al. (2008). The HMXB XLF had a differential slope of $1.3^{+0.3}_{-0.2}$, which was flatter but similar to the canonical value of ≈1.6 for the Milky Way and other galaxies from the soft X-ray. However, the break at 2×10^{37} erg s^{-1} was inconsistent with the single power-law slope from soft X-ray surveys. Doroshenko et al. (2014) completed a robust analysis of Galactic LMXB and HMXB XLFs using the *INTEGRAL* catalog of Krivonos et al. (2012). A novel method was used to create XLFs that did not require distance measurements for any of the sources. The differential HMXB XLF parameters were $\alpha_1 = 0.3^{+0.8}_{-0.2}$, $\alpha_2 = 2.1^{+3}_{-0.6}$, and $L_{\mathrm{break}} = 0.55^{+4.6}_{-0.28} \times 10^{36}$ erg s^{-1}. Both LMXBs and HMXBs had a flatter slope at low luminosities and a lower break luminosity compared to the previous hard X-ray studies.

The only known extragalactic hard XLF was published by Lutovinov et al. (2012). Using *INTEGRAL* data from 2003–2004 and 2010–2012 they produced the 20–60 keV completeness-corrected XLF of HMXBs in the LMC. From the six HMXBs in their sample, they found a power-law slope of $1.8^{+0.4}_{-0.3}$ and a break at $\sim 10^{37}$ erg s^{-1}. The power-law slope agreed with previous results in the 2–10 keV band from HMXBs in the LMC (Shtykovskiy & Gilfanov 2005) and predictions from the canonical HMXB XLF (Grimm et al. 2003).

Following their extragalactic study, Lutovinov et al. (2013) used the 9-year *INTEGRAL* All-Sky Survey catalog (Krivonos et al. 2012) to study 48 persistent Galactic HMXBs. Differential slopes for the HMXB XLF were $\alpha_1 = 1.40 \pm 0.13(\mathrm{stat}) \pm 0.06(\mathrm{syst.})$ and $\alpha_2 > 2.2$ with $L_{\mathrm{break}} = [2.5^{+2.7}_{-1.3}(\mathrm{stat.}) \pm 1.0(\mathrm{syst.})] \times 10^{36}$ erg s^{-1}. The statistical significance of the break was at the 2σ level, but the authors argued that the low-luminosity flattening of the wind-fed NS-HMXB XLF is likely real. The break luminosity was different from that of Grimm et al. (2002) and Voss & Ajello (2010), primarily due to the absence of BH systems, transients, Roche lobe systems, and varying completeness-correction methods. The lack of bright ($>10^{37}$ erg s^{-1}) HMXB sources in the Galaxy differs from the HMXB XLFs of star-forming galaxies, where the power-law slope continues to higher L_X.

To investigate the characteristics of the hard X-ray source population, we plot the 4–25 keV and 12–25 keV observed XLFs of detected sources in Figure 9. The number of sources between panels varies because many sources are undetected in the 12–25 keV band. The total XLF in both panels, which is comprised of only spiral/dwarf galaxies, has a slope that matches the HMXB XLF from the Milky Way and star-forming galaxies. However, the dwarf galaxies, whose sources are included in the total XLFs, were selected based on hosting ULXs, and so represent a biased sample that skews the bright end of the total XLFs.

Due to low number statistics for individual galaxies, which resulted from a combination of point source sensitivity and source confusion, the total XLF serves as a more robust sample suitable for comparison. The 12–25 keV XLF represents the intrinsic XRB luminosity for each galaxy as no extinction is expected and contribution from other source types is minimal. The shape is consistent with results from the soft 0.5–8 keV energy band. Even though the SFR ranges from ≈0.01–15 $M_\odot$ yr^{-1} there is limited scatter in the XLFs, where variations at low-L_X are a result of differing sensitivities. Mineo et al. (2013) found a monotonic increase in the ULX rate with SFR, and therefore the high-luminosity breaks in our XLFs constrain the ULX rate of the sample galaxies. In Figure 10 we show histograms of the luminosity distribution of detected sources in the 4–25 keV (left) and 12–25 (right) keV energy

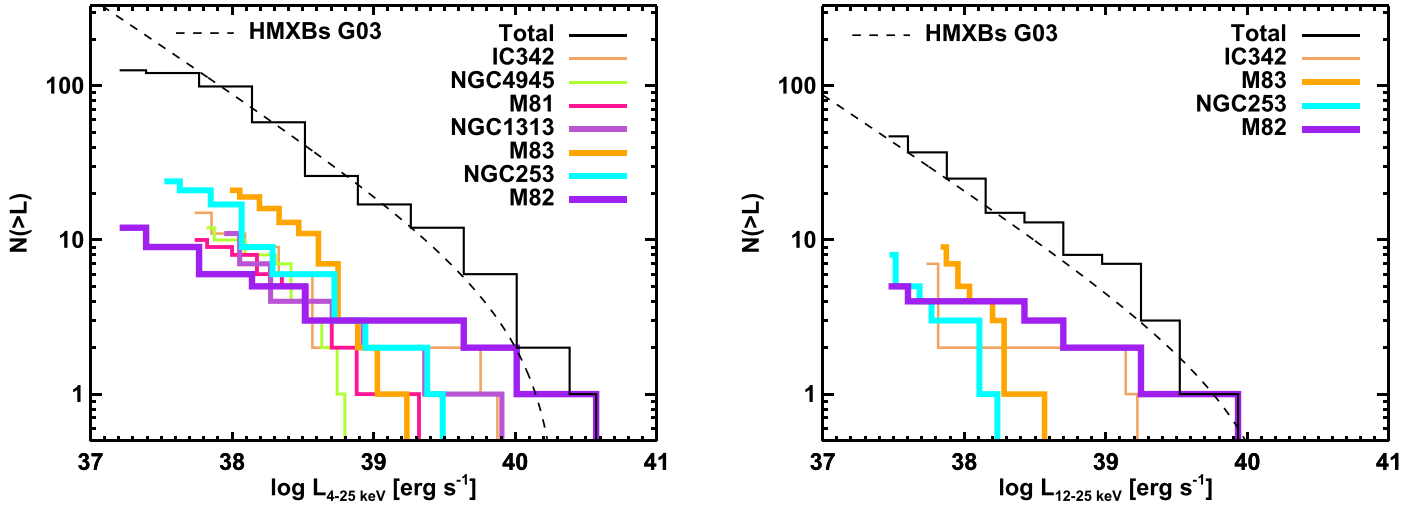

Figure 9. *NuSTAR* XLFs in the 4–25 keV (left) and 12–25 keV (right) energy bands for the detected sources. We only included individual XLFs for galaxies that had at least 10 (5) sources for 4–25 (12–25) keV. No completeness correction nor normalization for the SFR nor the stellar mass has been applied. The total XLFs (solid black line) represent all detected sources (in the given energy band) from all galaxies in the sample, including those whose individual XLFs are not shown here. The dashed black line shows the HMXB XLF from Grimm et al. (2003), normalized to 17 and 4 $M_\odot$ yr^{-1} for 4–25 and 12–25 keV, respectively. These normalizations were chosen such that the HMXB power-law relation was coincident with the total XLF in each panel. The total 4–25 and 12–25 keV XLFs, which are comprised of only spiral/dwarf galaxies, match well compared to the HMXB XLF from star-forming galaxies.

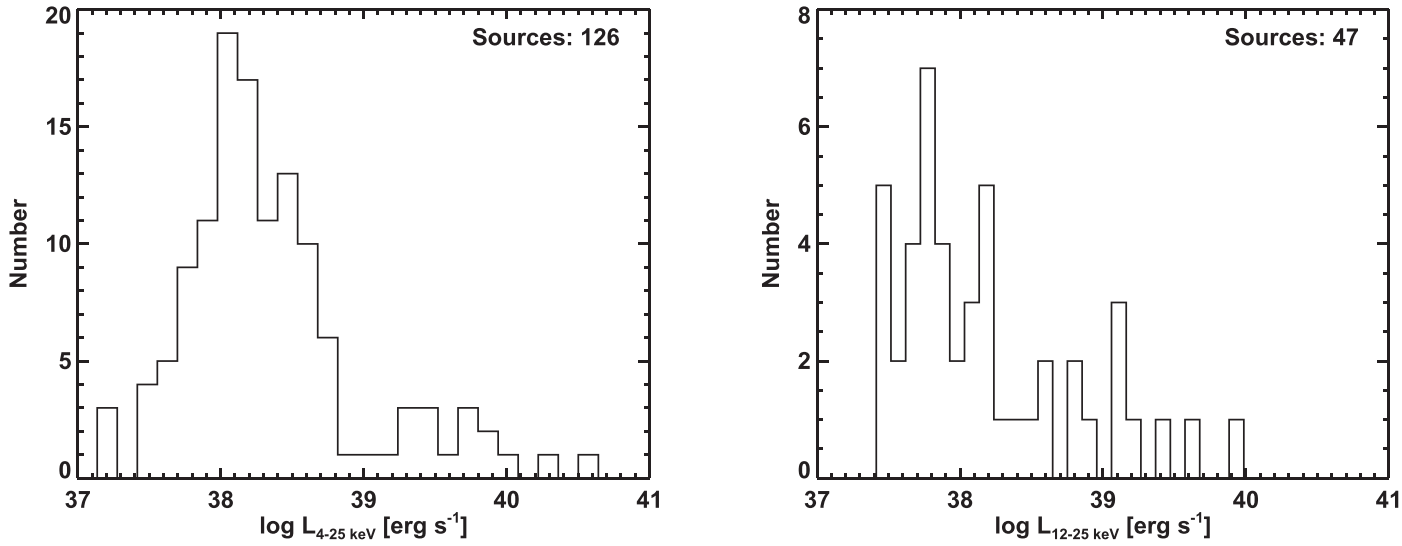

Figure 10. Histograms showing the luminosity distribution of detected sources in the 4–25 keV (left) and 12–25 keV (right) energy bands.

bands. The 4–25 keV completeness limit of our sample is apparent at $\approx 10^{38}$ erg s^{-1}.

5.3.1. BH and NS XLFs

As opposed to previous extragalactic XLF studies with *Chandra* and *XMM-Newton*, we were able to separate the population of XRBs into BHs and NSs. Identifying compact object types using, e.g., dynamical measurements or quasi-periodic oscillations, is unfeasible for galaxy populations. This simple yet powerful methodology enables us to explore hard X-ray characteristics in relation to BH/NS accretion regimes.

In Figure 11 we show the NS (dashed lines) and BH (solid lines) XLFs in the 4–25 keV (black) and 12–25 keV (blue) energy bands. XLFs represent all detected sources from the sample in the given energy band (including sources from galaxies whose individual XLFs were not shown in Figure 9). Conversions from the bolometric Eddington limits were calculated for BHs using the best fit DISKBB + CUTOFFPL spectrum from IC 342 X-1 (Rana et al. 2015) and for NSs using the best fit POWERLAW spectrum from M82 X-2 (Brightman et al. 2016). For the BH model, the 12–25 keV flux is 27% of the 4–25 keV flux, while for the NS model it is 55%. The 4–25 and 12–25 keV NS XLFs have similar shapes (as do the BH XLFs), which can be confirmed by applying the energy band conversion to the 4–25 keV XLFs. Both the 4–25 and 12–25 keV NS XLFs suggest a drop beginning at $\approx 10^{38}$ and $\approx 6 \times 10^{37}$ erg s^{-1}, respectively, attributable to their 1.4 $M_\odot$ NS Eddington limits. Increased sensitivity and completeness will be required to confirm these declines. The 4–25 keV BH XLF has a more gradual decline past the 4–25 keV Eddington limit for a 10 $M_\odot$ BH, with an abrupt drop at $\approx 7 \times 10^{39}$ erg s^{-1}, the bolometric Eddington limit for a 50 $M_\odot$ BH. Given the detection of $\sim$30 $M_\odot$ BH by the Laser Interferometer Gravitational Wave Observatory, it is possible that these sources are stellar-mass BHs accreting at the Eddington limit as opposed to super-Eddington

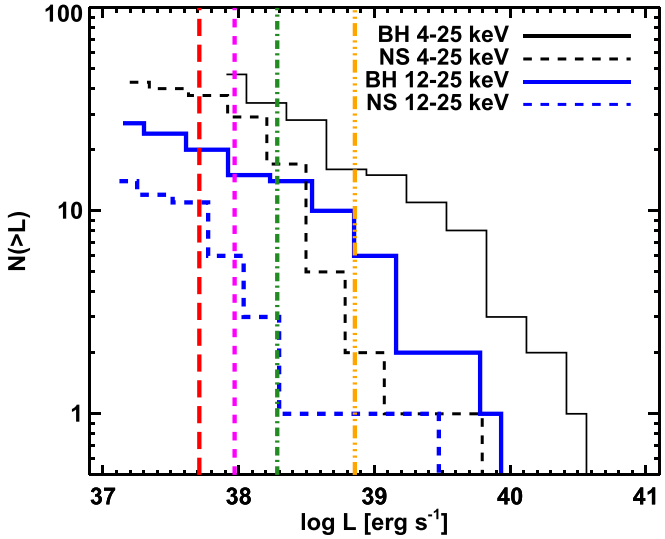

Figure 11. *NuSTAR* XLFs for candidate BH and NS sources from the sample in the 4–25 and 12–25 keV energy ranges. Vertical lines represent the Eddington limits for a 1.4 $M_\odot$ NS and a 10 $M_\odot$ BH as in Figure 12 (see Section 5.3.1 for details). The 12–25 keV NS XLF suggests a drop at $\approx 6 \times 10^{37}$ erg s^{-1}, attributable to the 12–25 keV Eddington limit for a 1.4 $M_\odot$ NS.

sources (Abbott et al. 2016, 2017a, 2017b; Marchant et al. 2017). The 12–25 keV NS and BH XLFs are essentially cutoff at their respective bolometric Eddington limits. How do we interpret the distribution of BHs across our luminosity range? Elbert et al. (2018) recently predicted the BH number as a function of galaxy stellar mass using an empirical approach based on the relationship between galaxy stellar mass and stellar metallicity. They estimated that an $L^\star$ galaxy should host millions of $\sim 30\,M_\odot$ BH, while dwarf satellite galaxies like Draco should host ~ 100. They determined that most low-mass BHs of $\sim 10\,M_\odot$ reside in massive galaxies ($M_\star \simeq 10^{11} M_\odot$) while massive BHs of $\sim 50\,M_\odot$ are typically found in dwarf galaxies ($M_\star \simeq 10^9\,M_\odot$). This result may explain the prevalence of many luminous ($\simeq 10^{40}$ erg s^{-1}) ULXs that have been found in dwarf galaxies such as Holmberg II/IX, which contribute to the bright end of the BH XLF.

One of the main goals of this work was to determine the ratio of BH to NS. In Figure 12 we used the cumulative XLFs to plot the ratio of BH to NS and the BH fraction[20] $N_{\rm BH}/(N_{\rm BH}+N_{\rm NS})$ in the 4–25 keV (top panel, black) and 12–25 keV (bottom panel, blue) energy bands. Vertical lines are as in Figure 11. By taking the ratio of the BH and NS cumulative XLFs we were able to determine the X-ray luminosities at which each source population is prevalent relative to the other. The 4–25 keV band has a ratio of ≈ 1 that begins to rise at the 4–25 keV NS Eddington limit, as one would expect the number of NSs to decrease. The same is true in the 12–25 keV energy band. It is apparent that the 4–25 keV ratio of BH/NS peaks past the 10 $M_\odot$ BH Eddington limit with a value of 15. However, the BH fraction rises past this point, indicating BHs dominate but may decrease in total number. Whether this is a statistical fluctuation due to the small sample size or a real peak in total BH number, coincidence with the 10 $M_\odot$ BH Eddington limit is intriguing in relation to the BH mass distribution. While the BH/NS ratio declines past this point, despite the existence of only one NS source $>10^{39}$ erg s^{-1}, a larger sample is needed to determine if stellar mass BHs in late-type galaxies are not copious in this mass–luminosity regime. A confirmation of the utility for the

[20] The BH fraction is not cumulative, unlike the cumulative BH/NS ratio.

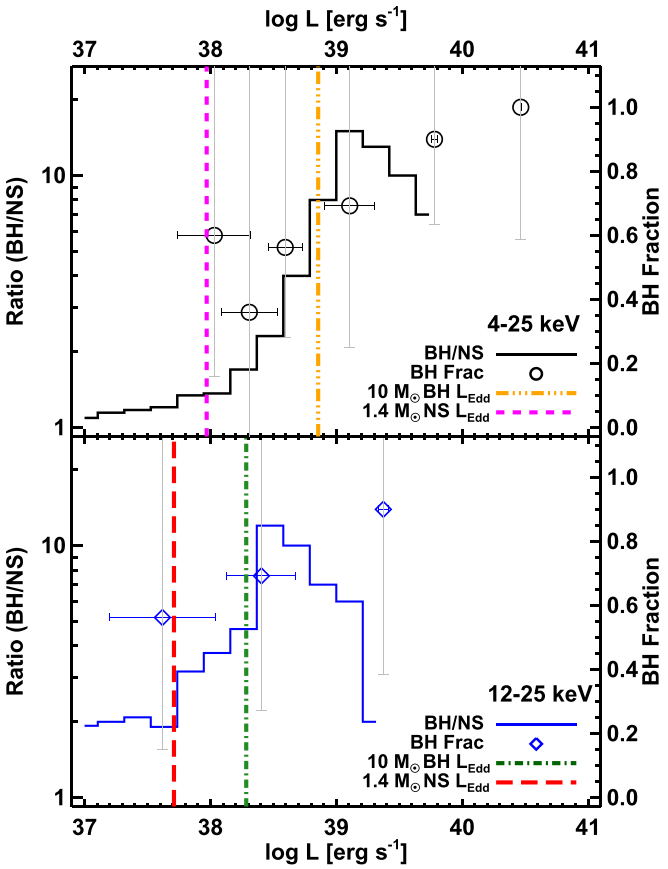

Figure 12. Ratio of the cumulative number of BHs to NSs for the 4–25 kev (top panel, black line) and 12–25 keV (bottom panel, blue line) sources. The lines are cutoff where no NSs are detected/classified, even though BHs are found at larger $L_{\rm X}$. We also show the BH fraction $N_{\rm BH}/(N_{\rm BH}+N_{\rm NS})$, in the 4–25 (12–25) keV energy band as black circles (blue diamonds), each grouped in bins of 9 BH sources, except the 4–25 keV bin at highest $L_{\rm X}$ that has 2 BH sources. BH fraction 1σ uncertainties were calculated using Poisson statistics (Gehrels 1986). We found that the overall ratio of BH to NS was ≈ 1 for the 4–25 keV and ≈ 2 for 12–25 keV energy band. The 4–25 keV BH fraction decreases at the bolometric Eddington limit for a 1.4 $M_\odot$ NS (beyond the 4–25 keV value), suggesting a copious NS population at this $L_{\rm X}$ (see Section 5.3.1 for details).

12–25 keV analysis are the similar ratios and shapes of both histograms.

The BH fraction enables us to study the relation between the BH and NS population at larger $L_{\rm X}$ compared to the BH/NS ratio. Beyond the Eddington limits for a 1.4 $M_\odot$ NS in each energy band, we see an approximately monotonic increase in the BH fraction, as expected. The BH fraction reaches 75% near the 4–25 keV 10 $M_\odot$ BH Eddington limit, quickly approaching unity at the highest $L_{\rm X}$. The 4–25 keV BH fraction decreases below 40% at the bolometric Eddington limit for a 1.4 $M_\odot$ NS, but given the lone data point to the left and uncertainties, this may not indicate a copious NS population at this $L_{\rm X}$. To determine if NS cluster near their Eddington luminosities requires a larger sample with uniform completeness for $L_{\rm X} < 10^{38}$ erg s^{-1}.

From our previous analysis we quoted 47 BHs and 43 NSs that were detected in the 4–25 keV energy band, giving a ratio of ≈ 1 across our luminosity range. We did not detect/identify many BHs at faint luminosities compared with NSs (4–25 keV), however, the opposite is true at high-$L_{\rm X}$ in both energy bands. A broader sample with uniform completeness will be required to eliminate ambiguities. The 12–25 keV ratio maintains a similar shape when

scaling the 4–25 keV luminosity by ≈50%. When determining totals for BHs and NSs, we found the 12–25 keV band had a ratio of $27/14 \approx 2$, a factor of 2 larger than the 4–25 keV band, suggesting that BH XRBs are harder than NS XRBs. When comparing relative percentages to the 4–25 keV band, a lack of detected NS sources in the 12–25 keV band is apparent, possibly due to the softer spectra of Z/Atolls NS. Whether this ratio of unity holds down to the lower limit for actively accreting ("luminous") XRBs at $\approx 10^{36}$ erg s^{-1} and into the quiescent XRB range will require deeper data.

6. Conclusions and Future Directions

Using a *NuSTAR*-selected sample of 12 late-type and dwarf galaxies, we investigated the 4–25 keV properties of the XRB population. With novel diagnostic methods that leverage the $E > 10$ keV energy band, we were able to distinguish between compact object types and accretion states via hardness-intensity and color–color diagrams. Specifically, we were able to classify 90/128 sources in the 4–25 keV energy band: 47 BHs and 43 NSs. This is a marked improvement from previous studies where identifying extragalactic XRB compact object types and spectral states has only been possible for a select few of the brightest systems.

We studied the relationship between BHs and NSs and the sSFR of a galaxy. A Spearman's rank test on the BH fraction, $N_{\rm BH}/(N_{\rm BH} + N_{\rm NS})$, versus sSFR gave a p-value of 0.072 and coefficient $r_s = 0.56$, indicating weak monotonicity but no correlation. Including M31, which is dominated by NSs and has a low sSFR, we obtained a p-value of 0.028 and coefficient $r_s = 0.63$. The data suggests that BHs dominate star-forming galaxies and NSs dominate low-sSFR galaxies. However, due to the varying sensitivity and completeness of our sample, we require improved statistics to investigate this further. Similarly, while there were indications from the data, in agreement with theoretical expectations, that accreting pulsars dominate at a high sSFR and Z/Atoll sources were prevalent at a low sSFR, no statistically significant correlation was found. We found that most BHs were identified with the hard accretion state, regardless of host galaxy sSFR, similar to the Galactic BH HMXB Cygnus X-1. Subsequent analysis of the rich multi-wavelength data sets using UV/optical/IR catalogs (in combination with the *NuSTAR-Chandra/XMM-Newton* data we analyzed) can help confirm the nature of these sources.

We classified galaxies as BH-, NS-, and ULX-dominated if >70% of their total 4–25 or 12–25 keV X-ray point source emission came from one of these groups. We found that galaxies with an sSFR $\gtrsim 2 \times 10^{-9}$ yr^{-1} were all ULX-dominated, which included all four dwarf galaxies in our sample as well as the starburst galaxies IC 342 and M82. Most galaxies were BH-dominated, whereas in the 4–25 keV energy band, only M31 and NGC 4945 were NS-dominated. We confirmed the $L_{\rm X}$–SFR correlation from previous studies by investigating the eight normal (Milky Way-type) galaxies in the *NuSTAR* sample with an SFR of 0.3–12.5 $M_\odot$ yr^{-1}. The best-fitting parameters for the relation $\log L_{\rm X} = \log A + B\log{\rm SFR}$ can be found in Table 7. The 4–25 keV result was nearly identical to previous work in the 2–10 keV range despite the use of different galaxy samples.

We constrained the correlation of X-ray luminosity with the SFR and stellar mass using the relationship $L_{\rm X} = \alpha M_\star + \beta{\rm SFR}$. We determined the best-fitting values (see Table 8) for α and β based on the eight normal (Milky Way-type) galaxies in the *NuSTAR* sample. In particular, the four dwarf galaxies had increased $L_{\rm X}/{\rm SFR}$ compared to normal galaxies, based on past scaling relations. This is not surprising as these dwarf galaxies were selected as ULX hosts, and as such are a biased sample. Studying an unbiased sample of dwarf galaxies would help determine a statistically significant $L_{\rm X}/{\rm SFR}$ relation. With the introduction of new programs/observatories to identify faint dwarf galaxies in the optical (e.g., Dragonfly, Abraham & van Dokkum 2014; Dark Energy Survey, Dark Energy Survey Collaboration et al. 2016), multiwavelength studies incorporating X-ray emission would improve our constraints on X-ray source populations in the low-mass regime.

We measured galaxy XLFs in the 4–25 and 12–25 keV energy bands, including the first $E > 10$ keV extragalactic XLF for an ensemble of galaxies. We determined that the combined XLF of all sample galaxies in each energy band followed that of the canonical HMXB XLF found by previous studies at $E < 10$ keV. Using the classifications for BHs and NSs, we produced cumulative BH and NS XLFs in the 4–25 and 12–25 keV energy bands. The 4–25 and 12–25 keV NS XLFs each indicated a decline beginning at $\approx 10^{38}$ and $\approx 6 \times 10^{37}$ erg s^{-1}, respectively, attributable to the 1.4 $M_\odot$ NS Eddington limit. Increased sensitivity and completeness in the 12–25 keV energy band is required to confirm the decline seen in the 12–25 keV NS XLF.

Using our classifications we investigated the characteristics of BHs and NSs at different $L_{\rm X}$, with a focus on behavior near the Eddington limits. We calculated the overall BH to NS ratio, finding $N_{\rm BH}/N_{\rm NS} \approx 1$ (4–25 keV) and $N_{\rm BH}/N_{\rm NS} \approx 2$ (12–25 keV), over a 4–25 and 12–25 keV luminosity range for all the detected sources of $\sim 10^{37}$–$10^{40.5}$ and $\sim 10^{37}$–10^{40} erg s^{-1}, respectively. We found that the 4–25 keV ratio of BH to NS increased from a value of 1 past the 4–25 keV Eddington limit for a 1.4 $M_\odot$ NS and reached a maximum value of 15 near the 4–25 keV Eddington limit for a 10 $M_\odot$ BH. However, while the total number of accreting stellar-mass BHs may decrease beyond the 10 $M_\odot$ BH $L_{\rm Edd}$, an improved statistical sample is required to determine its validity. To extend to larger $L_{\rm X}$ we investigated the BH fraction, $N_{\rm BH}/(N_{\rm BH}+N_{\rm NS})$, finding approximately monotonic increase beyond the Eddington limits for a 1.4 $M_\odot$ NS in both energy bands. We found evidence for a decrease in the BH fraction below 40% beyond the 4–25 keV Eddington limit for a 1.4 $M_\odot$ NS (the data point was coincident with the bolometric Eddington limit for a 1.4 $M_\odot$ NS). A larger sample with uniform completeness for $L_{\rm X} < 10^{38}$ erg s^{-1} is required to determine if NS cluster near their Eddington luminosities.

This galaxy sample was biased toward late-type/spiral galaxies and contained no early-type galaxies, meaning that we did not offer a comprehensive view of older stellar populations. Future observations that focus on building a sample of elliptical galaxies would be of great interest. Such galaxies have inherently faint LMXB populations and thus require extended observing campaigns. However, the nearest candidate, Cen A, is problematic due to its AGN, and most giant elliptical galaxies are located at $d \gtrsim 10$ Mpc, prohibiting resolved XRB studies with *NuSTAR*. Therefore, to improve our understanding of the XRB population in elliptical galaxies at $E > 10$ keV requires a next-generation hard X-ray telescope. Using our XRB classifications and XLFs enables comparison with binary population synthesis modeling (Fragos et al. 2009; Sørensen et al. 2017) that predicts the NS and BH-XRB populations in these galaxies. Expanding the range of sSFR

coupled with increased sensitivity has the potential to profoundly impact the study of accreting compact objects.

We thank the referee for useful comments that improved the manuscript. V.A. acknowledges financial support from NASA grant NNX15AR30G. This research made use of ASTROPY, a community-developed core PYTHON package for Astronomy (Astropy Collaboration et al. 2013). We acknowledge the usage of the HyperLeda database (http://leda.univ-lyon1.fr). This research has made use of the NED, which is operated by the Jet Propulsion Laboratory, California Institute of Technology, under contract with the National Aeronautics and Space Administration.

Facilities: *NuSTAR*, *CXO* (ACIS), *XMM* (PN, MOS).

Software: astropy (Astropy Collaboration et al. 2013).

Appendix
Notes on Individual Galaxies

A.1. IC 342

IC 342 is a nearly face-on spiral galaxy with intense star formation activity in its core (Becklin et al. 1980). A member of the IC 342/Maffei group of galaxies, it is located near the Galactic plane at $b \sim 10°$, making it difficult to constrain X-ray emission $\lesssim$1 keV. IC 342 has been studied by all major X-ray observatories over the past four decades. *Chandra* high-resolution camera imaging (HRC-I) of the central 30′ by 30′ region by Mak et al. (2008) resulted in the detection of 23 sources. They found that one of the three historical ULXs detected by *Einstein* was actually coincident with the nuclear center and thus not a ULX. Multiple ACIS-S observations have been used to study the spectrum of ULX IC 342 X-1 and to create a point source catalog consisting of 61 sources (Liu 2011). Mak et al. (2011) studied the long-term flux and spectral variability of a 35′ by 30′ region with *XMM-Newton* to a limiting luminosity of 10^{37} erg s^{-1}; 39 of the 61 detected sources showed long-term variability, 26 of which were classified as X-ray transients. Of the identified transients, eight also showed spectral variability indicative of XRBs. Rana et al. (2015) recently used two epochs of *NuSTAR*/*XMM-Newton* observations to investigate the two ULXs in IC 342. They found luminosities of $\sim 10^{40}$ and 7.4×10^{39} erg s^{-1} for sources X-1 and X-2, respectively. Joint spectral fitting of each source ruled out the possibility of a BH binary in a low/hard accretion state. They concluded that further broadband spectral studies are needed to identify the origin of the spectral components.

A.2. M83

M83 (NGC 5236) is a nearly face-on grand design spiral galaxy with an SFR of $\sim 3\ M_\odot$ yr^{-1}. These characteristics have made it an ideal object for X-ray population studies. A deep (790 ks) *Chandra* ACIS survey of M83 by Long et al. (2014) detected 378 point sources within the D_{25} ellipse and reached luminosities of $\sim 10^{36}$ erg s^{-1}. Based on multiwavelength data they identified 87 supernova remnant (SNR) candidates, which dominated the population in the disk. Long et al. (2014) classified X-ray point sources using spectral and temporal analysis. Spectral fitting of the 29 brightest (>2000 counts) sources showed that most of the SNRs were associated with the spiral arms while the harder sources (likely XRBs) were not. Analysis of the cleaned XLF (foreground sources, AGNs, and SNRs removed) indicated that most of the XRBs in the disk are LMXBs as opposed to HMXBs. The recent *NuSTAR*/*XMM-Newton*/*Chandra* survey by Yukita et al. (2016) detected 21 point sources and found that the hard X-ray emission $E > 10$ keV was dominated by intermediate accretion state BH XRBs and NS LMXBs.

A.3. M82

M82 (NGC 3034) is an example of an extreme starbursting galaxy with an SFR of 12 $M_\odot$ yr^{-1}. Part of the M81 group of galaxies, the starburst is likely a result of interaction with M81. Until the launch of *Chandra*, the discrete X-ray point source population of M82 was not well studied due to the large number density of sources in the nucleus and the presence of X-ray emission from hot gas from the starburst. To date, most studies still focus on the brightest few point sources as opposed to the population. M82 has more luminous XRBs (i.e., a flatter XLF; Kilgard et al. 2002) and its luminous source population appears to be HMXBs associated with young star clusters (Zezas et al. 2004), exhibiting variability and spectral shapes consistent with BH HMXBs (Kilgard 2007; Chiang & Kong 2011). M82 has been particularly well studied in X-rays due to the large population of six ULXs (Gladstone et al. 2013), the brightest of which reside in the nucleus, X-1 and X-2. M82 X-1 was long thought to be an intermediate-mass BH due to its super-Eddington luminosity, an idea that has recently been confirmed. Pasham et al. (2014) used *RXTE* data to measure the quasi-periodic oscillations of the source and estimated the mass of the BH to be $429 \pm 105\ M_\odot$. This important discovery bridged the divide between stellar mass BHs in XRBs and supermassive BHs at the centers of most galaxies. At nearly the same time as this discovery concerning M82 X-1, the ULX M82 X-2, which was long thought to be an intermediate-mass BH candidate, was discovered to be the first-ever confirmed ULX *pulsar*. Bachetti et al. (2014b) discovered pulsed emission spatially coincident with M82 X-2 using *NuSTAR*/*Chandra*/*Swift* data, confirming X-2 as a NS. M82 X-2 reaches 100 times the Eddington limit for an NS, with a peak luminosity L_X (0.3–10 keV) of 1.8×10^{40} erg s^{-1}. This result challenged the theory of accretion on to magnetized NS and has led to studies on what fraction of ULXs are NSs rather than BHs (e.g., Fragos et al. 2015; Shao & Li 2015; Wiktorowicz et al. 2015; King & Lasota 2016).

A.4. NGC 253

NGC 253 is also an edge-on starburst galaxy with a similarly high SFR of 6 $M_\odot$ yr^{-1}. Although distance estimates vary, a census of ULXs in the nearby (<5 Mpc) universe by Gladstone et al. (2013) reported that eight ULXs reside in NGC 253. Vogler & Pietsch (1999) used *ROSAT* to detect 32 sources within the D_{25} ellipse of NGC 253 to a luminosity of 7×10^{36} erg s^{-1}. They showed that most sources exhibit time variability and are likely XRBs. Pietsch et al. (2001) studied the 10 brightest sources in NGC 253 using *XMM-Newton* data and classified them using 0.5–10 keV color diagnostics. They identified three sources with soft colors as likely LMXBs and noted most sources showed time variability, also indicative of LMXBs. The recent *NuSTAR*/*Chandra* study by Lehmer et al. (2013) determined that the ULX source dominating the entire galaxy over 0.5–30 keV is distinct from the nuclear SMBH,

which apparently was actively accreting a decade prior and had turned off in the 2012 observations. A comprehensive study of the *NuSTAR* point sources by Wik et al. (2014b) detected 21 sources (4–25 keV) and found that most were BH XRBs in an intermediate accretion state.

A.5. M81

M81 (NGC 3031) is a nearby grand design spiral galaxy with a low SFR and a low-ionization nuclear emission region. The X-ray population of M81 has been studied by *Einstein* (Fabbiano 1988), *ROSAT* (Immler & Wang 2001), and *Chandra* (Tennant et al. 2001; Swartz et al. 2003). The most comprehensive analysis was completed by Sell et al. (2011), who used 220 ks of *Chandra* data from 16 observations to classify and investigate the variability of 265 sources detected above $\sim 10^{37}$ erg s^{-1}. They found significant variability in ~36%–60% of their sources but concluded that snapshot observations provided a consistent determination of the XLF of M81. Color diagnostics identified large numbers of many different source types such as LMXBs, HMXBs, and SNRs.

A.6. M31

M31 is both the nearest large spiral galaxy and most similar to the Milky Way, and thus has been the target of the most detailed studies of any extragalactic X-ray point source population (e.g., Trinchieri & Fabbiano 1991; Supper et al. 2001; Peacock et al. 2010; Barnard et al. 2014a; Henze et al. 2014). Previous *Chandra* observations have mostly been focused on monitoring the bulge region for both the activity of the SMBH as well as XRB variability, until the recent 2015 *Chandra* Large Project to cover the Panchromatic Hubble Andromeda Treasury (PHAT; Dalcanton et al. 2012) survey area (PI: B. F. Williams). Notable results included the finding that the XLF of the bulge was flatter than the disk (Kong et al. 2002; Williams et al. 2004; Vulic et al. 2016), at odds with studies of other spiral galaxies (Colbert et al. 2004; Binder et al. 2012). Stiele et al. (2011) used *XMM-Newton* data covering an area greater than the D_{25} ellipse to compile a catalog of 1897 sources above $\sim 10^{35}$ erg s^{-1}. Source classification techniques included using X-ray hardness ratios, spatial extent of the sources, long-term X-ray variability, and cross-correlation with X-ray, optical, infrared, and radio catalogs. Despite their robust analysis, 65% of their sources remained unclassified. This included only having 2 HMXB candidates to add to the 18 candidates found by Shaw Greening et al. (2009), which was unusual given that there are ~100 HMXBs in the Milky Way. This prompted a *Chandra* legacy survey of the M31 disk (PI: B. F. Williams) to complement the PHAT survey (Dalcanton et al. 2012). A *NuSTAR* legacy project was begun in early 2014 to cover part of the *Chandra*-PHAT area (P.I. A. E. Hornschemeier) and *NuSTAR* GO observations of the bulge have occurred in Cycles 1–3 (P.I. M. Yukita). Details about the M31 source population are given in papers on the globular cluster LMXB population (Maccarone et al. 2016), which comprises most of the bright X-ray sources in M31, and the bright pulsar candidate dominating the entire galaxy at $E > 25$ keV (Yukita et al. 2017).

A.7. NGC 5204

NGC 5204 is a Magellanic spiral galaxy that is part of the M101 group of galaxies and has a large sSFR comparable to that of M82. The ULX X-1 originally discovered by *Einstein* (Fabbiano & Panagia 1982) has been the motivation for most X-ray/multiwavelength observations of NGC 5204. Roberts et al. (2006) used a 2 month *Chandra* monitoring campaign to study the variability of X-1 and found that its spectrum became harder (e.g., heating of the corona) as its flux increased. They found no evidence supporting the presence of an intermediate-mass BH in X-1. Mukherjee et al. (2015) used two epochs of *NuSTAR*/*XMM-Newton* coverage of X-1 to study its 0.3–20 keV properties. No significant spectral variations were observed for the 5×10^{39} erg s^{-1} source and the broadband spectrum was consistent with super-Eddington accretion on to a stellar-mass BH.

A.8. NGC 1313

NGC 1313 is an isolated peculiar spiral galaxy with starburst activity and a similar sSFR to that of NGC 5204. It has a specific frequency of young massive star clusters similar to that of M83 (Larsen & Richtler 1999) and a concentration of stars at a stellar age of ≈200 Myr. Trudolyubov (2008) discovered a transient X-ray pulsar in *XMM-Newton* data with a period of 766 s that reached L_X (0.3–7 keV) $\approx 2 \times 10^{39}$ erg s^{-1}. Based on the X-ray properties it was classified as a B*e* X-ray pulsar candidate. Bachetti et al. (2013) recently investigated the 0.3–30 keV spectra of the ULXs X-1 and X-2 with *NuSTAR*/*XMM-Newton* observations. While X-2 was not detected for $E > 10$ keV, X-1 showed a clear spectral cutoff that ruled out a BH in a low/hard accretion state. The characteristics of a large spectral variation found in X-2 was indicative of a BH in the hard state.

A.9. NGC 4945

NGC 4945 is an edge-on barred spiral starburst galaxy with a type II Seyfert nucleus. The galaxy is the brightest extragalactic hard X-ray source (~50–100 keV) and hosts one of the nearest AGN. The nuclear region contains an obscured starburst region with a 10″ ring morphology (Schurch et al. 2002). Most X-ray investigations have focused on the AGN, although multiple *Chandra* studies (Colbert et al. 2004; Kaaret & Alonso-Herrero 2008; Liu 2011) have detected up to ≈50 X-ray sources in NGC 4945 to sensitivities of $\sim 10^{37}$ erg s^{-1}. In particular, *Chandra* (Swartz et al. 2004) and *XMM-Newton* (Berghea et al. 2008) studies found two ULXs that were used as part of a review of nearby galaxy ULX populations. Colbert et al. (2004) calculated a cumulative XLF slope of $\gamma = 0.7$ using 22 X-ray point sources, finding agreement with other spiral galaxies in their sample. SN 2011ja occurred in NGC 4945 and was studied by Chakraborti et al. (2013) using *Chandra*. X-ray observations allowed the authors to probe the history of variable mass loss from the progenitor, suggesting that SN may interact with circumstellar material ejected by non-steady winds (varying densities). Puccetti et al. (2014) used *NuSTAR* observations in combination with other archival X-ray data of NGC 4945 to investigate the spectral properties and variability of the galaxy. They found strong spectral variability above $E > 10$ keV and that most of the high-energy flux was transmitted rather than Compton-scattered.

A.10. Circinus

Circinus is a spiral galaxy with a similar sSFR to that of the Milky Way but located 4° below the Galactic plane, thus having a large $N_{\rm H}$. Circinus is an active galaxy with a type II Seyfert nucleus and complex structure. It has been observed many times by various X-ray observatories (e.g., Smith & Wilson 2001; Bianchi et al. 2002; Yang et al. 2009). Bauer et al. (2001) completed the first point source population study with *Chandra*, detecting 16 point sources to a 0.5–10 keV sensitivity of 10^{37} erg s^{-1}, with 25% of the sources being variable. Walton et al. (2013) studied Circinus ULX5 (there are four other known/candidate ULXs in Circinus, e.g., Swartz et al. 2004; Ptak et al. 2006), a variable source in the outskirts of the galaxy beyond D_{25}, using coordinated *NuSTAR-XMM-Newton* observations and archival X-ray data from other observatories. They determined a 0.3–30 keV luminosity of 1.6×10^{40} erg s^{-1} and BH mass of 90 $M_\odot$, found variability on long timescales of at least a factor of ∼5, and spectral variability similar to luminous Galactic BH XRBs. Esposito et al. (2015) used archival *Chandra-XMM-Newton* observations and discovered two pulsators that were identified as likely foreground cataclysmic variables. The ULX candidate CG X-1 had properties consistent with a Wolf-Rayet BH XRB, the rare class of sources for which only 4 confirmed and 3 candidates exist.

A.11. Holmberg II

Holmberg II is a dwarf irregular galaxy that is part of the M81 group and has properties very similar to the Small Magellanic Cloud. Kerp et al. (2002) detected 31 X-ray sources located within the H I column density distribution of Holmberg II to a sensitivity of 10^{37} erg s^{-1} using *ROSAT* PSPC data. Many studies of Holmberg II have focused on the unique ULX source Holmberg II X-1, located inside the "Foot nebula," from radio (Miller et al. 2005) to the optical (Abolmasov et al. 2007) and IR (Berghea et al. 2010a; Heida et al. 2016). Many interpretations for the nature of this ULX have been put forth, although there has been general consensus for a ≈100 $M_\odot$ BH (e.g., Goad et al. 2006; Berghea et al. 2010b). Walton et al. (2015) studied the 0.3–25 keV emission from the ULX Holmberg II X-1 with *NuSTAR-XMM-Newton-Suzaku* observations, finding $L_{\rm X} = 8.1 \times 10^{39}$ erg s^{-1}, which is typical for this source. They implied that the source was accreting near or above its Eddington limit and found 90% of the flux was emitted at $E < 10$ keV. Egorov et al. (2017) analyzed the structure and kinematics of ionized gas around X-1 using optical emission lines, finding evidence that the ULX may have escaped its parent star cluster.

A.12. Holmberg IX

Holmberg IX is a dwarf irregular galaxy that is also part of the M81 group, located near the outskirts of M81's D_{25} ellipse. It is the nearest young galaxy, having stellar populations with ages $\lesssim$200 Myr and dominated by blue and red supergiants. Thought to be formed by the recent tidal interaction between M81 and another M81 group galaxy, Holmberg IX hosts one of the best-studied ULXs (Ho IX X-1, also known as M81 X-9), which is persistently detected at $L_{\rm X}$ (0.3–10 keV) $>10^{40}$ erg s^{-1} (e.g., Walton et al. 2014). First discovered by the *Einstein* observatory (Fabbiano 1988), X-1 has been well studied by all X-ray observatories (e.g., La Parola et al. 2001; Walton et al. 2014). *XMM-Newton* observations initially revealed a cool accretion disk ($kT \sim 0.1 - 0.2$ keV), suggesting an intermediate-mass BH (e.g., Miller et al. 2004a, 2004b). However, recent work has indicated a spectrum consistent with a 100 $M_\odot$ BH accreting at the Eddington limit or a 10 $M_\odot$ BH above $L_{\rm Edd}$ (Kong et al. 2010). *NuSTAR* was critical in confirming the spectral cutoff and disfavoring an intermediate-mass BH (Walton et al. 2014, 2017).

ORCID iDs

N. Vulic https://orcid.org/0000-0001-7855-8336
A. E. Hornschemeier https://orcid.org/0000-0001-8667-2681
D. R. Wik https://orcid.org/0000-0001-9110-2245
M. Yukita https://orcid.org/0000-0001-6366-3459
A. Zezas https://orcid.org/0000-0001-8952-676X
A. F. Ptak https://orcid.org/0000-0001-5655-1440
B. D. Lehmer https://orcid.org/0000-0003-2192-3296
V. Antoniou https://orcid.org/0000-0001-7539-1593
T. J. Maccarone https://orcid.org/0000-0003-0976-4755
B. F. Williams https://orcid.org/0000-0002-7502-0597
F. M. Fornasini https://orcid.org/0000-0002-9286-9963

References

Abbott, B. P., Abbott, R., Abbott, T. D., et al. 2016, PhRvL, 116, 061102
Abbott, B. P., Abbott, R., Abbott, T. D., et al. 2017a, PhRvL, 118, 221101
Abbott, B. P., Abbott, R., Abbott, T. D., et al. 2017b, PhRvL, 119, 141101
Abolmasov, P., Fabrika, S., Sholukhova, O., & Afanasiev, V. 2007, AstBu, 62, 36
Abraham, R. G., & van Dokkum, P. G. 2014, PASP, 126, 55
Ajello, M., Alexander, D. M., Greiner, J., et al. 2012, ApJ, 749, 21
Antoniou, V., & Zezas, A. 2016, MNRAS, 459, 528
Antoniou, V., Zezas, A., Hatzidimitriou, D., & Kalogera, V. 2010, ApJL, 716, L140
Astropy Collaboration, Robitaille, T. P., Tollerud, E. J., et al. 2013, A&A, 558, A33
Bachetti, M., Barret, D., Boggs, S. E., et al. 2014a, in EPJ Web Conf. 64, Physics at the Magnetospheric Boundary, ed. E. Bozzo et al. (EDP: London), 06010
Bachetti, M., Harrison, F. A., Walton, D. J., et al. 2014b, Natur, 514, 202
Bachetti, M., Rana, V., Walton, D. J., et al. 2013, ApJ, 778, 163
Barnard, R., Garcia, M. R., Primini, F., et al. 2014a, ApJ, 780, 83
Barnard, R., Garcia, M. R., Primini, F., & Murray, S. S. 2014b, ApJ, 791, 33
Basu-Zych, A. R., Lehmer, B., Fragos, T., et al. 2016, ApJ, 818, 140
Bauer, F. E., Brandt, W. N., Sambruna, R. M., et al. 2001, AJ, 122, 182
Becklin, E. E., Gatley, I., Matthews, K., et al. 1980, ApJ, 236, 441
Belloni, T. M., & Motta, S. E. 2016, in Astrophysics of Black Holes: From Fundamental Aspects to Latest Developments, ed. C. Bambi (Berlin: Springer), 61
Bendo, G. J., Henkel, C., D'Cruze, M. J., et al. 2016, MNRAS, 463, 252
Berghea, C. T., Dudik, R. P., Weaver, K. A., & Kallman, T. R. 2010a, ApJ, 708, 354
Berghea, C. T., Dudik, R. P., Weaver, K. A., & Kallman, T. R. 2010b, ApJ, 708, 364
Berghea, C. T., Weaver, K. A., Colbert, E. J. M., & Roberts, T. P. 2008, ApJ, 687, 471
Bianchi, S., Matt, G., Fiore, F., et al. 2002, A&A, 396, 793
Binder, B., Gross, J., Williams, B. F., et al. 2017, ApJ, 834, 128
Binder, B., Williams, B. F., Eracleous, M., et al. 2012, ApJ, 758, 15
Bondi, H., & Hoyle, F. 1944, MNRAS, 104, 273
Bottacini, E., Ajello, M., & Greiner, J. 2012, ApJS, 201, 34
Bradshaw, C. F., Fomalont, E. B., & Geldzahler, B. J. 1999, ApJL, 512, L121
Brightman, M., Harrison, F., Walton, D. J., et al. 2016, ApJ, 816, 60
Calzetti, D. 2013, in Star Formation Rate Indicators, ed. J. Falćon-Barroso & J. H. Knapen (Cambridge: Cambridge Univ. Press), 419
Casagrande, L., Ramírez, I., Meléndez, J., & Asplund, M. 2012, ApJ, 761, 16
Cash, W. 1979, ApJ, 228, 939
Chakraborti, S., Ray, A., Smith, R., et al. 2013, ApJ, 774, 30

Chiang, Y.-K., & Kong, A. K. H. 2011, MNRAS, 414, 1329
Church, M. J., Gibiec, A., & Bałucińska-Church, M. 2014, MNRAS, 438, 2784
Clark, J. S., Bartlett, E. S., Broos, P. S., et al. 2015, A&A, 579, A131
Colbert, E. J. M., Heckman, T. M., Ptak, A. F., Strickland, D. K., & Weaver, K. A. 2004, ApJ, 602, 231
Corral-Santana, J. M., Casares, J., Muñoz-Darias, T., et al. 2016, A&A, 587, A61
Dalcanton, J. J., Williams, B. F., Lang, D., et al. 2012, ApJS, 200, 18
Dale, D. A., Cohen, S. A., Johnson, L. C., et al. 2009, ApJ, 703, 517
Dark Energy Survey Collaboration, Abbott, T., Abdalla, F. B., et al. 2016, MNRAS, 460, 1270
Das, A., Mesinger, A., Pallottini, A., Ferrara, A., & Wise, J. H. 2017, MNRAS, 469, 1166
Davidge, T. J. 2016, ApJ, 818, 142
Del Moro, A., Alexander, D. M., Aird, J. A., et al. 2017, ApJ, 849, 57
Done, C., Gierliński, M., & Kubota, A. 2007, A&ARv, 15, 1
Doroshenko, V., Ducci, L., Santangelo, A., & Sasaki, M. 2014, A&A, 567, A7
Egorov, O. V., Lozinskaya, T. A., & Moiseev, A. V. 2017, MNRAS, 467, L1
Elbert, O. D., Bullock, J. S., & Kaplinghat, M. 2018, MNRAS, 473, 1186
Engelbracht, C. W., Rieke, M. J., Rieke, G. H., Kelly, D. M., & Achtermann, J. M. 1998, ApJ, 505, 639
Esposito, P., Israel, G. L., Milisavljevic, D., et al. 2015, MNRAS, 452, 1112
Fabbiano, G. 1988, ApJ, 325, 544
Fabbiano, G. 2006, ARA&A, 44, 323
Fabbiano, G., & Panagia, N. 1982, in NASA CP-2238, Advances in Ultraviolet Astronomy: Four Years of IUE Research, ed. Y. Kondo (Washington, DC: NASA), 145
For, B.-Q., Koribalski, B. S., & Jarrett, T. H. 2012, MNRAS, 425, 1934
Fragos, T., Kalogera, V., Willems, B., et al. 2009, ApJL, 702, L143
Fragos, T., Lehmer, B. D., Naoz, S., Zezas, A., & Basu-Zych, A. 2013, ApJL, 776, L31
Fragos, T., Linden, T., Kalogera, V., & Sklias, P. 2015, ApJL, 802, L5
Fruscione, A., McDowell, J. C., Allen, G. E., et al. 2006, Proc. SPIE, 6270, 62701V
Fürst, F., Walton, D. J., Harrison, F. A., et al. 2016, ApJL, 831, L14
Gehrels, N. 1986, ApJ, 303, 336
Gil de Paz, A., Boissier, S., Madore, B. F., et al. 2007, ApJS, 173, 185
Gilfanov, M. 2004a, MNRAS, 349, 146
Gilfanov, M. 2004b, PThPS, 155, 49
Gilfanov, M., Grimm, H.-J., & Sunyaev, R. 2004a, MNRAS, 347, L57
Gilfanov, M., Grimm, H.-J., & Sunyaev, R. 2004b, MNRAS, 351, 1365
Gladstone, J. C., Copperwheat, C., Heinke, C. O., et al. 2013, ApJS, 206, 14
Gladstone, J. C., Roberts, T. P., & Done, C. 2009, MNRAS, 397, 1836
Goad, M. R., Roberts, T. P., Reeves, J. N., & Uttley, P. 2006, MNRAS, 365, 191
Gomez, S., Mason, P. A., & Robinson, E. L. 2015, ApJ, 809, 9
Graessle, D. E., Evans, I. N., Glotfelty, K., et al. 2006, Proc. SPIE, 6270, 62701X
Grimm, H.-J., Gilfanov, M., & Sunyaev, R. 2002, A&A, 391, 923
Grimm, H.-J., Gilfanov, M., & Sunyaev, R. 2003, MNRAS, 339, 793
Grinberg, V., Hell, N., Pottschmidt, K., et al. 2013, A&A, 554, A88
Haberl, F., Israel, G. L., Rodriguez Castillo, G. A., et al. 2017, A&A, 598, A69
Haberl, F., & Sturm, R. 2016, A&A, 586, A81
Harris, J., & Zaritsky, D. 2004, AJ, 127, 1531
Harris, J., & Zaritsky, D. 2009, AJ, 138, 1243
Harrison, F. A., Aird, J., Civano, F., et al. 2016, ApJ, 831, 185
Harrison, F. A., Craig, W. W., Christensen, F. E., et al. 2013, ApJ, 770, 103
Hasinger, G., & van der Klis, M. 1989, A&A, 225, 79
Heida, M., Jonker, P. G., Torres, M. A. P., et al. 2016, MNRAS, 459, 771
Henze, M., Pietsch, W., Haberl, F., et al. 2014, A&A, 563, A2
Hornschemeier, A. E., Wolter, A., & Kim, D.-W. 2016, in Proc. IAU 29B, Astronomy in Focus, 124
Hoyle, F., & Lyttleton, R. A. 1939, PCPS, 35, 405
Immler, S., & Wang, Q. D. 2001, ApJ, 554, 202
Into, T., & Portinari, L. 2013, MNRAS, 430, 2715
Israel, G. L., Belfiore, A., Stella, L., et al. 2017a, Sci, 355, 817
Israel, G. L., Papitto, A., Esposito, P., et al. 2017b, MNRAS, 466, L48
Jarrett, T. H., Masci, F., Tsai, C. W., et al. 2013, AJ, 145, 6
Kaaret, P., & Alonso-Herrero, A. 2008, ApJ, 682, 1020
Kaaret, P., Feng, H., & Roberts, T. P. 2017, ARA&A, 55, 303
Kalberla, P. M. W., Burton, W. B., Hartmann, D., et al. 2005, A&A, 440, 775
Karachentsev, I. D., Makarov, D. I., & Kaisina, E. I. 2013, AJ, 145, 101
Kerp, J., Walter, F., & Brinks, E. 2002, ApJ, 571, 809
Kilgard, R. E. 2007, PhD thesis, Univ. Leicester
Kilgard, R. E., Kaaret, P., Krauss, M. I., et al. 2002, ApJ, 573, 138
Kim, D.-W., & Fabbiano, G. 2004, ApJ, 611, 846
King, A., & Lasota, J.-P. 2016, MNRAS, 458, L10
King, A. R., Kolb, U., & Burderi, L. 1996, ApJL, 464, L127
Koliopanos, F., Vasilopoulos, G., Godet, O., et al. 2017, A&A, 608, A47
Kong, A. K. H., Garcia, M. R., Primini, F. A., et al. 2002, ApJ, 577, 738
Kong, A. K. H., Yang, Y. J., Yen, T.-C., Feng, H., & Kaaret, P. 2010, ApJ, 722, 1816
Kormendy, J., & Ho, L. C. 2013, ARA&A, 51, 511
Krivonos, R., Revnivtsev, M., Lutovinov, A., et al. 2007, A&A, 475, 775
Krivonos, R., Tsygankov, S., Lutovinov, A., et al. 2012, A&A, 545, A27
Kroupa, P. 1998, in ASP Conf. Ser. 134, Brown Dwarfs and Extrasolar Planets, ed. R. Rebolo, E. L. Martin, & M. R. Zapatero Osorio (San Francisco, CA: ASP), 483
Kroupa, P. 2001, MNRAS, 322, 231
La Parola, V., Peres, G., Fabbiano, G., Kim, D. W., & Bocchino, F. 2001, ApJ, 556, 47
Larsen, S. S., & Richtler, T. 1999, A&A, 345, 59
Lazzarini, M., Hornschemeier, A. E., Williams, B. F., et al. 2018, ApJ, 862, 28
Lee, J. C., Gil de Paz, A., Kennicutt, R. C., Jr., et al. 2011, ApJS, 192, 6
Lehmer, B. D., Alexander, D. M., Bauer, F. E., et al. 2010, ApJ, 724, 559
Lehmer, B. D., Basu-Zych, A. R., Mineo, S., et al. 2016, ApJ, 825, 7
Lehmer, B. D., Eufrasio, R. T., Markwardt, L., et al. 2017, ApJ, 851, 11
Lehmer, B. D., Tyler, J. B., Hornschemeier, A. E., et al. 2015, ApJ, 806, 126
Lehmer, B. D., Wik, D. R., Hornschemeier, A. E., et al. 2013, ApJ, 771, 134
Licquia, T. C., & Newman, J. A. 2015, ApJ, 806, 96
Liu, J. 2011, ApJS, 192, 10
Long, K. S., Kuntz, K. D., Blair, W. P., et al. 2014, ApJS, 212, 21
Lutovinov, A. A., Grebenev, S. A., & Tsygankov, S. S. 2012, AstL, 38, 492
Lutovinov, A. A., Revnivtsev, M. G., Tsygankov, S. S., & Krivonos, R. A. 2013, MNRAS, 431, 327
Maccarone, T. J., & Coppi, P. S. 2003, MNRAS, 338, 189
Maccarone, T. J., Yukita, M., Hornschemeier, A., et al. 2016, MNRAS, 458, 3633
Madau, P., & Fragos, T. 2017, ApJ, 840, 39
Madsen, K. K., Harrison, F. A., Markwardt, C. B., et al. 2015, ApJS, 220, 8
Mak, D. S. Y., Pun, C. S. J., & Kong, A. K. H. 2008, ApJ, 686, 995
Mak, D. S. Y., Pun, C. S. J., & Kong, A. K. H. 2011, ApJ, 728, 10
Makarov, D., Prugniel, P., Terekhova, N., Courtois, H., & Vauglin, I. 2014, A&A, 570, A13
Marchant, P., Langer, N., Podsiadlowski, P., et al. 2017, A&A, 604, A55
McCall, M. L. 2014, MNRAS, 440, 405
McClintock, J. E., & Remillard, R. A. 2006, in Compact Stellar X-ray Sources, ed. W. H. G. Lewin & M. van der Klis (Cambridge: Cambridge Univ. Press), 157
McGaugh, S. S., & Schombert, J. M. 2014, AJ, 148, 77
Mereminskiy, I. A., Krivonos, R. A., Lutovinov, A. A., et al. 2016, MNRAS, 459, 140
Mesinger, A., Ewall-Wice, A., & Hewitt, J. 2014, MNRAS, 439, 3262
Miller, J. M., Fabian, A. C., & Miller, M. C. 2004a, ApJ, 607, 931
Miller, J. M., Fabian, A. C., & Miller, M. C. 2004b, ApJL, 614, L117
Miller, N. A., Mushotzky, R. F., & Neff, S. G. 2005, ApJL, 623, L109
Mineo, S., Fabbiano, G., D'Abrusco, R., et al. 2014, ApJ, 780, 132
Mineo, S., Gilfanov, M., & Sunyaev, R. 2012, MNRAS, 419, 2095
Mineo, S., Rappaport, S., Steinhorn, B., et al. 2013, ApJ, 771, 133
Mukherjee, E. S., Walton, D. J., Bachetti, M., et al. 2015, ApJ, 808, 64
Nowak, M. A., Juett, A., Homan, J., et al. 2008, ApJ, 689, 1199
Pacucci, F., Mesinger, A., Mineo, S., & Ferrara, A. 2014, MNRAS, 443, 678
Paltani, S., Walter, R., McHardy, I. M., et al. 2008, A&A, 485, 707
Pasham, D. R., Strohmayer, T. E., & Mushotzky, R. F. 2014, Natur, 513, 74
Peacock, M. B., Maccarone, T. J., Kundu, A., & Zepf, S. E. 2010, MNRAS, 407, 2611
Peacock, M. B., & Zepf, S. E. 2016, ApJ, 818, 33
Pecaut, M. J., & Mamajek, E. E. 2013, ApJS, 208, 9
Pejcha, O., & Thompson, T. A. 2015, ApJ, 801, 90
Persic, M., & Rephaeli, Y. 2007, A&A, 463, 481
Pietsch, W., Roberts, T. P., Sako, M., et al. 2001, A&A, 365, L174
Press, W. H., Teukolsky, S. A., Vetterling, W. T., & Flannery, B. P. 2002, Numerical Recipes in C++: the art of Scientific Computing (2nd ed.; New York: Cambridge Univ. Press)
Ptak, A., Colbert, E., van der Marel, R. P., et al. 2006, ApJS, 166, 154
Puccetti, S., Comastri, A., Fiore, F., et al. 2014, ApJ, 793, 26
R Development Core Team 2008, in R: A Language and Environment for Statistical Computing, R Foundation for Statistical Computing
Rana, V., Harrison, F. A., Bachetti, M., et al. 2015, ApJ, 799, 121
Ranalli, P., Comastri, A., & Setti, G. 2003, A&A, 399, 39
Reig, P. 2011, Ap&SS, 332, 1
Remillard, R. A., & McClintock, J. E. 2006, ARA&A, 44, 49

Revnivtsev, M., Lutovinov, A., Churazov, E., et al. 2008, A&A, 491, 209
Ricci, D., Israel, G. L., & Stella, L. 1995, A&A, 299, 731
Roberts, T. P., Kilgard, R. E., Warwick, R. S., Goad, M. R., & Ward, M. J. 2006, MNRAS, 371, 1877
Rodríguez-Merino, L. H., Rosa-González, D., & Mayya, Y. D. 2011, ApJ, 726, 51
Sarazin, C. L., Irwin, J. A., & Bregman, J. N. 2000, ApJL, 544, L101
Sazonov, S., & Khabibullin, I. 2017, MNRAS, 468, 2249
Sazonov, S., Revnivtsev, M., Krivonos, R., Churazov, E., & Sunyaev, R. 2007, A&A, 462, 57
Schulz, N. S., Hasinger, G., & Truemper, J. 1989, A&A, 225, 48
Schurch, N. J., Roberts, T. P., & Warwick, R. S. 2002, MNRAS, 335, 241
Sell, P. H., Pooley, D., Zezas, A., et al. 2011, ApJ, 735, 26
Shao, Y., & Li, X.-D. 2015, ApJ, 802, 131
Shaw Greening, L., Barnard, R., Kolb, U., Tonkin, C., & Osborne, J. P. 2009, A&A, 495, 733
Shtykovskiy, P., & Gilfanov, M. 2005, MNRAS, 362, 879
Sick, J., Courteau, S., Cuillandre, J.-C., et al. 2015, in IAU Symp. 311, Galaxy Masses as Constraints of Formation Models, ed. M. Cappellari & S. Courteau (Cambridge: Cambridge Univ. Press), 82
Smith, D. A., & Wilson, A. S. 2001, ApJ, 557, 180
Smith, D. M., Heindl, W. A., & Swank, J. H. 2002, ApJ, 569, 362
Sobolewska, M. A., Gierliński, M., & Siemiginowska, A. 2009, MNRAS, 394, 1640
Sørensen, M., Fragos, T., Steiner, J. F., et al. 2017, A&A, 597, A12
Stiele, H., Pietsch, W., Haberl, F., et al. 2011, A&A, 534, A55
Supper, R., Hasinger, G., Lewin, W. H. G., et al. 2001, A&A, 373, 63
Swartz, D. A., Ghosh, K. K., McCollough, M. L., et al. 2003, ApJS, 144, 213
Swartz, D. A., Ghosh, K. K., Tennant, A. F., & Wu, K. 2004, ApJS, 154, 519
Tananbaum, H., Gursky, H., Kellogg, E., Giacconi, R., & Jones, C. 1972, ApJL, 177, L5
Tempel, E., Tamm, A., & Tenjes, P. 2010, A&A, 509, A91
Tenjes, P., Haud, U., & Einasto, J. 1998, A&A, 335, 449
Tennant, A. F., Wu, K., Ghosh, K. K., Kolodziejczak, J. J., & Swartz, D. A. 2001, ApJL, 549, L43
Tetarenko, B. E., Sivakoff, G. R., Heinke, C. O., & Gladstone, J. C. 2016, ApJS, 222, 15
Tozzi, P., Gilli, R., Mainieri, V., et al. 2006, A&A, 451, 457
Trinchieri, G., & Fabbiano, G. 1991, ApJ, 382, 82
Trudolyubov, S. P. 2008, MNRAS, 387, L36
Tully, R. B., Courtois, H. M., Dolphin, A. E., et al. 2013, AJ, 146, 86
Tully, R. B., Courtois, H. M., & Sorce, J. G. 2016, AJ, 152, 50
Tully, R. B., Rizzi, L., Shaya, E. J., et al. 2009, AJ, 138, 323
Vasilopoulos, G., Maitra, C., Haberl, F., Hatzidimitriou, D., & Petropoulou, M. 2018, MNRAS, 475, 220
Vasilopoulos, G., Zezas, A., Antoniou, V., & Haberl, F. 2017, MNRAS, 470, 4354
Vogler, A., & Pietsch, W. 1999, A&A, 342, 101
Voss, R., & Ajello, M. 2010, ApJ, 721, 1843
Vulic, N., Gallagher, S. C., & Barmby, P. 2016, MNRAS, 461, 3443
Walton, D. J., Fuerst, F., Harrison, F., et al. 2013, ApJ, 779, 148
Walton, D. J., Fürst, F., Harrison, F. A., et al. 2017, ApJ, 839, 105
Walton, D. J., Harrison, F. A., Grefenstette, B. W., et al. 2014, ApJ, 793, 21
Walton, D. J., Middleton, M. J., Rana, V., et al. 2015, ApJ, 806, 65
Wang, S., Qiu, Y., Liu, J., & Bregman, J. N. 2016, ApJ, 829, 20
White, N. E., Swank, J. H., & Holt, S. S. 1983, ApJ, 270, 711
Wik, D. R., Hornstrup, A., Molendi, S., et al. 2014a, ApJ, 792, 48
Wik, D. R., Lehmer, B. D., Hornschemeier, A. E., et al. 2014b, ApJ, 797, 79
Wiktorowicz, G., Belczynski, K., & Maccarone, T. 2014, in Binary Systems, their Evolution and Environments, 37
Wiktorowicz, G., Sobolewska, M., Sadowski, A., & Belczynski, K. 2015, ApJ, 810, 20
Williams, B. F., Binder, B. A., Dalcanton, J. J., Eracleous, M., & Dolphin, A. 2013, ApJ, 772, 12
Williams, B. F., Dolphin, A. E., Dalcanton, J. J., et al. 2017, ApJ, 846, 145
Williams, B. F., Garcia, M. R., Kong, A. K. H., et al. 2004, ApJ, 609, 735
Yang, J., Laycock, S. G. T., Drake, J. J., et al. 2017, AN, 338, 220
Yang, Y., Wilson, A. S., Matt, G., Terashima, Y., & Greenhill, L. J. 2009, ApJ, 691, 131
Yukita, M., Hornschemeier, A. E., Lehmer, B. D., et al. 2016, ApJ, 824, 107
Yukita, M., Ptak, A., Hornschemeier, A. E., et al. 2017, ApJ, 838, 47
Zezas, A., Fabbiano, G., Ward, M., et al. 2004, in COSPAR Meeting 35, 35th COSPAR Scientific Assembly, ed. J.-P. Paillé, 4107
Zhang, Z., Gilfanov, M., & Bogdán, Á. 2012, A&A, 546, A36